

Raman studies on individual nanotubes and nanotube ensembles – vibrational properties and scattering efficiencies

Vorgelegt von Diplom-Physiker

Hagen Telg

aus Berlin

Von der Fakultät II: Mathematik und Naturwissenschaften
der Technischen Universität Berlin
zur Erlangung des akademischen Grades

Doktor der Naturwissenschaften

– Dr. rer. nat. –

genehmigte Dissertation

Promotionsausschuss

Vorsitzende : Prof. Dr. Sabine Klapp

1. Gutachter : Prof. Dr. Christian Thomsen, TU-Berlin

2. Gutachter : Prof. Dr. John Robertson, University of Cambridge, UK

Tag der wissenschaftlichen Aussprache: 06. November 2009

Berlin, 2009

D 83

Zusammenfassung *Raman studies on individual nanotubes and nanotube ensembles – vibrational properties and scattering efficiencies*

Die vorgelegte Dissertationsschrift befasst sich mit den optischen Eigenschaften von Kohlenstoffnanoröhren. Kohlenstoffnanoröhren (KNR) sind Nanometer dicke hohle Zylinder, deren Wände aus Kohlenstoffatomen aufgebaut sind. Das große Interesse an KNRs beruht unter anderem auf den vielversprechenden elektronischen Eigenschaften wie etwa dem ballistischen Transport und einer großen Anzahl möglicher Bandlücken. Die Charakterisierung von KNRs geschieht meist mithilfe der Raman-Spektroskopie. So lässt sich anhand der radialen Atmungsmoden (RAM) die atomare Struktur – gegeben durch die chiralen Indices (n_1, n_2) – der in einer Probe vorhandenen Röhren bestimmen. Anhand der hochenergetischen Moden lässt sich überprüfen, ob eine Probe metallische Röhren enthält.

Die Arbeit besteht aus zwei Teilen. Im ersten Teil wird die maximale Raman-Intensität der RAM für unterschiedliche (n_1, n_2) untersucht. Diese Intensitäten lassen Rückschlüsse auf die Elektron-Phonon-Kopplung zu, welche wiederum relevant für das Verständnis von Transporteigenschaften ist. Außerdem verspricht man sich, die Häufigkeiten der einzelnen (n_1, n_2) in einer Probe mithilfe der RAM-Intensitäten bestimmen zu können. Wir beobachten große Unterschiede zwischen den Raman-Intensitäten der verschiedenen (n_1, n_2) , welche wir entweder auf Unterschiede der natürlichen Linienbreiten oder auf Variationen der Elektron-Phonon-Kopplung zurückführen können.

Der zweite Teil der Arbeit behandelt die Form und den Ursprung der Moden im hochenergetischen Bereich des Raman-Spektrums von KNRs. Wie oben erwähnt, kann dieser Bereich des Spektrums zum Nachweis von metallischen Röhren in einer Probe benutzt werden. Entspricht die Anregungsenergie der Resonanzenergie einer metallischen Röhre, so verschiebt und verbreitert sich der sogenannte G^- Peak. Hierzu gibt es zwei Theorien, welche das Phänomen auf sehr unterschiedliche physikalische Prozesse zurückführen. Gewöhnliche Nanoröhrenproben enthalten viele verschiedenen Röhrensorten, metallische sowie halbleitende, sodass sich die Raman-Signale überlagern und daher keine der genannten Theorien zu favorisieren ist. In den letzten Jahren sind zunehmend Experimente an scheinbar einzelnen Röhren durchgeführt worden, deren Interpretationen sich je nach zurate gezogener Theorie widersprachen.

In dieser Arbeit werden Raman-Experimente an einem winzigen Bündel von einer metallischen und einer halbleitenden Nanoröhre präsentiert. Wir zeigen, dass der verbreiterte und verschobene Peak in metallischen Röhren dem durch eine sehr starke Elektron-Phonon-Kopplung verschobenen und verbreiterten LO Phonon zuzuordnen ist. Die Beobachtung eines weiteren Peaks bei der unveränderten Frequenz des LO Phonons ist folglich nur durch die Anwesenheit einer halbleitenden Röhre zu erklären. Außerdem bestätigen unsere Messungen, dass der verschobene und verbreiterte Peak ein intrinsisches Merkmal von metallischen KNRs ist, er resultiert also nicht aus der Bündelung von Röhren.

Des Weiteren können wir durch Raman-Experimente an Proben, die alle denkbaren (n_1, n_2) enthalten, die Durchmesserabhängigkeit der TO Phononen in halbleitenden Röhren zu kleineren Röhrendurchmessern erweitern.

List of Publications

Acetylene: A Key Growth Precursor for Single-Walled Carbon Nanotube Forests.

G. Zhong, S. Hofmann, F. Yan, H. Telg, J. H. Warner, D. Eder, C. Thomsen, W. I. Milne and J. Robertson. *J. Phys. Chem. C* **113(40)**, 17321 (2009).

Longitudinal Optical Phonons in Metallic and Semiconducting Carbon Nanotubes.

Martin Fouquet, Hagen Telg, Janina Maultzsch, Yang Wu, Bhupesh Chandra, J. Hone, Tony F. Heinz, and C. Thomsen. *Phys. Rev. Lett.* **102(7)**, 075501 (2009).

Growth and characterization of high-density mats of single-walled carbon nanotubes for interconnects.

J. Robertson, G. Zhong, H. Telg, C. Thomsen, J. H. Warner, G. A. D. Briggs, U. Dettlaff-Weglikowska, and S. Roth. *Appl. Phys. Lett.* **93(16)**, 163111 (2008).

G(-) and G(+) in the Raman spectrum of isolated nanotube: a study on resonance conditions and lineshape.

H. Telg, M. Fouquet, J. Maultzsch, Y. Wu, B. Chandra, J. Hone, T. F. Heinz, and C. Thomsen. *phys. stat. sol. (b)* **245(10)**, 2189 (2008).

Carbon nanotubes for interconnects in VLSI integrated circuits.

J. Robertson, G. Zhong, H. Telg, C. Thomsen, J. M. Warner, G. A. D. Briggs, U. Dettlaff, S. Roth, and J. Dijon. *phys. stat. sol. (b)* **245(10)**, 2303 (2008).

First and second optical transitions in single-walled carbon nanotubes: a resonant Raman study.

H. Telg, J. Maultzsch, S. Reich, and C. Thomsen. *phys. stat. sol. (b)* **244(11)**, 4006 (2007).

Resonant-Raman intensities and transition energies of the E_{11} transition in carbon nanotubes.

H. Telg, J. Maultzsch, S. Reich, and C. Thomsen. *Phys. Rev. B* **74(11)**, 115415 (2006).

Raman intensities of the first optical transitions in carbon nanotubes.

H. Telg, J. Maultzsch, S. Reich, F. Hennrich, and C. Thomsen. *phys. stat. sol. (b)* **243(13)**, 3181 (2006).

Radial breathing mode of single-walled carbon nanotubes: Optical transition energies and chiral-index assignment.

J. Maultzsch, H. Telg, S. Reich, and C. Thomsen. *Phys. Rev. B* **72**, 205438 (2005).

Strength of radial breathing mode in single-walled carbon nanotubes.

M. Machón, S. Reich, H. Telg, J. Maultzsch, P. Ordejón, and C. Thomsen. *Phys. Rev. B* **71**, 035416 (2005).

Chirality dependence of the high-energy Raman modes in carbon nanotubes.

H. Telg, J. Maultzsch, S. Reich, and C. Thomsen. In *Electronic Properties of Novel Nanostructures*, volume 786 of *AIP conference proceedings*, page 162. 19th International Winterschool and Euroconference on Electronic Properties of Novel Materials, Kirchberg, Austria, Mar. 2005.

Chiral-index assignment of carbon nanotubes by resonant Raman scattering.

J Maultzsch, H Telg, S Reich, and C Thomsen. In *Electronic Properties of Novel Nanostructures*, volume 786 of *AIP conference proceedings*, pages 401–405. 19th International Winterschool and Euroconference on Electronic Properties of Novel Materials, Kirchberg, Austria, Mar. 2005.

Chirality distribution and transition energies of carbon nanotubes.

H. Telg, J. Maultzsch, S. Reich, F. Hennrich, and C. Thomsen. *Phys. Rev. Lett.* **93**, 177401 (2004).

Raman excitation profiles for the (n_1, n_2) assignment in carbon nanotubes.

H. Telg, J. Maultzsch, S. Reich, F. Hennrich, and C. Thomsen. In *Structural and Electronic Properties of Molecular Nanostructures*, AIP Conference Proceedings, pages 330–333. 18th International Winterschool and Euroconference on Electronic Properties of Novel Materials, Kirchberg, Austria, Mar. 2004.

Contents

1	Introduction	1
2	Experimental method	5
2.1	Raman scattering	5
2.1.1	Scattering efficiency	6
2.1.2	From the measured Raman intensity to the Raman susceptibility	8
2.1.3	Resonant Raman scattering	10
2.2	Experimental setup	12
3	Basic properties of single-walled carbon nanotubes	15
3.1	Atomic structure	17
3.2	Electronic bandstructure - optical transitions	19
3.2.1	The zonefolding approximation	19
3.2.2	Optical transitions	21
3.2.3	Overview of theoretical models	23
3.3	Vibrational properties and Raman effect	24
3.3.1	The phonon bandstructure	24
3.4	Resonance enhancement	27
3.5	Chiral-index assignment	28
3.6	The influence of the environment on the Kataura plot	32
4	RBM intensities: abundance <i>versus</i> e-ph coupling	37
4.1	Raman susceptibility	38

4.1.1	Dependence of $ \chi_R^{max} $ on the Optical Transition E_{ii}	41
4.1.2	Dependence of $ \chi_R^{max} $ on the Family ν	43
4.1.3	Dependence of $ \chi_R^{max} $ on the Chiral Angle	44
4.1.4	Metallic <i>versus</i> Semiconducting Nanotubes	46
4.1.5	Diameter Dependence of $ \chi_R^{max} $	48
4.2	(n_1, n_2) abundances	49
4.3	Summary	50
5	The high-energy modes	53
5.1	Nanotubes in solution	56
5.1.1	The LO phonon modes	57
5.1.2	The TO phonon modes	63
5.1.3	Infrared active phonon	66
5.2	Isolated nanotubes	69
5.2.1	Rayleigh experiments	70
5.2.2	Raman experiments	71
5.3	Summary	76
6	Conclusions	79
	Bibliography	81
	Acknowledgements	91

Chapter 1

Introduction

In recent years the progress in the field of device-miniaturization and crystal growth increased the interest in low dimensional materials. The confinement of the crystallinity to two, one or even zero dimensions offers applications beyond miniaturization. The low dimensional materials reveal new and promising optical, electronic and transport properties.

Since their discovery in 1991 by Iijima *et al.* [1] the interest in carbon nanotubes has constantly grown. The reason for the large number of scientific groups and recently also companies practicing research on carbon nanotubes can be found in the large number of imaginable application in the microscopic as well as in the macroscopic scale. While some people dream about a space elevator tenth of thousand kilometers in length others design electronic nanometer-sized devices [2]. The idea of a space elevator is based on the enormous strength of the sp^2 bonds which connect the carbon atoms in a nanotube and which is even stronger than the sp^3 bonds in diamond. In addition to the strength nanotubes have a very low density. The promising properties of nanotubes for electronic devices is the ballistic transport which is maintained over large distances and their electronic bandgap which strongly varies for different atomic structure (n_1, n_2) . Figure 1.1 shows two carbon nanotubes with very similar atomic structure (n_1, n_2) . However, this apparently minor difference results in large differences in the electronic properties, with the left tube being metallic and the right tube having a bandgap of $E_g = 1.36$ eV.

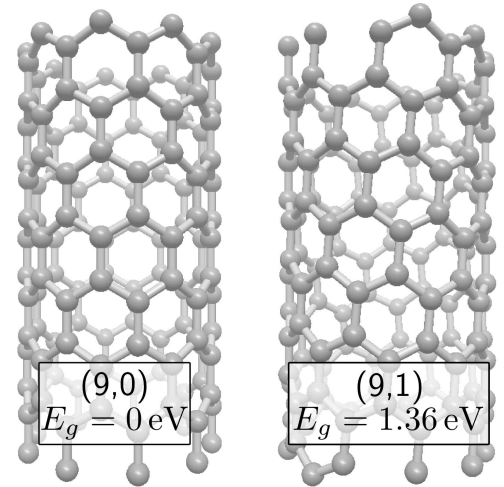


Figure 1.1: Metallic (left) and semiconducting (right) carbon nanotube. Minor differences in the atomic structure result in significant differences in the electronic properties.

The probably most established characterization method for carbon nanotubes is the Raman spectroscopy. [3, 4] While the defect induced D-mode offers a tool to estimate the quality of a nanotube sample, the diameter distribution can be obtained from the diameter dependent radial breathing mode (RBM). Due to the unique electronic bandstructure of carbon nanotubes the exact atomic structure (n_1, n_2) can be obtained from the RBM in conjunction with the excitation energy. [5] Even without a detailed (n_1, n_2) assignment, the presence of metallic nanotubes in a sample can be detected on the basis of the shape of the high-energy modes (HEM) in the Raman spectrum [6–8].

The electronic properties, therefore the width of the bandgap, of carbon nanotubes vary for different environments due to screening of the electron-hole and electron-electron interactions in the tube. This property, which makes nanotubes suitable for gas sensor applications [9], is still under debate and controversial results can be found in the literature [10–13]. In Sect. 3.6 we present resonant Raman scattering experiments on nanotubes dissolved in aqueous solution. By using two different types of solvents we show how transition energies and RBM frequencies are effected by different environments.

One of the major challenges in nanotube chemistry was and will be in the future the growth or subsequent sorting of particular (n_1, n_2) [6, 14, 15]. This, in turn, demands a technique to probe (n_1, n_2) abundances in a sample, which does not exist yet. One idea to probe (n_1, n_2) abundances is to use the Raman intensities of the RBM [16–18]. However, the RBM scattering efficiency strongly depends on the particular (n_1, n_2) [5, 19–22]. In Chap. 4 we present a detailed study of the RBM Raman intensities of nanotubes dispersed in solution. We discuss variations of the intensities between different (n_1, n_2) with respect to the scattering efficiency, the influence of the lifetime of the optical transitions, the electron-phonon coupling and (n_1, n_2) abundances.

As mentioned above the high-energy mode (HEM) in the carbon nanotube Raman spectrum is widely used in the nanotube community to probe the presence of metallic nanotubes in a sample. A broadened and downshifted HEM indicates the presence of metallic nanotubes in resonance. The origin of this effect was described by two conflicting theories [23–25]. On the one hand experiments on nanotube ensembles are not capable of solving this conflict. On the other hand this conflict does not interfere with the interpretation of the experimental results regarding the presence of metallic nanotubes in the sample. Recently there is an increasing number of experiments performed on presumably individual nanotubes [26–30]. For individual nanotubes the conflicting theories lead to contradicting interpretations. An answer to this problem is essential in order to show from a Raman spectrum if the sample consists of an individual metallic nanotube or a bundle of nanotubes including semiconducting tubes. To address this issue we present in Chap. 5 resonant Raman experiments performed on nanotube dispersed in solution and

on a tiny bundle of one metallic and one semiconducting nanotube. Consulting the RBM frequencies we assign the different features of the HEM to particular (n_1, n_2) . Based on the assignment we discuss the physical origin of the different HEM features.

Chapter 2

Experimental method

2.1 Raman scattering

When light travels through a medium with no optical transition which could lead to absorption, the light will still lose intensity due to scattering. Most of the scattered light is due to Rayleigh scattering, a process where the light is elastically scattered – the energy of the light is preserved – by small imperfections of the medium. However, a tiny fraction of the light is inelastically scattered and therefore loses or gains energy during the scattering process.

In this work we will mainly focus on Raman scattering, an inelastic scattering process which describes the scattering of light by phonons. As light can be regarded as a stream of photons or as an electromagnetic wave there are two ways to describe the process of scattering. For a better understanding of the process we will describe Raman scattering from both perspectives. As discussed later this approach is especially useful for the comparison between theoretical predictions and experimental observations.

When an electro-magnetic wave with frequency ω_i and wave vector \vec{k}_i travels through a medium a polarization $\vec{P}_i(\vec{r}, t)$ of the electron cloud will be induced, with an amplitude depending on the polarizability χ (susceptibility). At non-zero temperatures the atoms in the medium will vibrate and are therefore periodically displaced with frequency ω_0 and wave vector \vec{q} . When such a displacement $\vec{Q}(\vec{r}, t)$ changes the polarizability of the medium ($d\chi/d\vec{Q}|_0 \neq 0$), the propagating sinusoidal polarization $\vec{P}_i(\vec{r}, t)$ induced by the light will be modulated by the vibration of the atoms. The modulated wave $\vec{P}(\vec{r}, t)$ can be described as a superposition of three waves, $\vec{P}_i(\vec{r}, t)$ the polarization wave moving in phase with the incident light and two waves $\vec{P}_{ind}^{\pm}(\vec{r}, t)$ with frequencies and wave vectors as \vec{P}_i increased or decreased by the frequency and wave vector of the atomic vibration,

$$\begin{aligned}
\vec{P}(\vec{r}, t) &= \vec{P}_i(\vec{r}, t) + \vec{P}_{ind}^+(\vec{r}, t) + \vec{P}_{ind}^-(\vec{r}, t) \\
&= \vec{P}_i(\vec{k}_i, \omega_i) \cos(\vec{k}_i \cdot \vec{r} - \omega_i t) \\
&\quad + \vec{P}_{ind}(\vec{k}_i, \omega_i, \vec{Q}) \cos[(\vec{k}_i + \vec{q}) \cdot \vec{r} - (\omega_i + \omega_0)t] \\
&\quad + \vec{P}_{ind}(\vec{k}_i, \omega_i, \vec{Q}) \cos[(\vec{k}_i - \vec{q}) \cdot \vec{r} - (\omega_i - \omega_0)t] \quad . \tag{2.1}
\end{aligned}$$

While the first term in Eq. 2.1 represents the unscattered light traveling through the medium, the second and third terms lead to radiation with higher (anti-Stokes) and lower frequency (Stokes), respectively. The shift of the Stokes and anti-Stokes radiation with respect to the unscattered light is given by the eigenfrequency of the studied atomic vibration.

It is well known that the atomic vibrations are quantized into phonons and the electromagnetic field into photons. Therefore, speaking from the microscopic point of view, the process described above refers to a photon being scattered by a phonon intermediated by an electron. During the process the phonon is either generated (Stokes) or annihilated (anti-Stokes).

In the Raman scattering process energy and momentum has to be conserved. Therefore the momentum q of the phonon can not exceed $2\vec{k}_i$ (backscattering). As a consequence only zone-center phonons can be observed in a Raman experiment with the incident light in the visible, since the momentum of the light is 2-3 orders of magnitude smaller than the Brillouin zone of the crystal.

2.1.1 Scattering efficiency

To calculate the scattering efficiency $dS/d\Omega$ for Raman scattering we need to calculate the power of the electro-magnetic field induced by the polarizations $\vec{P}_{ind}^\pm(\vec{r}, t)$ as a function of the power of the incident light. In a semiclassical approach this leads to the *power* Raman scattering efficiency given in Ref. [31]. As we will use a detector which is based on photon counting we rather need a *quantum* scattering efficiency. This is obtained by multiplying the *power* efficiency by ω_i/ω_s , where ω_i and ω_s refer to the incident and the scattered

light, respectively [32]. Therewith the *quantum* Raman scattering efficiency reads,

$$\frac{dS}{d\Omega} = \frac{1}{V} \frac{d\sigma_s}{d\Omega} = \frac{\omega_s^3 \omega_i}{(4\pi)^2 c^4} \frac{\eta_s}{\eta_i} \frac{\eta_{out}^2}{\eta_{in}^2} R |\mathbf{e}_s \cdot \chi_R \cdot \mathbf{e}_i|^2 \Lambda \quad (2.2)$$

where $R = (1 - R_i)(1 - R_s)$

$$\Lambda = \frac{\hbar}{2\omega_{ph}} (n(\omega_{ph}) + 1) \quad (\text{Stokes})$$

$$\Lambda = \frac{\hbar}{2\omega_{ph}} n(\omega_{ph}) \quad (\text{anti - Stokes})$$

$$n(\omega_{ph}) = \frac{1}{e^{\frac{\hbar\omega_{ph}}{kT}} - 1} \quad (\text{Bose - Einstein factor})$$

where c is the speed of light and ω_{ph} the eigen-frequency of the phonon. \mathbf{e}_i and \mathbf{e}_s are the polarization vectors of the incident and the scattered light, respectively. The expression including the refractive indices in the sample η_i for the incident light and η_s for the scattered light and the refractive indices η_{in} inside and η_{out} outside the sample account for influence of these values on the effective angle of collection. R refers to the loss of light due to the reflection when the light enters (R_i) and leaves (R_s) the sample. The Raman susceptibility χ_R is a second rank tensor which is given by the sensitivity of the optical susceptibility χ_o to the displacement of the atoms related to the particular phonon. Λ represents the thermodynamical average over the ground states of the material. It therefore considers the probability of a photon being created or annihilated in the presence of thermal phonons.

Unlike the Raman cross section $d\sigma_s/d\Omega$ the scattering efficiency $dS/d\Omega$ is independent from the scattering volume V . When deriving the cross section the incident beam is assumed to cover all of V . Since the Raman intensity depends on the flux rather than the flux density of the incident light – simple Raman scattering is a linear optical process – dropping V is reasonable and avoids misunderstandings. Therefore Eq. 2.2 represents the ratio between incident and scattered photons per unit length within the sample.

The scattering efficiency given in Eq. 2.2 does not consider absorption of light in the sample, since the absorption depends on the length of the scattering path. Absorption is considered in the next section (Eq. 2.3) when discuss the Raman intensity actually observed in the experiments.

2.1.2 From the measured Raman intensity to the Raman susceptibility

In the experimental section of this work we present Raman spectra of carbon nanotubes. On the one hand we are interested in the positions of the various features. On the other hand we want to discuss the intensity variations between different peaks with respect to the properties of particular nanotubes. Therefore we have to strip down the measured Raman intensities to the Raman susceptibility χ_R , since it is independent from the experimental conditions and thus exclusively represents the properties of the nanotube. The Raman intensities collected by a Raman setup (Sect. 2.2) are basically the scattering efficiency given by Eq. 2.2 for a particular solid angle and multiplied by the integration time t , the laser power P_i , and the scattering length L . Additionally the intensities are scaled by the response $I_R(\omega_s)$ of the experimental setup and, since we are measuring on an ensemble of nanotubes in solution, the nanotube density ρ . Therefore, the measured Raman intensity $I(\omega_s)$ is given by

$$I(\omega_s) = \frac{dS}{d\Omega} \Delta\Omega P_i t \frac{L_\alpha}{\hbar \omega_i} I_R(\omega_s) \quad (2.3)$$

$$L_\alpha = \frac{1 - e^{-(dS/d\Omega + \alpha_i + \alpha_s)L}}{dS/d\Omega + \alpha_i + \alpha_s}$$

As mentioned above, the scattering efficiency in Eq. 2.2 gives the probability for an incident photon being inelastically scattered by the sample involving a particular phonon. Therefore the laser power has to be transferred to the number of photons per unit time. This is reflected in Eq. 2.3 by dividing by $\hbar \omega_i$. L_α is the scattering path length considering absorption of the light, with the absorption coefficients α_i and α_s for the incident and scattered light, respectively. L is the path length usually given by the sample thickness or by the depth of field defined by the setup. For our experiments we assume the latter since most of our samples are much thicker than the depth of field. Note that the depth of field depends on the wavelength, therefore we will use $L_\alpha(\omega_s)$ in the following.

In order to obtain the Raman susceptibility from measurements, we need to normalize the observed Raman intensity to $1/32$, ρ , π^{-2} , c^{-4} , \hbar , η_s/η_i , $\Delta\Omega$, ω_s^3 , $I_R(\omega_s)$, $L_\alpha(\omega_s)$, η_{out}^2/η_{in}^2 , R , ω_{ph}^{-1} , $(n+1)$, t and P_i . Since we do not know the density ρ of nanotubes in our sample, we can not determine absolute Raman susceptibilities. However, since ρ is constant we can still compare the relative Raman susceptibilities for the different types of tubes (this is discussed in more detail in Sect. 4). Not being interested in absolute values we can ignore all constants, which are marked in blue in the list above. η_s/η_i can be treated as one because the observed nanotubes are in low concentration surrounded by media (water, air) with small dispersions in the region of interest.

The list of variables, to which we have to normalize $I(\omega_s)$, can further be shortened when the observed Raman intensity $I(\omega_s)$ is normalized to the intensity of calcium fluoride $I_{\text{CaF}_2}(\omega_s)$ ($\omega_{ph} = 320 \text{ cm}^{-1}$), taken at identical experimental conditions. Since for all measurements we are far off resonance (bandgap: $E_g(\text{CaF}_2) \approx 8 \text{ eV}$), the Raman susceptibility of CaF_2 can be treated as constant [33]. When we normalize the Raman intensity $I(\omega_s)$ to $I_{\text{CaF}_2}(\omega_s)$ the result obviously becomes independent from ω_s and the system response $I_R(\omega_s)$. Both the nanotube samples as well as the CaF_2 are totally transparent. Assuming very small values for α_i and α_s , $L_\alpha(\omega_s)$ approximates $L(\omega_s)$ which is solely determined by the experimental conditions and therefore also drops out by normalizing $I(\omega_s)$ to $I_{\text{CaF}_2}(\omega_s)$.

This procedure also makes the the result independent from η_{out}^2/η_{in}^2 and R , which both depend on ω_s and have different values for the nanotube sample and CaF_2 . Most measurements presented in this work are conducted on nanotubes in solution contained in a glass cell. Due to the very similar properties of water, glass and CaF_2 concerning the dependence on the frequency of light, η_{out}^2/η_{in}^2 and R lead to a constant value when $I(\omega_s)$ is normalized to $I_{\text{CaF}_2}(\omega_s)$. Deviations in the optical properties between water, glass and CaF_2 lead to a deviation in the resulting Raman susceptibility χ_R of about 1 %. Only in case of nanotubes in air this error becomes larger.

Note that usually the phonon frequency ω_{ph} of the studied Raman mode differs from that of CaF_2 , $\omega_{ph, \text{CaF}_2}$. Therefore the excitation frequencies ω_i also vary between $I(\omega_s)$ and $I_{\text{CaF}_2}(\omega_s)$. For very large differences between studied Raman modes ($\Delta\omega_{ph} > 1000 \text{ cm}^{-1}$) this has to be taken into account.

After dividing $I(\omega_s)$ by $I_{\text{CaF}_2}(\omega_s)$ we only have to normalize $I(\omega_s)$ to the ω_{ph}^{-1} , $(n+1)$, t and P_i to finally determine the square of the Raman susceptibility χ_R .

In summary, after normalizing the Raman spectra to t , P_i , $(n+1)$, ω_{ph}^{-1} and $I_{\text{CaF}_2}(\omega_s)$ the observed Raman intensities are proportional to $|\mathbf{e}_s \cdot \chi_R \cdot \mathbf{e}_i|^2$, the square of the Raman susceptibility.

2.1.3 Resonant Raman scattering

Figure 2.1 depicts how an electron is excited, scattered and relaxed during the Raman process. Three cases are distinguished: the non-resonant case, where the energy of the excitation energy ($\hbar\omega_i$) is far away from a optical transition; the incoming resonance, where the excitation energy $\hbar\omega_i$ matches the transition energy of an intermediate state; and the outgoing resonance, where the excited electron is scattered by the phonon into the real intermediate state from which it radiatively relaxes emitting a photon $\hbar\omega_s$. When a resonance condition is met, the Raman signal is strongly enhanced. In fact, in individual nanotubes, Raman scattering can only be observed with considerable signal strength when excited resonantly. Therefore we will ignore the non-resonant contributions to the scattering efficiency in the following.

For resonant Raman scattering in carbon nanotubes we assume an individual intermediate excitonic state and the initial and final electronic states to be the same. Therefore the Raman susceptibility close to the resonance can be described by [34–37]

$$|\chi_R|^2 = \frac{2\omega_{ph}V}{\omega_i^2} K \quad (2.4)$$

$$\text{where} \quad K = \frac{\mathcal{M}_R^2}{\left((\hbar\omega_i - E_{ii})^2 + \left(\frac{\gamma}{2}\right)^2\right) \left((\hbar\omega_i - \hbar\omega_{ph} - E_{ii})^2 + \left(\frac{\gamma}{2}\right)^2\right)} \quad (2.5)$$

where E_{ii} is the energy of the optical transition and \mathcal{M}_R the Raman matrix element. γ refers to the lifetime and therefore the natural linewidth of the optical transition. In most samples the optical transitions are additionally broadened by imperfections. Therefore we will refer to γ as the broadening parameter.

K describes the convolution of two Lorentzian curves of width γ and distance ω_{ph} . Due to ω_i in Eq. 2.4 the maximum of the two Lorentzians is slightly different. For phonons with small ω_{ph} , as for the radial breathing mode in nanotubes, this difference is rather

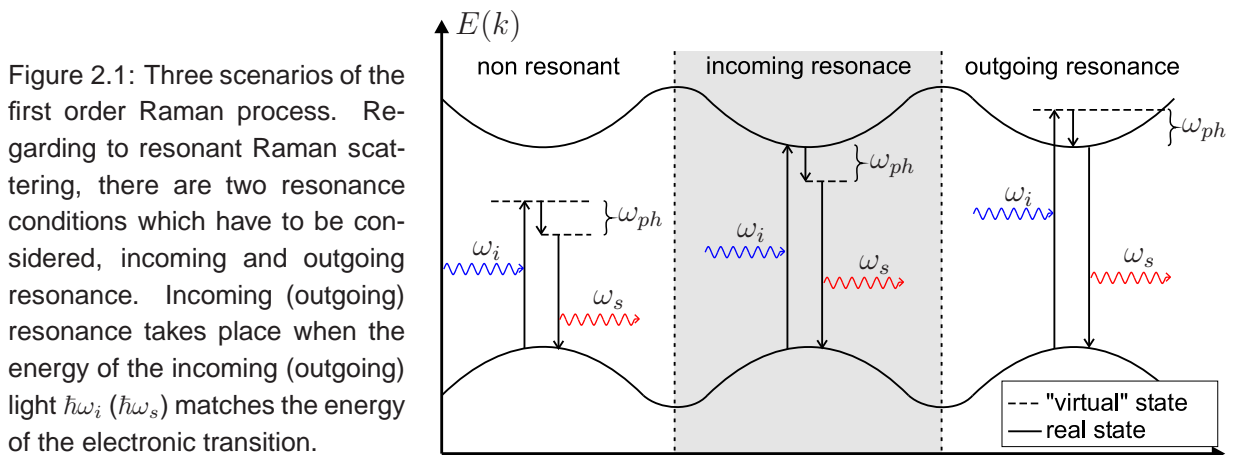


Figure 2.1: Three scenarios of the first order Raman process. Regarding to resonant Raman scattering, there are two resonance conditions which have to be considered, incoming and outgoing resonance. Incoming (outgoing) resonance takes place when the energy of the incoming (outgoing) light $\hbar\omega_i$ ($\hbar\omega_s$) matches the energy of the electronic transition.

small. We will mainly use the expression of the resonance profile in order to obtain the E_{ii} and γ from collected Raman intensity profiles. As we assume changes on E_{ii} and γ due to ω_i to be negligible we will fit the Raman intensity profiles by Eq. 2.5. However, when the aim is to compare experimental results to theoretical predictions on \mathcal{M}_R for different modes with different resonance conditions the influence from ω_i on \mathcal{M}_R might be relevant.

The Raman matrix elements consists of two times the absorption strength \mathcal{M}_{abs} and the electron-phonon coupling $\mathcal{M}_{\text{e-ph}}$ and is therefore given by $\mathcal{M}_R = \mathcal{M}_{\text{abs}}^2 \mathcal{M}_{\text{e-ph}}$ [36]. Some theoretical models only provide $\mathcal{M}_{\text{e-ph}}$. Therefore we will sometimes compare our results solely to the electron-phonon coupling assuming the effects due to \mathcal{M}_{abs} to be small.

2.2 Experimental setup

In a Raman experiment it is essential to suppress the elastically scattered light of the exciting laser. This is either achieved with a notch filter, a very narrow band-stop filter, or, as in our experiments, with a triple monochromator. In the triple monochromator setup the first two monochromators (pre-monochromators) are coupled in a subtractive configuration. The slit between the pre-monochromators is rather large and defines the part of the spectrum which can pass the monochromators. In this way the pre-monochromators solely act as a bandpass filter, very efficiently suppressing the rest of the spectrum. The final diffraction is done by the third monochromator (spectrograph).

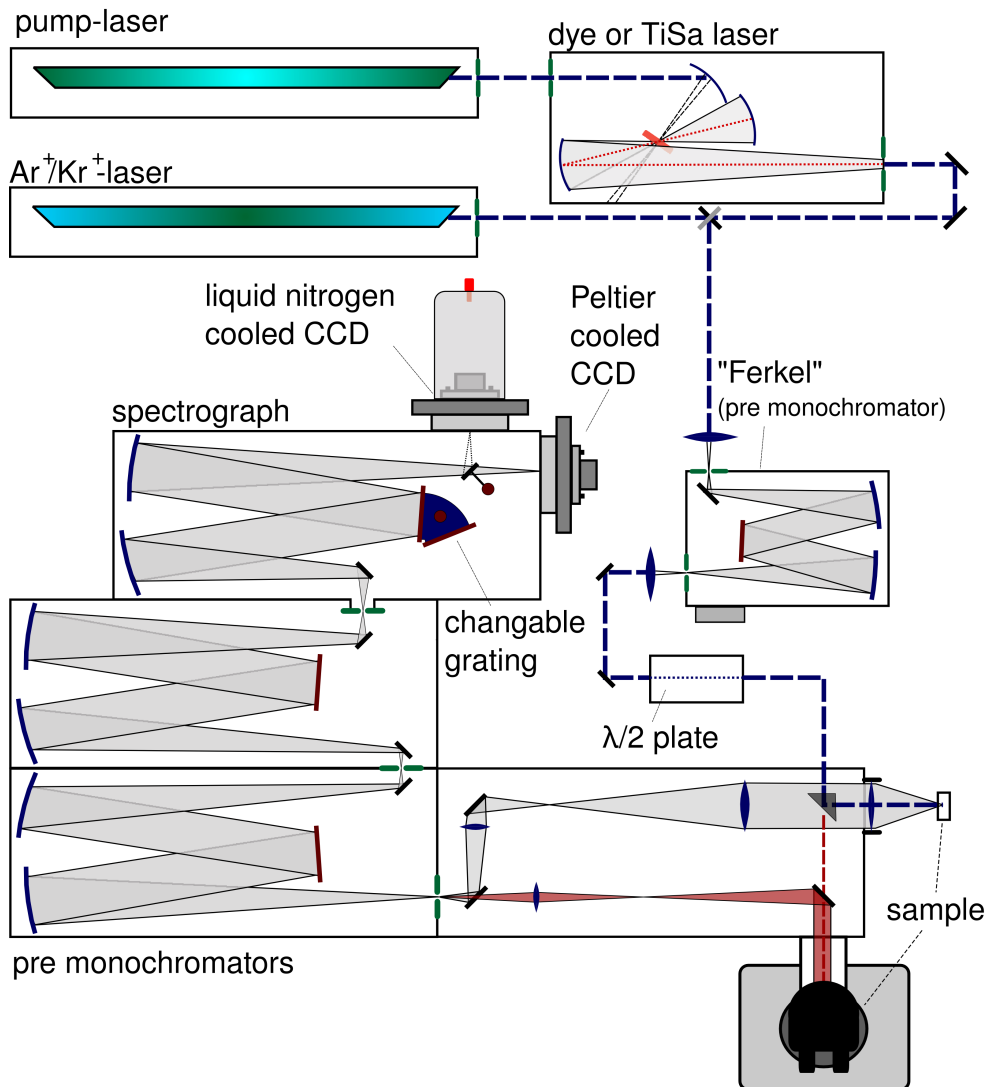


Figure 2.2: Experimental setup for Raman experiments.

While the notch-filter gives a better signal to noise ratio and enables a more compact setup, the triple-monochromator setup can be used for tunable laser systems. Since our aim was to collect intensity profiles of the Raman modes, we used a tunable Raman setup including a triple-monochromator.

The excitation energy was varied between ≈ 1.13 eV and ≈ 2.17 eV using tunable lasers, a titanium-sapphire laser (≈ 1.13 - 1.80 eV) and a dye laser running with DCM-special (≈ 1.80 - 2.05 eV) and Rhodamin 6G (≈ 2.00 - 2.17 eV), respectively. For the signal detection the spectrograph was equipped with two silicon charge-coupled devices (CCD) and an indium gallium arsenide photodiode array, each of the three having its particular operating range [Si(LN-cooled): visible; Si(Peltier-cooled): visible – near-infrared; InGaAs(LN-cooled): near-infrared].

In our setup the Raman spectroscopy is performed in backscattering geometry. It is possible to choose between a macro and a micro configuration. Compared to the micro configuration, the focus-spot and the scattering length is larger in the macro setup, due to the smaller numerical aperture in macro. A larger focus-spot and scattering length is useful for transparent volume-samples (see Sect. 4 and 5.1), since it leads to smaller power densities and therefore less local heating of the sample. The small focus-spot of the micro setup is useful for the observation of small areas or single objects as in Sect. 5.2.

Chapter 3

Basic properties of single-walled carbon nanotubes

Nanotubes are hollow cylinders made of carbon atoms. They can be understood as graphene sheets – a single layer of graphite – rolled up to a seamless tube. Therefore many of the properties of nanotubes are inherited or can be derived from graphene, at least to a certain level of approximation.

The sp^2 hybrid bond, which connects the carbon atoms in graphene, is probably the strongest bond found in chemistry. In carbon nanotubes this bond is only slightly weakened by the deformation due to the curvature of the wall; this is most pronounced in very small diameter tubes. These strong bonds make nanotubes extremely stiff and more than 100 times stronger than steel [38,39]. Therefore nanotubes are interesting for applications like probes in atomic force microscopes and electromechanical memories [40,41].

Also inherited from graphene, nanotubes reveal a high carrier mobility and ballistic transport, which makes them future candidates for replacing silicon in electronic devices [42,43]. A further reason to apply nanotubes in electronic devices is the very high thermal conductivity which is due to the rigidity of the sp^2 bonds and the weak coupling between phonons [44].

However, most of these fascinating properties depend on the atomic structure of the studied nanotube. In the first section of this chapter (Sect. 3.1) we will show how a nanotube can be constructed by rolling up a sheet of graphene. We will show how the infinite number of different nanotubes structures are named by their chiral indices (n_1, n_2) and how to determine characteristic structural properties such as the diameter d and chiral angle θ .

In Sect. 3.2 we show how the electronic bandstructure of a nanotube can be derived from the bandstructure of graphene and from the atomic structure of the particular nanotube (n_1, n_2) . It turns out that nanotubes can be either metallic or semiconducting.

Symmetry considerations in addition to the bandstructure will lead to the optical properties of carbon nanotubes regarding the allowed optical transitions which will lead to resonance enhancement of the Raman signal. Furthermore we will introduce two more ways to classify carbon nanotubes, the family ν and the band index \mathfrak{b} .

In section 3.3 we will give an introduction to the phonon bandstructure of carbon nanotubes. Here we also introduce the Raman spectrum of nanotubes with focus on the diameter dependence of the radial breathing mode.

As mentioned above, most of the nanotube properties depend on the atomic structure of the particular nanotube (n_1, n_2) . Therefore it is crucial to know which nanotube(s) is (are) present in the studied sample. In Sect. 3.5 we introduce a technique to assign nanotubes to their particular structure (n_1, n_2) by resonant Raman scattering [5].

Table 3.1: Collection of nanotube properties and classifications which are frequently used in this work.

name	formula
chiral indices	$(n_1, n_2) = n_1 \vec{a}_1 + n_2 \vec{a}_2$
diameter	$d = \vec{a}_0 / \pi \sqrt{n_1^2 + n_1 n_2 + n_2^2}$
chiral angle	$\theta = \arccos \left((n_1 + n_2/2) / \sqrt{n_1^2 + n_1 n_2 + n_2^2} \right)$
family index ¹	$\nu = (n_1 - n_2) \bmod 3$
metallic	$\nu = 0$
semiconducting	$\nu = \pm 1$
branch index	$\mathfrak{b} = 2n_1 + n_2$
next neighbor within a branch	$(m_1, m_2) = (n_1 \pm 1, n_2 \mp 2)$
ω_{RBM} versus diameter	$\omega_{\text{RBM}} = \frac{c_1}{d} + c_2 \quad c_1 = 215 \frac{\text{nm}}{\text{cm}}, c_2 = 18 \text{ cm}^{-1}$

¹ Instead of the branch index we usually name a branch by (n_1, n_2) of the first nanotube within the branch, the tube with the smallest d .

3.1 Atomic structure

In figure 3.1 we depict how a nanotube can be constructed by rolling up a sheet of graphene. To actually result in a seamless tube, the vector $\vec{c}_h = n_1 \cdot \vec{a}_1 + n_2 \cdot \vec{a}_2$, which will represent the circumference of the particular nanotube, has to be a multiple (n_1, n_2) of the graphene basis vectors \vec{a}_1 and \vec{a}_2 . Additionally the side of the sheet which will be parallel to the axis of the tube has to be perpendicular to \vec{c}_h , that is to say the sheet has to be a rectangle. The resulting tube will describe a one dimensional crystal with the only basis vector T .

In this way an infinite number of different nanotubes can be constructed solely differing by the index (n_1, n_2) which therefore they are named by. In graphene there exist two distinguishable direction along which the graphene lattice shows the most obvious periodicity and which are named in Fig. 3.1 by zig-zag and armchair. These are also the names which nanotubes are called by when they are rolled up along vectors \vec{c}_h parallel to these directions. Both kind of nanotubes zig-zag and armchair, which are given by nanotubes with $n_2 = 0$ and $n_1 = n_2$, respectively, are also called achiral. All other tubes are called chiral. Achiral tubes distinguish themselves by their very small basis vectors T , for which their are preferred in theoretical studies.

In section 4 we show that the Raman intensity strongly depends on particular characteristic of nanotubes, which are the diameter d the chiral angle θ and the family ν [3]. The diameter of the nanotube can be calculated from the vector \vec{c}_h ,

$$d = \frac{|\vec{c}_h|}{\pi} = \frac{\vec{a}_0}{\pi} \sqrt{n_1^2 + n_1 n_2 + n_2^2}. \quad (3.1)$$

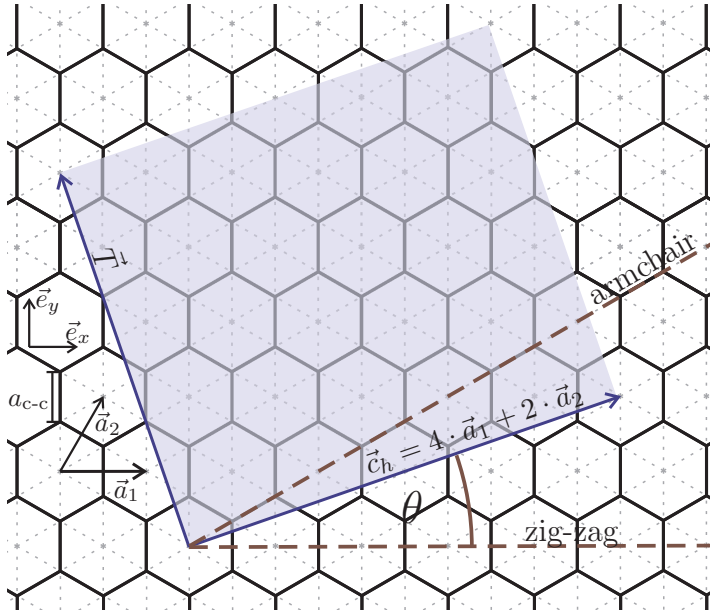


Figure 3.1: Lattice structure of graphene with basis vectors $\vec{a}_1 = (1, 0) \cdot a_0$ and $\vec{a}_2 = (0.5, 0.5\sqrt{3}) \cdot a_0$; $a_0 = \sqrt{3} \cdot a_{c-c}$ with the distance a_{c-c} between neighboring carbon atoms. Rolling up the highlighted area to a cylinder along the vector \vec{c}_h forms the unit cell of a (4,2) tube.

The chiral angle is defined by the angle between \vec{c}_h and the zig-zag direction and is thus given by

$$\theta = \arccos \left(\frac{n_1 + n_2/2}{\sqrt{n_1^2 + n_1 n_2 + n_2^2}} \right) . \quad (3.2)$$

For chiral angles larger than 60° the nanotubes structures (n_1, n_2) repeat. However, already for angles larger than 30° almost identical nanotubes can be found with $\theta < 30^\circ$. They only differ in the order of n_1 and n_2 , therefore in the chirality in terms of right or left handed. As we can not distinguish (n_1, n_2) from (n_2, n_1) in the experiment we will only distinguish tubes with chiral angles between 0° and 30° with $\theta = 0^\circ$ for zig-zag tubes and $\theta = 60^\circ$ for armchair tubes.

3.2 Electronic bandstructure - optical transitions

From the “Theoretical Solid state Physics’ classes we know that there are several ways to approximate the electronic bandstructures of a solid, such as free electron, tight-binding, *ab-initio* and density matrix formalism. For this work the relevant information we want to gain from the nanotube bandstructure is predetermined by the method by which we perform a (n_1, n_2) assignment of the different nanotubes. As this method is based on pattern recognition, it is more important for us to know the bandstructure of as many nanotubes as possible than to know the accurate energy values. A theory which provides the bandstructure of all nanotubes with a – for our purposes – sufficient precision is the zonefolding approximation on the basis of a tight binding description of the bandstructure of graphene (Sect. 3.2.1). The so obtained bandstructures lead, under consideration of selection rules, to the optical transition energies forming the characteristic E_{ii} versus d pattern, known as the Kataura plot (see Sect. 3.2.2) [45]. In Sect. 3.2.3 we will discuss deviations from the zonefolding approximation when taking the curvature of the tube-wall and many-particle interactions into account.

3.2.1 The zonefolding approximation

The bandstructure of carbon nanotubes obtained from the zonefolding approximation is given by the bandstructure of graphene under the consideration of a limitation of the

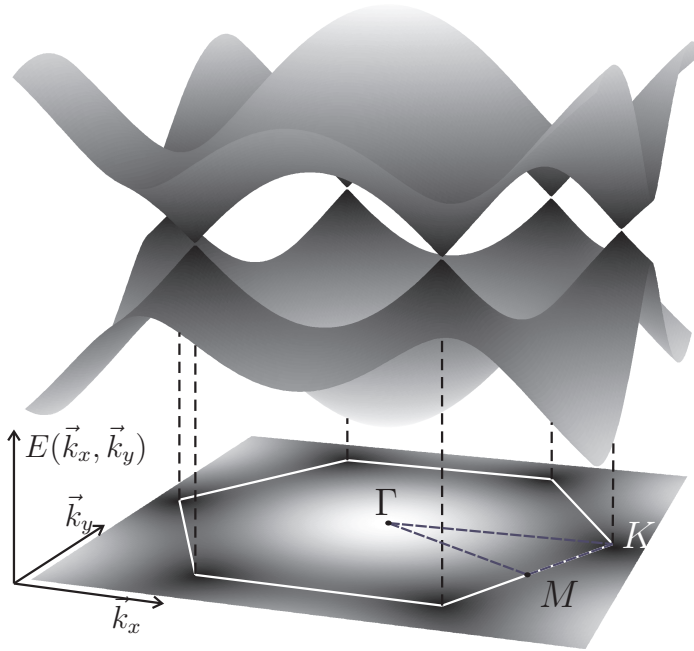
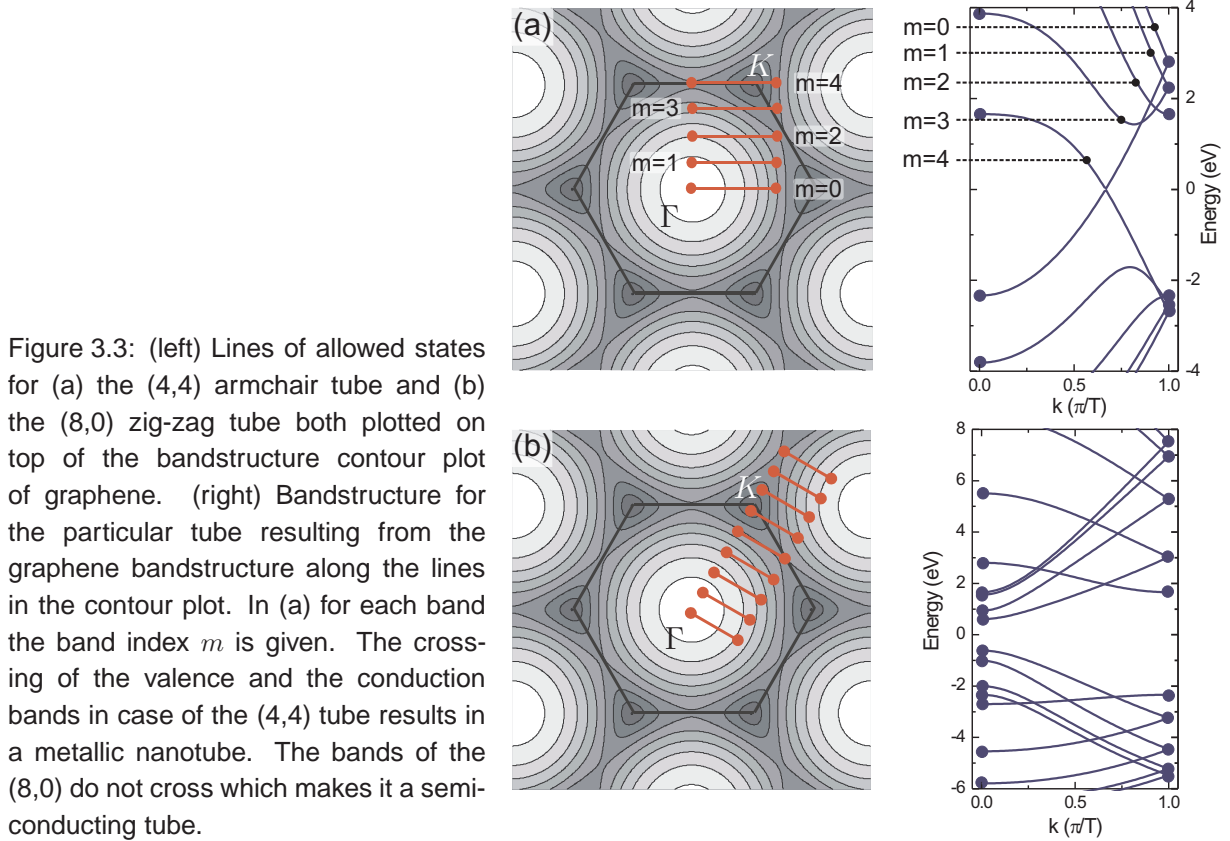


Figure 3.2: Electronic bandstructure of graphene described by a third-neighbor tight-binding model [3]. The plot shows the crossing of the valence and the conduction band at the K points.



available states due to the confinement to 1D [3]. The graphene bandstructure is usually obtained from tight-binding approximations including the first or, as in Fig. 3.2, the third nearest neighbors [46]. What makes graphene rather exceptional is the fact that the Fermi surface consists of exactly two points K and K' . Thus the valence and the conduction bands touch only at six points in the Brillouin zone, three sets of the two inequivalent high-symmetry points K and K' , which makes graphene a semimetal.

Regarding nanotubes, we have an extended (infinitely large) system solely parallel to the tube axis. Therefore we can assume a continuum of allowed wave vectors \vec{k} solely along this direction. Waves which travel along the circumference \vec{c}_h of the tube interfere destructively unless they fulfill the periodic boundary condition

$$\vec{c}_h \cdot \vec{k} = 2\pi m \quad (m \in \mathbb{N}). \quad (3.3)$$

This leaves the k -space with lines of allowed states with a distance depending on $|\vec{c}_h|$, thus the diameter d of the particular tube, $|\Delta\vec{k}| = 2/d$. The length of the lines with respect to the Brillouin zone is given by the length of the nanotube unit cell T ($2\pi/T$).

On the left of figure 3.3 we show the lines of allowed \vec{k} plotted on top of a contour plot of the bandstructure of graphene. The actual bandstructure of the particular tube, shown

on the right of Fig. 3.3, is given by the bandstructure of graphene along the lines. Since each band in the nanotube bandstructure is related to a particular line and therefore to a particular index m in Eq. 3.3, each band is named by m (band index).

In case of the (4,4) tube in Fig. 3.3 (a) the zonefolding results in a zero bandgap, while the bandstructure of the (8,0) tube in Fig. 3.3 (b) reveals a bandgap. Obviously some nanotubes are metallic while others are semiconducting, depending if the graphene K -point is among the allowed \vec{k} or not. Whether a nanotube is metallic or semiconducting can be answered by calculating ν ,

$$\nu = (n_1 - n_2) \bmod 3 \quad . \quad (3.4)$$

ν can either be -1 , $+1$ or 0 . In the latter case the tube is metallic, while in the other cases the tube is semiconducting.

3.2.2 Optical transitions

In the previous section we showed that the bandstructure of nanotubes consists of many sub-bands. However, an incident photon can only lead to transitions between particular bands m . On the one hand only light polarized parallel to the tube axis can interact with the nanotube due to the so called *antenna effect* [47]. On the other hand the band index m can only be changed by light polarized perpendicular to the tube axis. Therefore optical transitions E_{ii} are solely expected between bands with the same m [47, 48]. The indices i give the number of the involved sub-band starting to count with the sub-band closest to the Fermi level.

Fig. 3.4 (left) shows optical transition energies E_{ii} obtained by the zonefolding approximation based on a tight-binding description of graphene including the third nearest neighbors [46]. The representation of E_{ii} as a function of the tube diameter d – the so called Kataura plot – is very useful when it comes to identifying particular nanotubes (n_1, n_2) in a sample (Sect. 3.5) due to its characteristic pattern. The right of Fig. 3.4 shows a Kataura plot which we obtained experimentally by resonant Raman spectroscopy [17, 20]. Differences between theory and experiment will be discussed below in Sect. 3.2.3.

Each data point in the Kataura plot represents a transition energy of a particular nanotube (n_1, n_2) . Basically the pattern of the data points show three characteristics which are related to the optical transition E_{ii} , the nanotube family ν and the branch \mathbf{b} . The most obvious characteristic is the overall $1/d$ dependence given by the optical transitions E_{ii} , here E_{ii}^S and E_{ii}^M are transitions of semiconducting and metallic tubes, respectively.

A second characteristic feature is the formation of branches pointing towards both sides away from the $1/d$ dependence. Tubes within a particular branch have the same branch

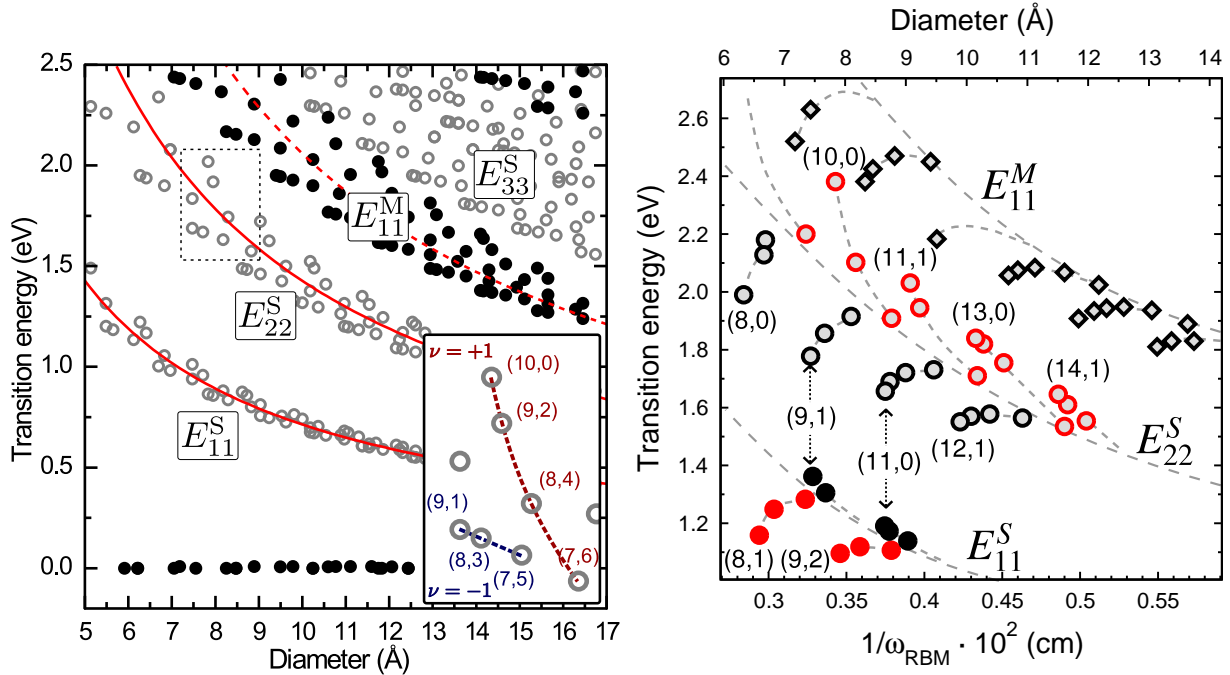


Figure 3.4: (left) Kataura plot based on the zone-folding approximation [3]. For semiconducting nanotubes (open gray circles) the first (E_{11}^S), second (E_{22}^S), and third (E_{33}^S) optical transitions are shown. For metallic nanotubes only the first optical transition E_{11}^M is contained. The red lines show the $1/d$ relation of transition energies obtained when assuming an isotropic bandstructure around the K point. In the inset a highlighted section of the Kataura is shown. It contains two branches which are related to the different nanotube families $\nu = \pm 1$. (right) experimental Kataura plot obtained by resonant Raman scattering on HiPCO nanotubes in solution [20]. Circles are transitions of semiconducting nanotubes excited into E_{11}^S (filled circles) and E_{22}^S (open circles). Semiconducting nanotubes with $\nu = +1$ are given in red, while tubes with $\nu = -1$ are black. Diamonds are the first optical transition E_{11}^M of metallic tubes.

index \mathfrak{b} , given by

$$\mathfrak{b} = 2n_1 + n_2. \quad (3.5)$$

Sometimes we name a particular branch by the nanotube (n_1, n_2) with the smallest diameter within the branch. For a given branch, the tube (m_1, m_2) next to the tube (n_1, n_2) can be calculated by

$$(m_1, m_2) = (n_1 \pm 1, n_2 \mp 2). \quad (3.6)$$

Another characteristic of the pattern in the Kataura plot is that branches of the the same nanotube family ν are bent towards the same direction. This is clearly visible in the experimental plot on the right of Fig. 3.4 where points related to nanotubes with $\nu = +1$ are colored in red while tubes with $\nu = -1$ are given by black circles. It is furthermore

noteworthy that for a given family the direction in which the branches are bent alternates when going from one transition to the next. In this way the branches with $\nu = +1$ are bent downwards in case of E_{11}^S and upwards for E_{22}^S .

3.2.3 Overview of theoretical models

Although the introduced description of the optical transitions in nanotubes is sufficient for our purposes we want to mention some more sophisticated theories, which describe a more realistic model of the electronic properties of carbon nanotubes.

A rather plausible weakness of the zonefolding approximation is the fact that it neglects the curvature of the tube walls, which would force the naturally flat sp^2 bonds to bend. This was addressed in a symmetry-adapted non-orthogonal tight-binding model developed by Popov *et al.* [49]. By considering the curved wall of the nanotubes they could improve the predictions of the optical transition energies. As this theory provides the transition energies of all nanotubes (n_1, n_2) , we also applied results from Ref. [49]. Although this theory considers changes in the electronic bandstructure due to the curved walls, it neglects deviations from the idealized atomic structure due to curvature induced weakening of the bonds. This relaxation of the atomic structure can be addressed by *ab-initio* calculations. However, for chiral nanotubes with unit cells containing more than 100 atoms, this technique is too time consuming to be applied to all (n_1, n_2) [50].

All above mentioned theories neglect electron-electron and electron-hole interaction. Recently it was predicted by theory and shown in experiments that, in fact, the optical excitations have to be treated as excitons rather than as free electron-hole-pairs [51–55]. However, theories which include many particle interactions are still quite rare and time consuming. Therefore no complete Kataura plot has been provided so far which includes curvature effects, electron-electron and electron-hole interaction. [13].

3.3 Vibrational properties and Raman effect

3.3.1 The phonon bandstructure

The phonon bandstructure of carbon nanotubes can be obtained by the zonefolding approximation based on the phonon bandstructure of graphene, in a equivalent procedure as introduced in Sect. 3.2 for the electronic bands. However, this method without any further adjustments gives rather unsatisfying results concerning the acoustic phonons. The acoustic out-of-plane vibration for instance becomes in nanotubes an optical phonon with non-zero frequency at the Γ point, which would not be obtained by simple zonefolding.

In figure 3.5 we show the phonon dispersion for the (10,10) and the (5,0) nanotube obtained from force-constant calculations [56]. Each plot contains the non-degenerate phonon branches (thick lines $m = 0$) and all subbands $m \neq 0$ (thin lines) (Eq. 3.3). As discussed above (Sect. 3.2.2) we only consider electronic transitions with $\Delta m = 0$. Therefore, the phonon involved in the first-order Raman spectrum must conserve m , why we only consider the Raman-active phonons with $m = 0$.

Since we do not expect to see the infrared-active phonon (IR) and the acoustic phonons in the first order Raman spectrum there remain three phonons which should be observed in the Raman spectrum. The two phonon branches at high energies, TO and LO, correspond to the E_{2g} (G-mode) in graphite, with the atoms vibrating parallel to the tube axis in case of the LO phonon, and perpendicular to the axis in case of the TO phonon. Due to their high energies the Raman modes corresponding to these two vibrations are also called high-energy modes (HEM) or, following their relationship to the G mode in graphite, G^- and G^+ . The phonon mode at low frequencies corresponds to the out-of-plane vibration,

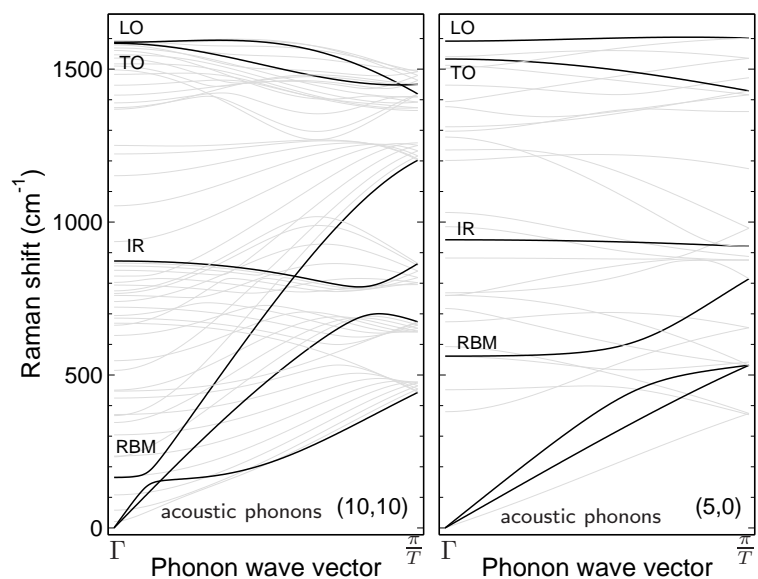


Figure 3.5: Phonon bandstructure of the (10,10) and (5,0) nanotubes obtained from force-constant calculations. The RBM as well as the TO phonon mode strongly differs between the two tubes. Both differences are due to diameter dependences of the particular modes (see Sect. 3.3.1 and 5)

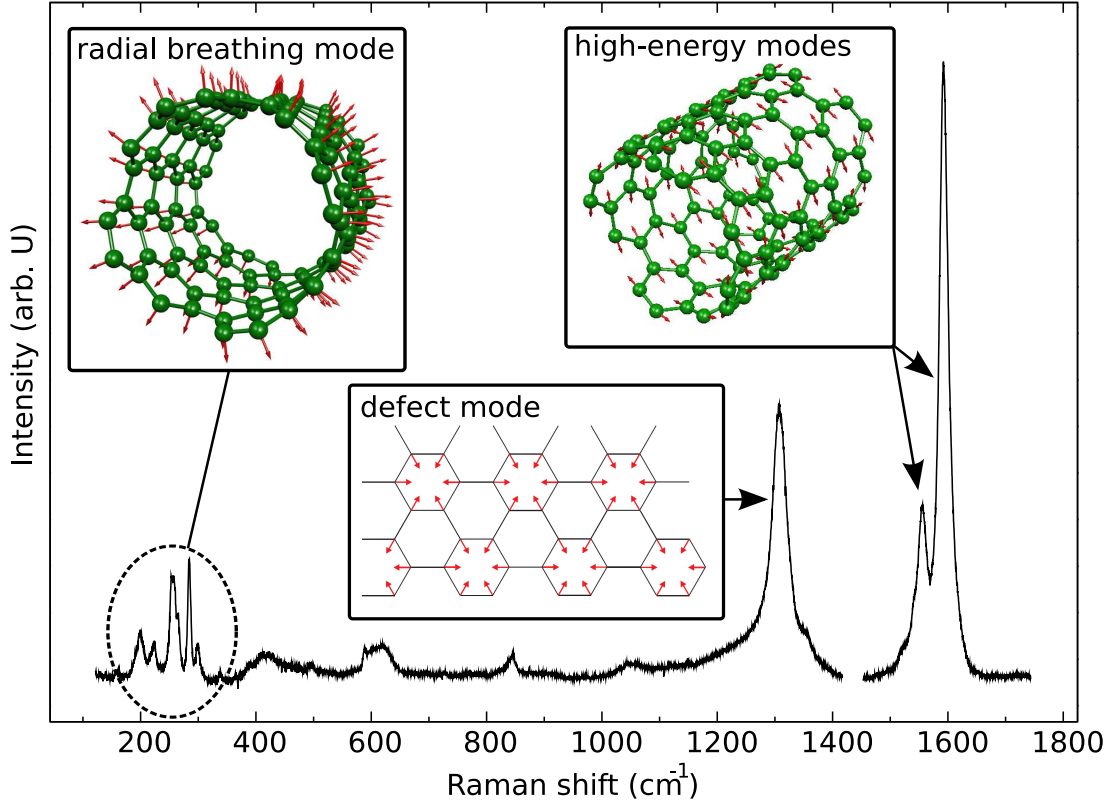


Figure 3.6: Raman spectrum taken from an ensemble of nanotubes (HiPCO) containing all (n_1, n_2) in the diameter range between 0.5 and 1.4 nm. The insets demonstrate the atomic displacement corresponding to the particular Raman mode. For the high-energy mode the inset refers to the TO-phonon which corresponds to the smaller of the two peaks.

an acoustic phonon in graphite. In nanotubes this phonon is an radial breathing-like vibration of the atoms, the so-called radial breathing mode (RBM). In nanotubes this phonon has a non-zero frequency at the Γ point and is therefore an optical phonon. Its frequency scales inversely with the nanotube diameter, see Sect. 3.3.1.

Concerning first-order Raman spectroscopy we expect to observe phonons restricted to wave vectors with $q \approx 0$. Therefore, we would expect three peaks in the nanotube Raman spectrum, the two HEM peaks near 1600 cm^{-1} and the RBM in the low energy region. Figure 3.6 shows a Raman spectrum collected from an ensemble of nanotubes, containing all nanotubes (n_1, n_2) between 0.5 and 1.5 nm. Four peaks and peak series, respectively, are distinguished. Two are the RBM and HEM at frequencies similar to those predicted by the force constants calculation. While we give a short introduction to the RBM below, there is a major discussion concerning the HEM in Sect. 5. A third mode is the defect induced mode which is correlated to a double-resonant Raman process involving phonons with $q \neq 0$ [57, 58]. Moreover, there are the intermediate frequency

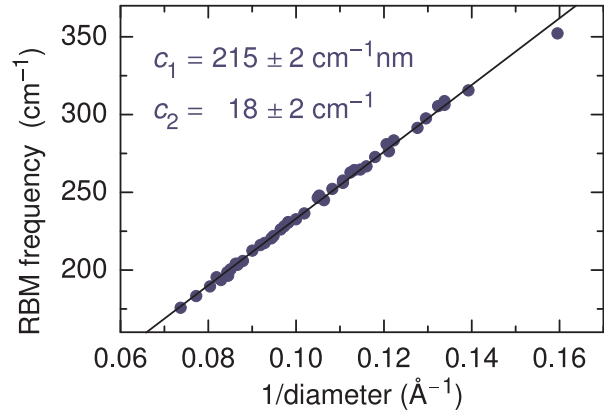


Figure 3.7: RBM frequencies as a function of inverse tube diameter $1/d$. The black line is a linear fit resulting in the parameters c_1 and c_2 . Taken from Ref. [5]

modes (IFMs), a series of peaks which are still under debate and which will be further discussed in Sect. 5.1.3 [59, 60].

Radial breathing mode

In figure 3.6 a whole series of peaks appears in the low-energy regime, where we expect the RBM. The reason for this is that the RBM frequency ω_{RBM} strongly varies for different nanotubes (n_1, n_2) . This strong variation is also seen in the theoretical data shown in Fig. 3.5.

The breathing like vibration of the RBM can be described by the harmonic oscillation of a cylinder. Solving the equation of motion for a cylinder yields an eigen frequency ω_0 of the breathing like vibration,

$$\omega_0 = \frac{c}{r} \sqrt{\kappa} \quad , \quad (3.7)$$

where c contains, in case of a nanotube, the lattice constant of graphene and the mass of the atoms per graphene unit cell. One might expect that the force constant κ depends on the nanotube chiral angle. But in fact, the force constant is independent of the chiral angle, thus it does not matter along which direction a graphene lattice is stretched, the repulsive force is always the same. Therefore ω_{RBM} solely depends on the nanotube diameter d [61].

Figure 3.7 shows experimental results for the radial breathing mode frequency as a function of tube diameter [5]. It turns out that next to the constant $c = c_1$ mentioned above we need a further parameter c_2 which includes interactions with the environment, like the van der Waals interaction with other tubes within a bundle or with an underlying substrate. Therefore, the relation of the RBM frequency and the tube diameter is given by [5]

$$\omega_{\text{RBM}} = \frac{c_1}{d} + c_2 \quad c_1 = 215 \frac{\text{nm}}{\text{cm}}, c_2 = 18 \text{ cm}^{-1} \quad . \quad (3.8)$$

Due to different conditions in different types of samples the values for c_1 and c_2 might vary in the literature [3, 62, 63].

3.4 Resonance enhancement

We assume that most, probably all, Raman modes of carbon nanotubes are only observed when they experience resonance enhancement (Sect. 2.1.3). However, full resonance profiles have so far only been collected for the RBM [19,20,64]. As discussed above, an optical excitation in carbon nanotubes is an exciton. Therefore except for the ground state there is only one discrete state involved in the resonant Raman process. Therefore a Raman resonance profile of carbon nanotubes can be described by Eq. 2.5.

3.5 Chiral-index assignment

Parts of this sections were published in Ref. [5]

There are many reasons why there is a need for a reliable way of performing an (n_1, n_2) assignment in a nanotube sample. One reason is that almost all nanotube properties which we introduced in the previous sections vary for different (n_1, n_2) . We can expect that other properties, as thermal conduction [65], transport properties [66], spin orbit coupling [67] or electron-phonon coupling (Sect. 4), to name just a few, also vary with (n_1, n_2) . Furthermore, separation and selective functionalization methods depend on a reliable method to verify their success [6, 7, 68].

There are basically three techniques to identify the nanotube structure (n_1, n_2) , photoluminescence excitation spectroscopy (PLE) [69], resonant Raman scattering [5, 20, 64] and electron diffraction [70]. While the latter method is destructive and only suitable for freely suspended isolated nanotubes or small bundles, the other two methods are nondestructive and can be applied to nanotube ensembles containing many different kinds of nanotubes (n_1, n_2) . Strictly speaking also PLE experiments are destructive, since the sample has to undergo a separation procedure, which is irreversible – till now there is no way to completely remove the surfactant [71]. Another disadvantage of PLE compared to the other two methods is that it is impossible to detect metallic nanotubes. A disadvantage of the Raman method is the experimental effort. To identify all nanotubes present in a sample, Raman spectra have to be taken at many different excitation energies, which implies the availability of tunable laser systems.

In this Section we show how to assign a particular nanotube (n_1, n_2) to an observed radial breathing mode. The reliability of the final assignment strongly depends on the sample type, the experimental capabilities and the accuracy of reference data. While the assignment of the nanotubes in a sample containing all different kinds of tubes (Sect. 4) is very reliable, there is always some uncertainty when assigning an isolated nanotube (Sect. 5.2). Regarding the experimental setup, it has to be capable of detecting low Raman shifts and of resolving the RBMs of different tubes. Therefore a triple monochromator is necessary as described in Sect. 2.2 or a setup with a Notch-filter with a low cut-off frequency. The monochromator and detection device, respectively, have to be capable to resolve two peaks separated by $\approx 2 \text{ cm}^{-1}$. Furthermore the quality depends on the available laser lines, since only those tubes can be detected which are in resonance with the laser.

The reference used for the assignment is a Kataura plot which is given by the optical transition energy E_{ii} as a function of the nanotube diameter d (see Fig. 3.4 in Sect. 3.2.2). To compare an observed RBM to the Kataura plot we either have to transfer the diameter scale in the Kataura plot to ω_{RBM} or the observed ω_{RBM} to d . This is achieved by using

Eq. 3.8, keeping in mind that the coefficients c_1 and c_2 in Eq. 3.8 might vary for different samples (Sect.3.3.1).

The assignment of ω_{RBM} to (n_1, n_2) is achieved either by pattern recognition or by simply looking for the reference data point which matches the experimental data the best. Pattern recognition is by far the more reliable method but only possible if the Raman spectrum shows a set of different RBMs. This is only the case for samples containing different kinds of nanotubes, i.e. ensembles of nanotubes. When all observed Raman spectra show only one RBM, e.g. when the sample consist of one single tube or contains only one kind of chiral indices (n_1, n_2) , the quality of the assignment depends on the chosen Kataura plot. As we discussed in Sect. 3.3.1, the RBM can slightly vary for different samples. However, much more pronounced is the effect of different environments on the the electronic transition E_{ii} (Sect. 3.6). Therefore the best choice for the reference Kataura plot is an experimental plot taken under the same conditions as the RBM peak one wants to assign. If a theoretical Kataura plot is used, it usually has to be shifted with respect to the energy scale to account for environmental effects (Sect. 3.6).

In the following we will demonstrate, how to perform an (n_1, n_2) assignment supported by pattern recognition [5]. An assignment of a single nanotube is discussed in Sect. 5.2. The top of Fig. 3.8 shows an RBM spectrum obtained from a HiPCO nanotube sample at an excitation energy of 1.96 eV. Nanotubes produced by the HiPCO method contain all types of nanotubes (n_1, n_2) within ≈ 0.5 and ≈ 1.5 nm (Sect. 4.1.5). The Kataura plot in Fig. 3.8 which we use for the assignment is obtained from the same type of sample. Therefore we assume identical RBM frequencies and transition energies E_{ii} for the tubes in the spectrum and the Kataura plot.

In the Kataura plot the excitation energy is marked by the dashed gray line. In addition we marked an energy region ΔE around the laser line where we expect to find the nanotubes (n_1, n_2) which are associated with the RBMs in the spectrum. The width of the resonance window ΔE is estimated by the sum of the width of the electronic transition linewidth (≈ 60 meV) and the energy of the RBM phonon (≈ 30 meV). If the Kataura plot is obtained from nanotubes in a different environment, the energy region has to be enlarged by the assumed energy deviation.

The pattern in the Kataura plot shows groups of nanotubes with close-by transitions and ω_{RBM} , which are due to the branches (see Sect. 3.2.2). These groups are also visible in the Raman spectrum. Therefore we can assign in Fig. 3.8 the RBMs highlighted in blue to the metallic tubes in the (15,0) branch. The first and the last tubes of the (15,0) branch are not within the resonance window ΔE . Therefore we can assign the peaks within the group of RBMs, going from left to right, to the (11,8), (12,6) and (13,4) tube. From the Kataura plot we know that also the (14,2) tube should be observed. Therefore it is

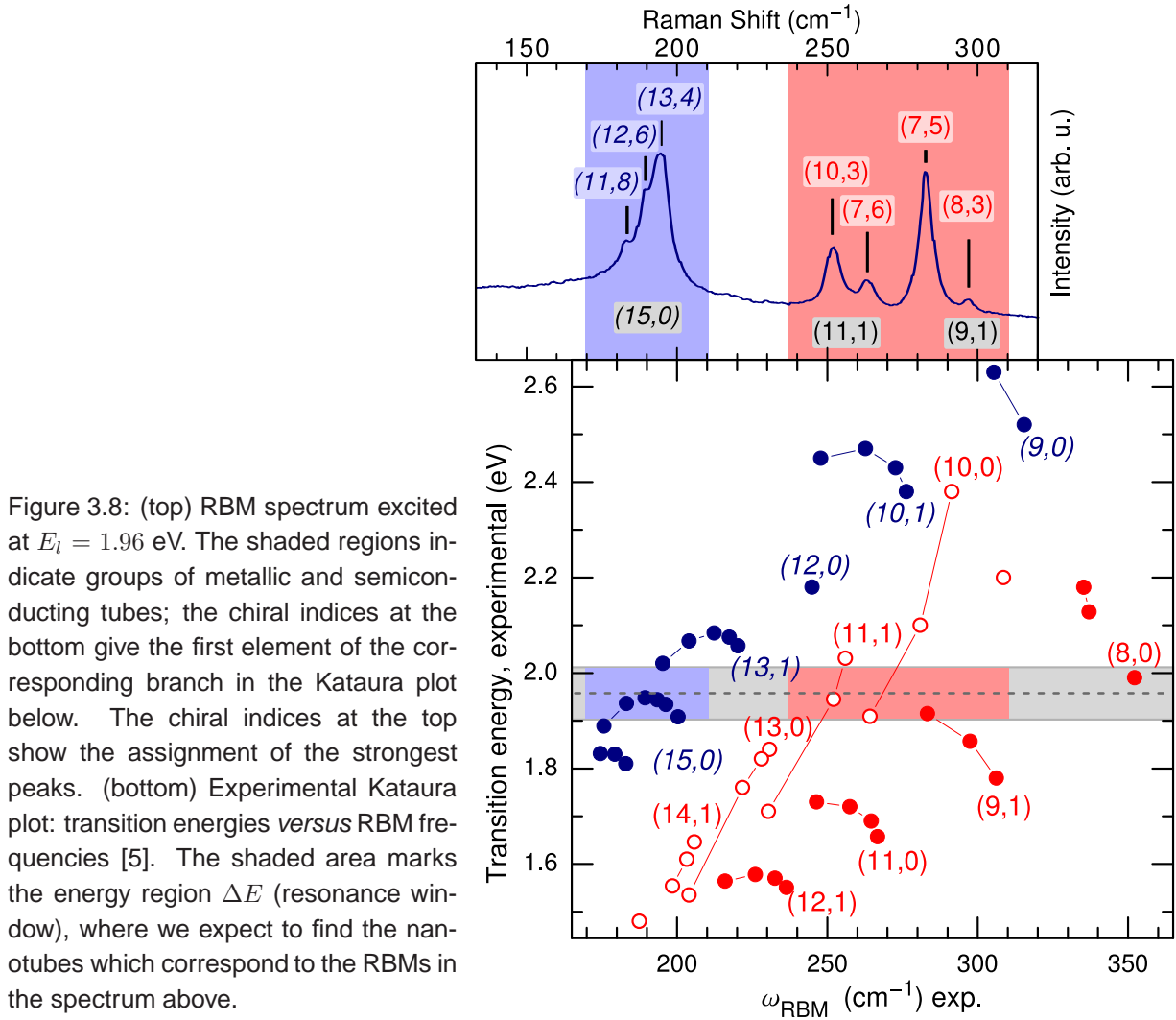


Figure 3.8: (top) RBM spectrum excited at $E_l = 1.96$ eV. The shaded regions indicate groups of metallic and semiconducting tubes; the chiral indices at the bottom give the first element of the corresponding branch in the Kataura plot below. The chiral indices at the top show the assignment of the strongest peaks. (bottom) Experimental Kataura plot: transition energies versus RBM frequencies [5]. The shaded area marks the energy region ΔE (resonance window), where we expect to find the nanotubes which correspond to the RBMs in the spectrum above.

worth adding a forth peak when fitting the spectrum. Having found a branch of tubes in the Raman spectrum is extremely useful, if the remaining RBMs do not show a branch pattern or if the E_{ii} in the Kataura plot and the sample under study are expected to deviate. Because after having found a branch, the energy region ΔE where to look for the remaining nanotubes in the RBM spectrum can be pinned down to the E_{ii} of the identified branch.

All RBMs highlighted in red in Fig. 3.8 can be assigned to semiconducting nanotubes due to the large ω_{RBM} gap to the metallic tubes, also visible in the Kataura plot. However, it might be confusing that the intensity of the (10,3) tube, which has its E_{ii} exactly at the laser energy, is smaller than the intensity of the (7,5) tube, which is hardly inside the resonance window ΔE . The reason is that the (7,5) tube belongs to the $\nu = -1$ family which shows much larger Raman intensities than the $\nu = +1$ family to which the (10,3) tube belongs (Sect. 4). Such information is especially useful when the laser line is just

between the transition energy of nanotubes with similar ω_{RBM} like e.g. the (7,5) and the (9,2) tubes. An assignment can therefore further be improved when we know the expected maximum Raman intensities, which can vary due to variation in the scattering efficiency in different nanotubes (see Sect. 4).

3.6 Environmental influences on the Kataura plot

Parts of this sections were published in Ref. [5]

The experimental Kataura plot and therefore a possible assignment can be affected in two ways, both due to changes in the nanotube environment. First, the RBM frequency and therefore the parameters c_1 and c_2 in Eq. 3.8 slightly varies for different nanotube environments [3, 62, 63]. Second, the environment causes a screening of Coulomb interactions in the tubes. This has a dramatic effect on the renormalization due to the electron-electron interaction and exciton binding energy. Therefore the measured E_{ii} differ by up to 100 meV between different samples [11, 64, 72]. Although both effects, the change in ω_{RBM} and E_{ii} , depend somewhat on the chiral indices (n_1, n_2) , the characteristic pattern of the Kataura plot remains and so does the validity of the assignment procedure introduced in the previous section.

In the following we demonstrate how the choice of surfactants influences E_{ii} and ω_{RBM} . Therefore we studied HiPCO nanotubes in aqueous solution stabilized by two different surfactants, sodium dodecyl sulfate (SDS) and sodium dodecylbenzene sulfonate (SDBS) [73]. To analyze the surfactant-induced changes in the Raman spectra, we recorded resonance profiles for both surfactants with excitation energies between 1.85 eV and 2.2 eV, see Fig. 3.9. In this region, the laser energies are in resonance with both metallic and semi-

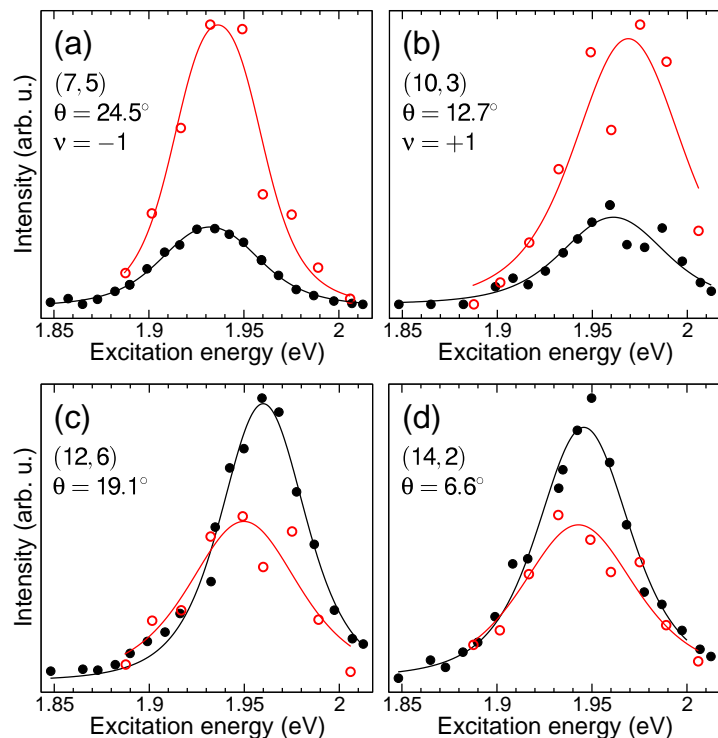


Figure 3.9: Resonance profiles of the RBM for surfactants SDS (open red dots) and SDBS (filled black dots). The chiral indices, chiral angle θ , and family ν are given. Semiconducting tubes, (a) and (b), show a small upshift of the position of the resonance maximum in case of SDS. In metallic tubes, (c) and (d), the shift of the transition energies is in opposite direction. The RBM intensity of metallic tubes is stronger in the SDBS sample, while the intensity of semiconducting tubes is stronger in the SDS sample. Since the nanotube concentration is unknown for both solutions only relative intensities can be considered.

tube	SDBS		SDS		$\Delta\omega$ (cm ⁻¹)	ΔE (meV)
	ω_{RBM} (cm ⁻¹)	E_{ii} (eV)	ω_{RBM} (cm ⁻¹)	E_{ii} (eV)		
metallic nanotubes						
(15,0)	200	1.91	203	1.91	-3	0 ± 20
(14,2)	196	1.93	199	1.93	-3	0 ± 10
(13,4)	193	1.94	196	1.93	-3	10±10
(12,6)	189.4	1.948	191.1	1.938	-1.7	10±6
(11,8)	183.2	1.936	184.1	1.906	-0.9	30±8
semiconducting nanotubes						
(8,3)	297.5	1.857	297.5	1.877	0.0	-20±13
(7,5)	283.3	1.915	283.2	1.919	0.1	-4±4
(7,6)	264.2	1.909	263.6	1.917	0.6	-8±6
(10,3)	252.1	1.945	252.1	1.953	0.0	-8±6

Table 3.2: Comparison of transition energies and RBM frequencies for different surfactants (SDS and SDBS). All transition energies are obtained from resonance profiles. The experimental errors for the first three tubes of the (15,0) branch are larger than for the majority of our data.

conducting tubes. We observe changes of (i) the transition energies, (ii) the Raman intensities, and (iii) the RBM frequencies.

In case of semiconducting tubes [Fig. 3.9(a) and (b)], the transition energies are $\approx 5 - 10$ meV larger for the solvent SDS (open red circles) compared to SDBS (black circles). Furthermore the Raman signal is stronger from the SDS samples. In case of metallic nanotubes the variations between the two solvents are the other way around, with larger transition energies and stronger signal from the SDBS sample, see table 3.2. However, the transition energy variation are small and for several tubes in particular from the metallic (15,0) branch within the experimental error.

In Fig. 3.10(a) and 3.10(b) we compare the RBM spectra for both surfactants at the same laser energy in the region of semiconducting and metallic tubes, respectively. The RBM frequency of semiconducting tubes is the same in both surfactants within experimental error (red and black curves in Fig. 3.10(a)). The relative RBM intensities, in particular from the (8,3) and the (7,5) tube, are different in these spectra, reflecting the small transition energy shift. The original intensity ratio in the SDS sample at $E_l = 1.916$ eV can be recovered if the SDBS sample is excited at a slightly lower energy ($E_l = 1.908$ eV, dashed curve). This shift of the laser energy compensates the shift in the optical transition energy of semiconducting tubes.

The dependence of the RBM frequency and intensity in metallic and semiconducting tubes on the type of surfactant agrees with the observation by Strano *et al.* [7] of selective functionalization of metallic tubes. They found a decrease of the absorption strength for the metallic E_{11}^M transitions, resulting from functionalization with tetrafluoroborate salt

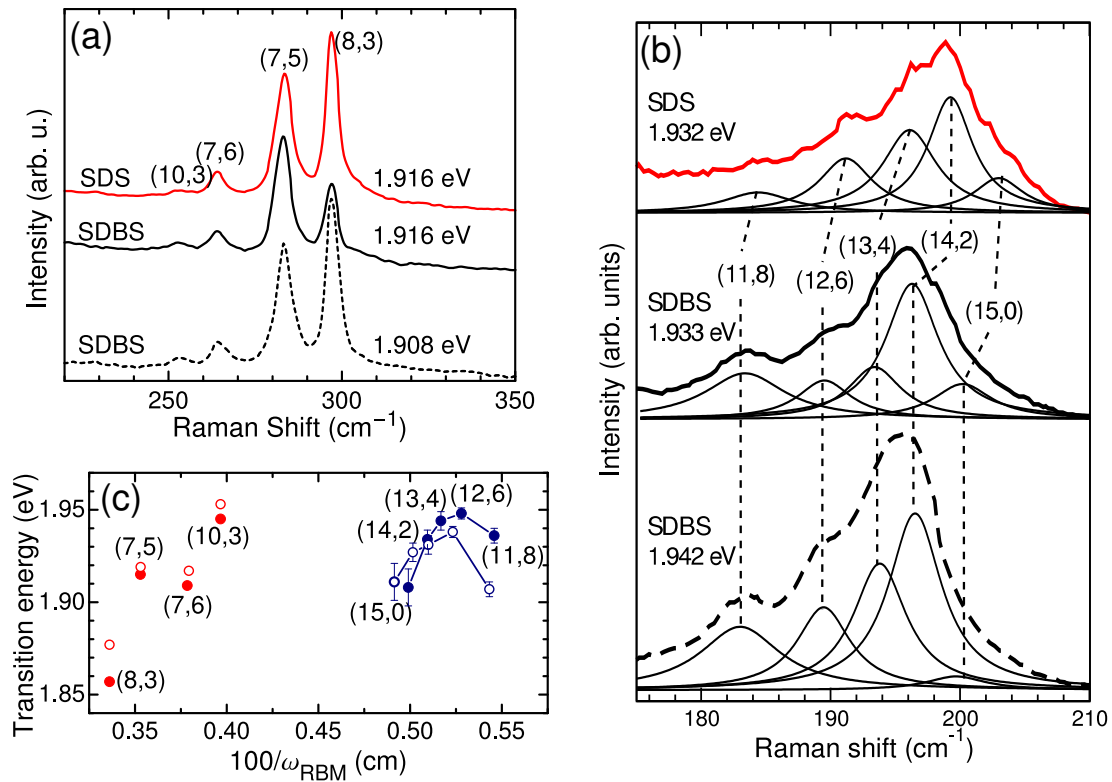


Figure 3.10: (a) RBM spectra of nanotubes dispersed in D₂O using SDBS (black) and SDS (red; gray) as surfactants at excitation energy 1.916 eV (solid lines) and 1.908 eV (dashed lines). The spectra are normalized to the RBM amplitude of the (7,5) tube. (b) Metallic part of the RBM spectrum. Red: SDS sample; black: SDBS sample. Thin lines show the fit of the RBM peaks by Lorentzians. The peaks are shifted to higher frequencies in the SDS sample. (c) Section of the Kataura plot showing the transition energy *versus* inverse RBM frequency of nanotubes in SDS (open dots) and SDBS (closed dots). Semiconducting tubes (gray, red) show a uniform shift of the transition energies. Metallic tubes (dark, blue) are shifted in energy and RBM frequency.

and formation of covalent bonds. Simultaneously, the RBM shifted to larger frequency. We can thus interpret our results as due to an interaction between the surfactant and the nanotube, which is stronger for SDS than for SDBS. Although it is unlikely that a covalent bond forms as in the case of Ref. [7], an electron transfer from the metallic tubes to the surfactant might occur. The Raman intensity decreases in SDS as the resonant absorption becomes weaker, simultaneously the interaction leads to a larger RBM frequency. From our data we cannot detect such a difference in the interaction for semiconducting tubes, as the RBM is constant when changing the surfactant.

The small shift in transition energies might be to first approximation assigned to a change in the dielectric environment. It is for several tubes within the range of experimental error. We have no explanation yet for the shift in opposite direction for metallic

and semiconducting tubes.

Izard *et al.* [74] studied the development of RBM spectra from bundled tubes to bundles wrapped by SDS and to individual tubes in SDS. They also observed an upshift of the RBM due to wrapping by SDS which they assigned to pressure induced by the surfactant. The metallic tubes appear to be more sensitive to the surfactant, as the RBM shift is in general larger than for semiconducting tubes, in agreement with our results. Izard *et al.* [74] observed changes in the relative RBM intensities as well, which they ascribed to a selective exfoliation process. From our data, we rather suggest a small change in resonance condition.

Figure 3.10(c) shows a small section of the Kataura plot with data from SDS (open dots) and from SDBS (closed dots). The differences in transition energies and RBM frequencies are minor on the scale of the Kataura plot. However, we can expect larger differences for other environments, e.g. nanotubes (bucky-paper), air or Si-substrate. Assuming a mono-chiral dispersion of nanotubes – sample containing only one (n_1, n_2) – the variations of ω_{RBM} in metallic tubes between the two solvents is large enough to cause uncertainty in the assignment, unless the Kataura plot used for the assignment is based on the same sample type. Fig. 3.10(b) shows that for instance the (13,4) tube could easily be assigned to the (14,2) tube if there were no other RBMs enabling a pattern recognition. On the other hand, even if the (13,4) and the (14,2) tube were confused in the assignment, this would in most cases not effect conclusions drawn about other physical properties. As these tubes are neighboring tubes in the same Kataura branch, the physical properties are expected to be similar.

Chapter 4

Raman intensities of the radial breathing mode: scattering efficiency *versus* (n_1, n_2) abundance

Large effort is devoted to controlling the atomic structure - the chiral index (n_1, n_2) [3] - of carbon nanotubes either during the growth process [75–77] or by sorting the tubes by subsequent chemical treatment [8], electrophoresis [6], density gradient [78], selective solubility [79] or chromatography of DNA-wrapped tubes [14]. In spite of constant progress, most nanotube samples contain a large variety of different chiral indices (n_1, n_2) . Common techniques to probe the chiral indices in a nanotube ensemble are photoluminescence excitation (PLE) [69] and resonance Raman spectroscopy (RRS) [5, 20, 64] (Sect. 3.5). In order to check if a growth or separation process favors a certain type of nanotube, a technique is needed to probe the abundances of different nanotube (n_1, n_2) in a sample. In principle this can be achieved by studying the signal intensities from PLE or RRS experiments.

Theoretical predictions show that the signal strength in PLE and Raman spectra depend on nanotube properties like the diameter d , chiral angle θ , family ν and the optical transition E_{ii} [21, 22, 50]. Therefore the intensities in PLE and RRS spectra obtained from a sample with uniform (n_1, n_2) abundances can give information on (n_1, n_2) specific properties. The absorption and emission efficiency for example, which can be obtained from the PLE intensities, are important parameters for the use of nanotubes as a light emitter or in conducting transparent films. The Raman intensities give, in addition to the absorption efficiency, information about the electron-phonon (e-ph) coupling. The e-ph coupling in turn plays an important role in the understanding of relaxation processes,

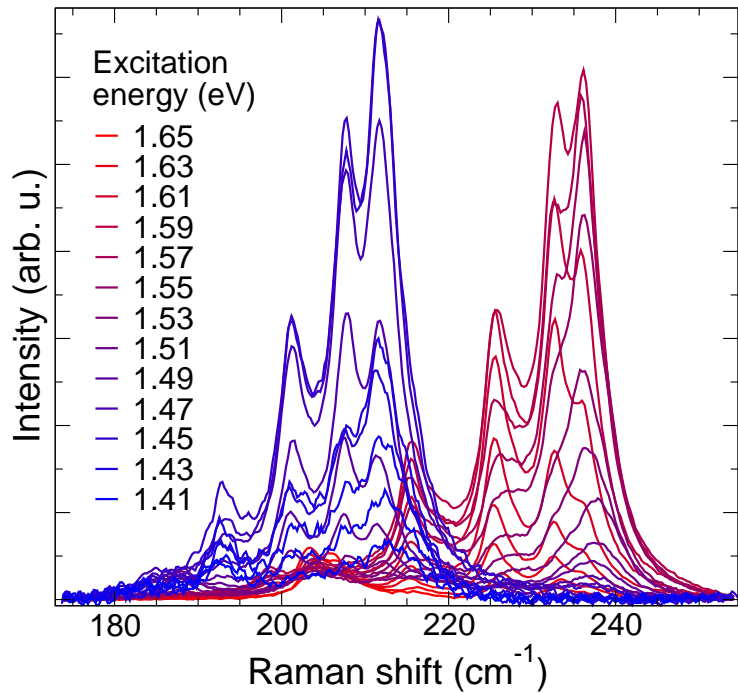


Figure 4.1: Raman spectra of the radial breathing mode of HiPCO carbon nanotubes in solution. The spectra are normalized to the integration time t , the laser power P_i and the system responds (see Sect. 2.1.2).

which influence emission efficiencies, and scattering processes in electron transport.

In this chapter we show that the maximum Raman intensities observed from different (n_1, n_2) nanotubes in a nanotube ensemble strongly vary from tube to tube. The problem we face is that we can not tell if these variations are due to different (n_1, n_2) abundances or due to different scattering efficiencies of different (n_1, n_2) nanotubes. In Sect. 4.1 we will discuss the behavior of the scattering efficiency based on the assumption that the sample has a uniform (n_1, n_2) distribution [5, 17, 18, 20, 80]. In Sect. 4.2 we will discuss the issue of how to determine differences in the abundances for different (n_1, n_2) nanotubes.

4.1 Raman susceptibility

Resonant Raman spectroscopy (RRS) of the radial breathing mode (RBM) in carbon nanotubes is an established method to determine the nanotubes species in a sample [5]. To assign each observed RBM to a particular (n_1, n_2) , the RBM frequency is correlated with the transition energy, obtained from the RBM intensity as a function of excitation energy, as described in Sect 3.5. From the perspective of fundamental research as well as sample characterization it is of interest to further study the Raman intensities of the RBMs. When the Raman signal is processed as described in Sect. 2.1.2 the signal is proportional to the Raman susceptibility χ_R . The Raman susceptibility as a function of excitation energy gives information on basic material properties as the absorption efficiency, the coupling-strength between carriers and phonons, and the lifetime of excited states.

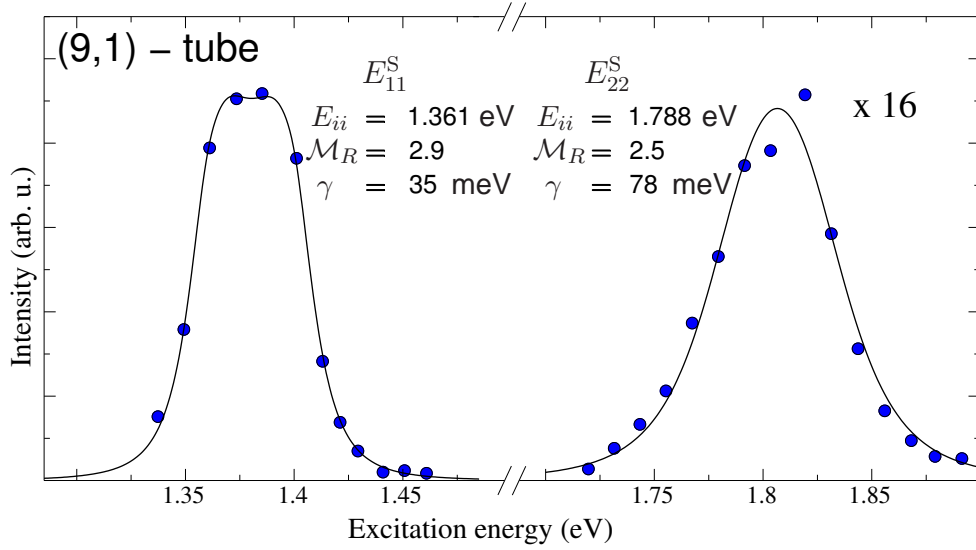


Figure 4.2: Raman intensity profile of the first and second optical transition, E_{11}^S and E_{22}^S , of the (9,1)-tube. E_{ii} , \mathcal{M}_R and γ are fit parameters obtained from fitting Eq. 2.4 to the intensity profile (solid lines). The intensity of the E_{22}^S profile is multiplied by 16.

In order to study these material properties for different (n_1, n_2) nanotubes we performed Raman experiments on an ensemble of nanotubes. The sample was produced by the HiPCO method which provides all different (n_1, n_2) within a diameter range between ≈ 0.5 and ≈ 1.5 nm. To avoid tube-tube interactions, which broaden resonance windows and therefore lower the signal strength [72], the tubes were ultrasonically dispersed in D_2O and stabilized in sodium dodecyl sulfate (SDS) micelles [71, 73]. Furthermore, in comparison to aggregated nanotubes, dissolved tubes allow the use of much higher laser powers than bundled tubes without effecting the properties of the sample. While the Raman spectra of nanotubes in solution show no observable change up to at least 50 mW excitation power, in aggregated tubes the peaks start to broaden and downshift already above 1 mW, which indicates heating of the sample.

Spectra of the RBMs were collected at excitation energies between 1.15 and 2.15 eV at intervals of 5-15 meV and laser power P_i up to 40 mW. Therefore we used the setup described in Sect. 2.2 in macro configuration and backscattering geometry. Figure 4.1 shows a selection of spectra excited with laser energies between 1.41 and 1.65 eV. All spectra are normalized to the integration time t , the laser power P_i and the system responds. In order to obtain data which are proportional to the square of the Raman susceptibility $|\chi_R|^2$ we further processed the RBM peak intensities – the area of a Lorentzian fit – by normalizing to the inverse Raman shift $\omega_{ph,RBM}^{-1}$ and the Bose occupation number according to Sect. 2.1.2.

Figure 4.1 shows how each of the RBMs has its maximum intensity at a certain laser

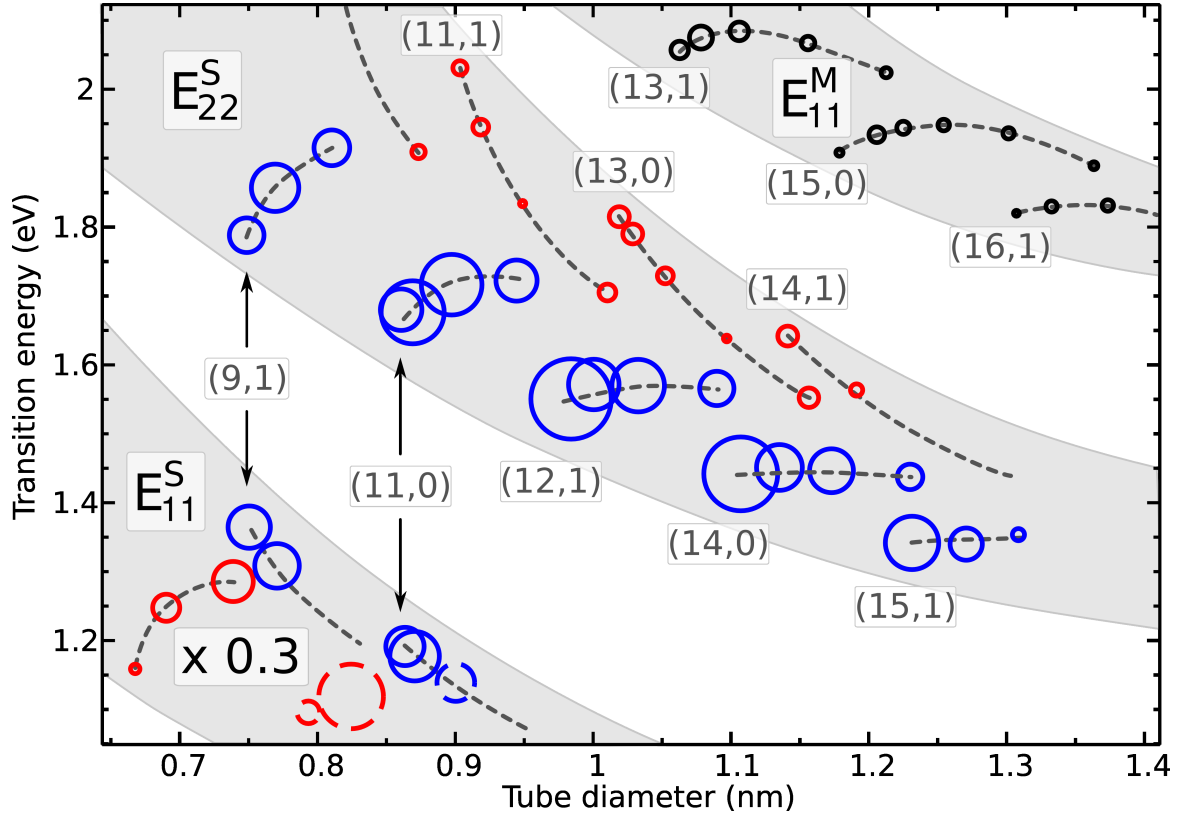


Figure 4.3: Experimental Kataura plot, where the maximum Raman susceptibility $|\chi_R^{max}|$ is given by the diameter of the circles. The first and second electronic transition, E_{11}^S and E_{22}^S , of semiconducting tubes and the first electronic transition of metallic tubes are highlighted in gray. Red and blue symbols represent semiconducting nanotubes of the different nanotube families $\nu = +1$ (red) and $\nu = -1$ (blue). Raman intensities of E_{11}^S are scaled by a factor 0.3. Branches are labeled by the tube with the smallest diameter within the branch. The members of each branch are connected by dashed lines.

energy which corresponds to the fact that the origin of the RBM is a resonant Raman process (Sect. 2.1.3). Plotting the square of the Raman susceptibility $|\chi_R|^2$ as a function of excitation energy yields a intensity profile as shown in Fig. 4.2. From fitting the formula for the resonance profile (Eq. 2.5) to the experimental data we get for each observed RBM the optical transition energy E_{ii} , the broadening γ of this transition and the value \mathcal{M}_R which is proportional to the Raman matrix element, see Sect. 2.1.3.

Correlating E_{ii} with the nanotube diameter, which we obtain from the RBM frequency ω_{RBM} using Eq. 3.8, we can produce a Kataura plot (Sect. 3.2) shown in Fig. 4.3. In addition Fig. 4.3 contains the maximum Raman susceptibility $|\chi_R^{max}|$ for each RBM. $|\chi_R^{max}|$ is proportional to the symbol diameter. Therefore the area of the symbols is proportional to the square of $|\chi_R^{max}|$ which is similar to the maximum Raman intensity of the particular

RBM as it is observed in the experiment.¹ According to Sect. 3.5 we assigned each data point to a particular (n_1, n_2) nanotube. Based on the assignment we can distinguish between the first and second optical transitions of semiconducting nanotubes, E_{11}^S and E_{22}^S , and the first optical transition of metallic tubes E_{11}^M . Furthermore we distinguish between the nanotube families $\nu = +1$ (red symbols) and $\nu = -1$ (blue symbols). For some branches we give (n_1, n_2) of the nanotube with the smallest diameter within the branch. The (n_1, n_2) of other nanotubes within a branch can be calculated using Eq. 3.6.

Fig. 4.3 shows strong differences of $|\chi_R^{max}|$ between the different (n_1, n_2) nanotubes. However, these differences refer more to the nanotube groups rather than the particular (n_1, n_2) of a nanotube. Therefore we discuss below the dependence of $|\chi_R^{max}|$ on the optical transitions E_{ii} , the nanotube family $\nu = \pm 1$, the chiral angle θ , whether a nanotube is metallic or semiconducting and the nanotube diameter d .

4.1.1 Dependence of $|\chi_R^{max}|$ on the Optical Transition E_{ii}

In Fig. 4.3, the maximum Raman susceptibility $|\chi_R^{max}|$ of the first optical transition in semiconducting nanotubes E_{11}^S is scaled by a factor of 0.3. Therefore the most obvious difference in $|\chi_R^{max}|$ is seen between the first and second optical transitions of semiconducting nanotubes E_{11}^S and E_{22}^S , respectively. This difference is even more pronounced in Fig. 4.2 where we compare the intensity profiles of the E_{11}^S (left) and the E_{22}^S (right) transitions of the (9,1) nanotube. The maximum Raman intensity of the E_{11}^S transition is ≈ 16 times larger than the intensity of the E_{22}^S transition. From this result one might be tempted to deduce a stronger electron-phonon coupling or absorption strength in case of E_{11}^S . An indication that this is not the case is given by the slopes of the resonance profiles. Obviously the slope of the E_{11}^S intensity profile is much steeper than that of the E_{22}^S profile (the relative scale of the energy axes is the same for E_{11}^S and E_{22}^S in Fig. 4.2). This corresponds to a change in the broadening parameter γ of the underlying electronic transition.

In Fig. 4.2 we also show the graph of the resonance profile Eq. 2.5 fit to the experimental data. The fit results \mathcal{M}_R and γ , also given in Fig. 4.2, show that in fact the Raman matrix elements \mathcal{M}_R are similar for E_{11}^S and E_{22}^S . The strong intensity difference is mainly due to the change in γ , which is for E_{22}^S approximately twice as large as for E_{11}^S . γ is the imaginary part of the electronic transition energy E_{11}^S and thus related to the lifetime of the transition. The observed change in γ can be interpreted as longer lifetimes of excitations in the first excitonic state - a result which is also known from time resolved measurements [81]. We

¹In Fig. 4.3 We show the maximum susceptibility $|\chi_R^{max}|$ instead of the matrix elements \mathcal{M}_R , because \mathcal{M}_R is very sensitive to changes in γ . Therefore the use of \mathcal{M}_R in Fig. 4.3 would introduce significant errors. Variations of γ and the matrix element \mathcal{M}_R are discussed in the text.

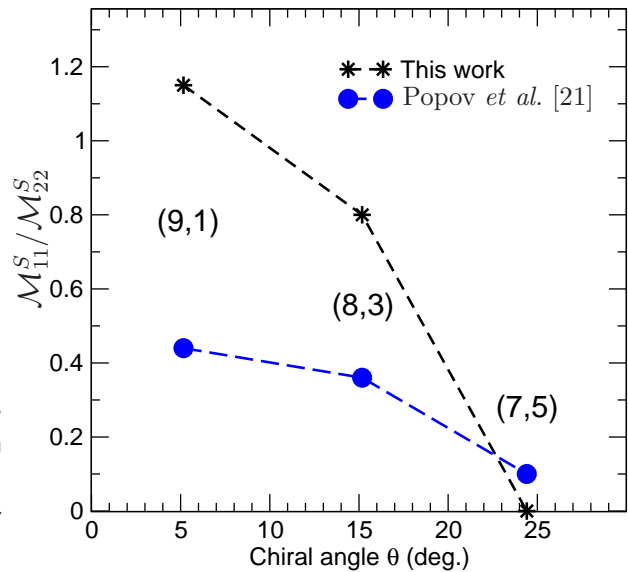


Figure 4.4: Ratio of the Raman matrix elements \mathcal{M}_{11}^S and \mathcal{M}_{22}^S for tubes within the (9,1) branch (stars). Matrix elements were obtained by fitting Eq. 2.4 to RBM intensity profiles of the particular tubes. Circles are results from Ref. [21].

do not give absolute values for the lifetime since γ is affected by inhomogeneities in the sample like the formation of small bundles and varying tube length. Differences in the sample quality might also be the reason for deviations between our results and result from Satishkumar *et al.* [82]. They observed intensity ratios I_{11}/I_{22} twice as large as ours and an accordingly smaller line width of E_{11}^S . Interestingly, their values for γ of the second optical transitions do not differ significantly from our results. Apparently the (shorter) lifetime of the E_{22}^S -exciton is much less affected by environmental changes.

As discussed in the introduction of this chapter all presented experimental Raman intensities are possibly affected by variations of the (n_1, n_2) abundances. However, the ratio between the matrix elements \mathcal{M}_R of the different optical transitions in a particular tube are not affected by the abundance of the tube. Therefore to study the ratio $\mathcal{M}_{11}^S / \mathcal{M}_{22}^S$ is a useful tool to check the validity of a theoretical model.

In Fig. 4.4 we show the ratio $\mathcal{M}_{11}^S / \mathcal{M}_{22}^S$ as a function of chiral angle of our experimental results and predictions from Popov *et al.* [21]. Matrix elements published in Ref. [21] are based on a non-orthogonal tight binding model, which does not include electron-electron and electron-hole interactions. However, the theoretical values show the same trend as the experimental values. But the predicted values underestimates the experimental findings by a factor of ≈ 2 . Unfortunately, published theoretical work, which include electron-electron and electron-hole interactions, does not report values for both the first and the second optical transitions [22].

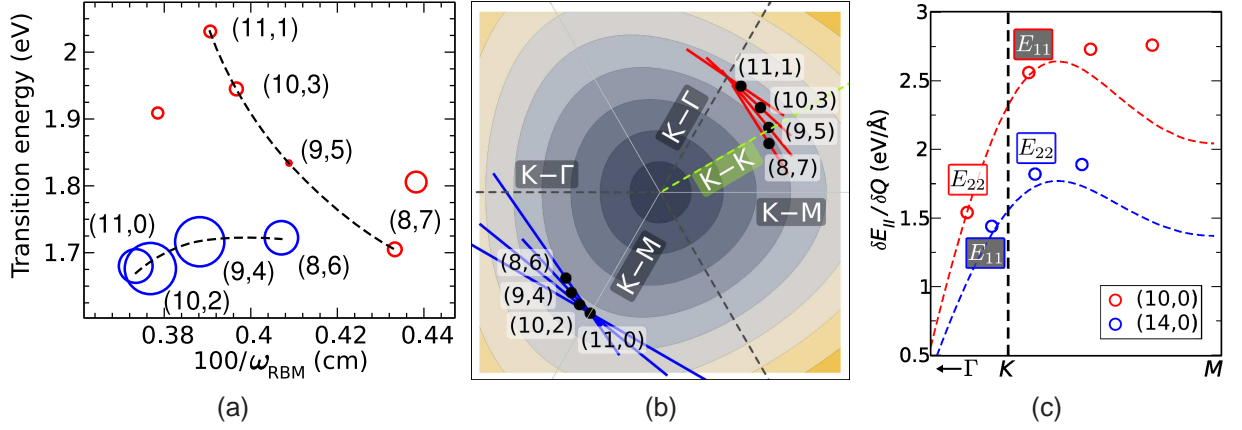


Figure 4.5: (a) Section of the Kataura plot in Fig. 4.3 showing the second optical transitions E_{22}^S of the $(11,0)$ ($\nu = -1$) and the $(11,1)$ ($\nu = +1$) branch. Tubes referring to these two branches are labeled by their particular (n_1, n_2) . (b) Contour plot of the graphene bandstructure around the K point. The lines show the allowed states of the particulate (n_1, n_2) which are related to the second optical transition. The position of the nanotube band minima and thus the places where the optical transitions take place are given by the black dots. (c) Deformation potential (\propto electron-phonon coupling) of the RBM in the $(10,0)$ ($\nu = +1$) and $(14,0)$ ($\nu = -1$) tube as a function of the position in k -space. Circles are results from *ab-initio* calculations, dashed lines from zone-folding on the tight-binding description of graphene [83].

4.1.2 Dependence of $|\chi_R^{\max}|$ on the Family ν

The second most noticeable difference of the Raman susceptibility $|\chi_R^{\max}|$ is observed for the different nanotube families $\nu = (n_1 - n_2) \bmod 3 = \pm 1$. When semiconducting nanotubes are excited resonantly into the second optical transition E_{22}^S , the maximum Raman susceptibility $|\chi_R^{\max}|$ of nanotubes belonging to the family with $\nu = -1$ (open blue circles in Fig. 4.3) is by a factor of ≈ 3 larger than that of nanotubes with $\nu = +1$ (open red circles). Fig. 4.5a shows a section of Fig. 4.3 including the $(11,0)$ and the $(11,1)$ branch representing branches with $\nu = -1$ and $\nu = +1$, respectively.

The reason for the intensity difference between the families can be understood when plotting the lines of the allowed states of each tube in the Brillouin zone of the electronic band structure of graphene as it is done in the zone folding approximation (Sect. 3.2). In Fig. 4.5b we show a contour plot of the band structure of graphene in the vicinity of the K point. In addition we plot the lines of allowed states of E_{22}^S for the $(11,0)$ branch ($\nu = -1$) and the $(11,1)$ branch ($\nu = +1$). Note that these tubes have similar diameters, for which reason we can exclude effects due to diameter related variations in the abundances, the electron-phonon coupling or absorption strength.

In Fig. 4.5b we see that the transitions of the tubes with $\nu = +1$ and $\nu = -1$ are located on opposing sides with respect to the K point. The E_{22}^S transitions of $\nu = +1$ nanotubes are located closer to the $K-\Gamma$ direction while nanotubes with $\nu = -1$ are located closer

to the K - M direction. *Ab-initio* calculations of the electron-phonon coupling reported by Machón *et al.* [50] show a significant difference between electronic states located on the K - Γ and those located on the K - M symmetry direction of graphene. Fig. 4.5c shows the results from Ref. [50] for the electron-phonon matrix elements of the (19,0)-tube, which has $\nu = +1$, and the (17,0)-tube, which has $\nu = -1$. As for the (11,0) and the (11,1) in our example, the positions for a given transition of the (19,0) and (17,0) tubes are located on opposing sides of the K point. As the electron-phonon coupling strongly differs on the two sides we can expect in case of E_{22}^S weaker signal from $\nu = +1$ nanotubes than from $\nu = -1$ nanotubes, which is in agreement with our results.

The positions of two consecutive transitions of a particular nanotube, e.g. E_{22}^S and E_{11}^S , are on opposing sides of the K point. Therefore tubes with $\nu = -1$, which have strong signal when excited into E_{22}^S , are expected to have weak signal when excited into E_{11}^S . In case of tubes with $\nu = +1$ it is the other way around. Fig. 4.3 shows that in case of E_{11}^S , the branches which are bent downwards have stronger signal than branches which are pointing upwards, which in fact is the same finding as for E_{22}^S . However, as indicated by the colors of the symbols, branches which are pointing downwards have $\nu = +1$ in case of in E_{11}^S and $\nu = -1$ in E_{22}^S . Therefore we see the expected change of signal strength between the tube families $\nu = \pm 1$ when going from E_{22}^S to E_{11}^S .

Furthermore, in Fig. 4.3 we see that the intensity difference between the families $\nu = \pm 1$ is much weaker in case of E_{11}^S compared to E_{22}^S . This can be understood when studying the calculations by Machón *et al.* [50], shown in Fig. 4.5c. Since transitions for a particular ii of two tubes, one with $\nu = +1$ the other with $\nu = -1$, are located on opposing sides of the K point, the difference in electron-phonon coupling between the two tubes increases with increasing distance to the K point. As the distance to the K point increases with increasing ii , the deviations of the electron-phonon coupling between the two families $\nu = \pm 1$ is expected to be smaller for E_{22}^S than for E_{11}^S , as observed in the experiment.

4.1.3 Dependence of $|\chi_R^{max}|$ on the Chiral Angle

Within a branch of semiconducting nanotubes the chiral angle θ of the tubes changes from $\gtrsim 0^\circ$ to $\lesssim 30^\circ$ when going from the small diameter end, which is bent away from the $1/d$ relation, to the large diameter end, where the $\nu = \pm 1$ families almost touch the $1/d$ relation. In Fig 4.6a we show the dependence of $|\chi|_{22}^{max}$ on the chiral angle θ for tubes from four branches. Two of them, the (11,0) and (12,1) branches, belong to the $\nu = -1$ family, the other two, the (11,1) and (13,0) branches, to the $\nu = +1$ family. Besides the deviation of $|\chi|_{22}^{max}$ between the nanotube families $\nu = \pm 1$, discussed above, a dependence on the chiral angle is seen. The branches with $\nu = -1$ show an increase of the signal when going from large to small θ with a sudden decrease for zig-zag tubes ($\theta = 0$). In case of

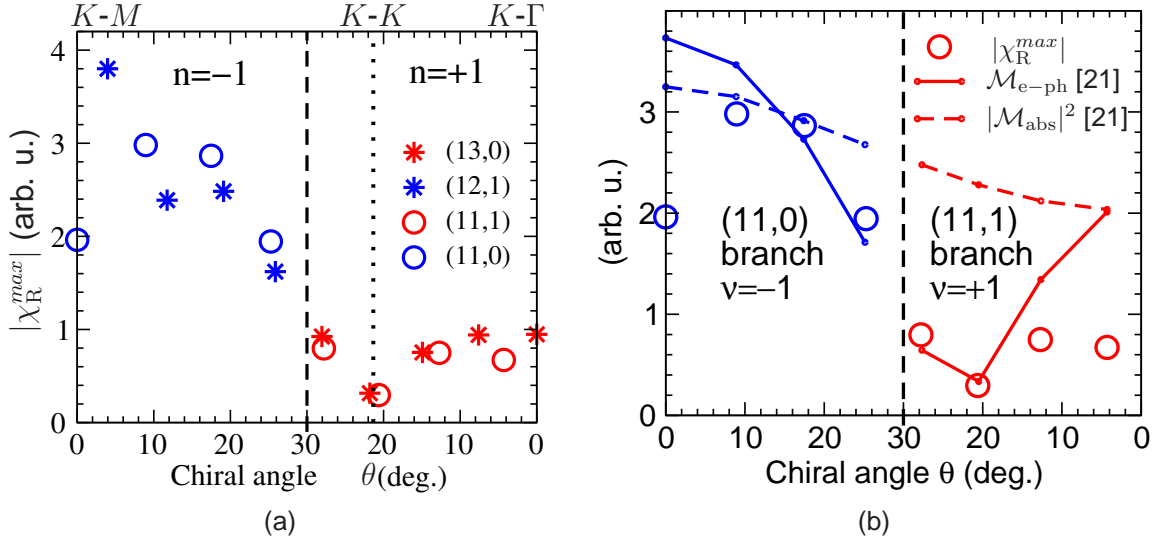
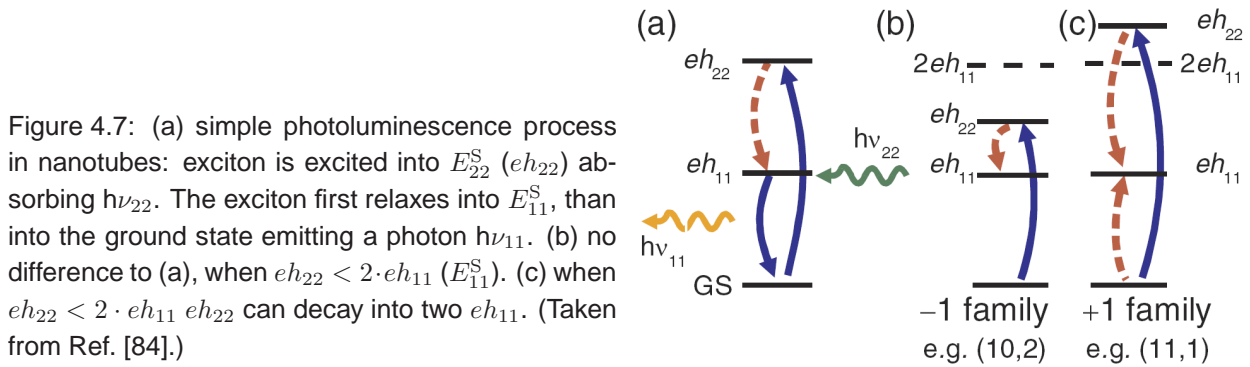


Figure 4.6: Maximum Raman susceptibility $|\chi_R^{max}|$ as a function of chiral angle θ . (a) $|\chi_R^{max}|$ for tubes of four nanotube branches excited into E_{22}^S . Tubes with $\nu = -1$ are on the left, tubes with $\nu = +1$ on the right of the vertical dashed line. The dotted line marks the chiral angle where $|\chi_R^{max}|$ is at minimum. (b) Comparison of $|\chi_R^{max}|$ to predictions on the electron-phonon coupling M_{e-ph} and absorption strength M_{abs} from Ref. [21].

the $\nu = +1$, $|\chi_{22}^{max}|$ appears to be rather independent of θ with one exception. Nanotubes with $\theta \approx 20^\circ$ have ≈ 3 times weaker $|\chi_{22}^{max}|$ than tubes with other chiral angles.

In order to understand this finding we again consider the picture of the positions of the transitions in the graphene Brillouin zone with respect to the K point, Fig. 4.5b. In this picture going from $\theta = 0^\circ$ to $\theta = 30^\circ$ within a $\nu = -1$ branch implies a change of the position of the transition from the $K-M$ to the $K-K$ direction. Within a $\nu = +1$ family this means a change of the transition from the $K-\Gamma$ to the $K-K$ directions. Therefore the dependence of $|\chi_{22}^{max}|$ as a function of the chiral angle θ in Fig. 4.6a can be understood as $|\chi_{22}^{max}|$ as a function of the position of the transition in the graphene k -space going from the $K-M$ to the $K-\Gamma$ direction. Fig. 4.5b shows that the $(9,5)$ tube ($\nu = +1$ and $\theta = 20.6^\circ$), which represents the minimum in Fig. 4.6a, has its E_{22}^S transition very close to the $K-K$ direction. Calculations presented by Popov *et al.* [21] show that in case of E_{22}^S the matrix element M_{e-ph} changes sign within a $\nu = +1$ family for nanotubes close to $\approx 20^\circ$. Therefore our results suggest that the change of sign happens exactly at the $K-K$ direction.

Assuming the band structure of graphene to be symmetric around the K point, we would expect armchair tubes to have transitions exactly on the $K-K$ direction. In Sect. 3.2 we showed that the band structure actually undergoes a trigonal warping, which is the reason why the transitions of all tubes except for zig-zag tubes are shifted towards the $K-M$ direction. Therefore the transitions of nanotubes with $\theta \approx 20^\circ$ with either $\nu = +1$



ore $\nu = -1$ are shifted onto the K - K direction. Whether the particular nanotube belongs to $\nu = +1$ or $\nu = -1$ depends on the optical transition and alternates between consecutive transitions. In case of E_{11}^S the tube with the smallest $|\chi|_{11}^{max}$ has $\nu = -1$ while the tube with the smallest $|\chi|_{22}^{max}$ has $\nu = +1$.

In figure 4.6b we compare our results on the Raman susceptibility $|\chi|_{22}^{max}$ of the (11,0) ($\nu = -1$) and (11,1) ($\nu = +1$) to predictions from Popov *et al.* [21].² The predicted data already represent the general trend of $|\chi|_{22}^{max}$ as a function of θ and ν when only the electron-phonon coupling is taken into account (solid lines). The agreement between theory and experiment slightly improves when also the absorption strength is taken into account, which shows a weak dependence on θ and ν (dashed lines). It is noticeable, that the theoretical data strongly deviates from the experimental results in case of small chiral angled tubes. Also results from Jiang *et al.* [22], which in contrast to Ref. [21] include electron-hole interactions, do not reproduce our experimental results either.

A possible explanation of the strong deviation is given by Reich *et al.* [84]. They suggested the weak $|\chi|_{22}^{max}$ (and PLE signal) of small chiral angle tubes with $\nu = +1$ to be due to exciton-exciton interactions. They introduced an additional decay channel for the E_{22}^S excitons of tubes with $E_{22}^S \geq 2E_{11}^S$. These excitons may decay into two E_{11}^S excitons (Fig. 4.7), which causes a decrease of the absorption strength and therefore the Raman signal.

4.1.4 Metallic *versus* Semiconducting Nanotubes

Although all metallic nanotubes belong to the same family $\nu = 0$, they show in the Kataura plot the same pattern of upwards and downwards bent branches as semiconducting nanotubes (Sect. 3.2). However, in contrast to semiconducting nanotubes the lower and upper branches belong to the same tubes. Therefore each metallic nanotube contributes with a pair of transition, one in the lower branch and one in the upper branch, both at the

²Note that due to the uncertainty regarding the nanotube concentration in the experiment, experimental data can not be compared to theoretical data in terms of absolute values.

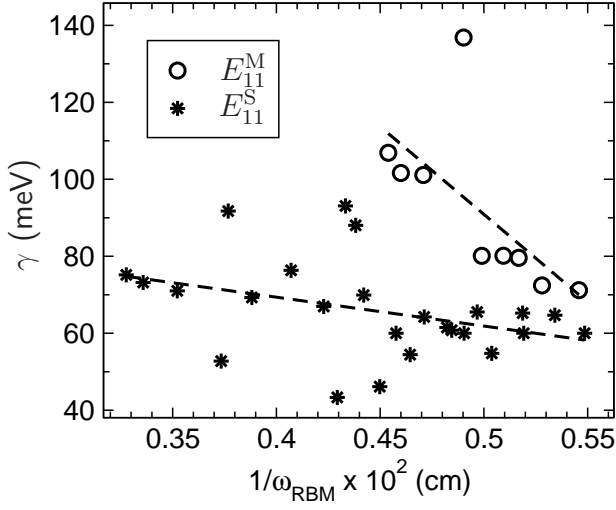


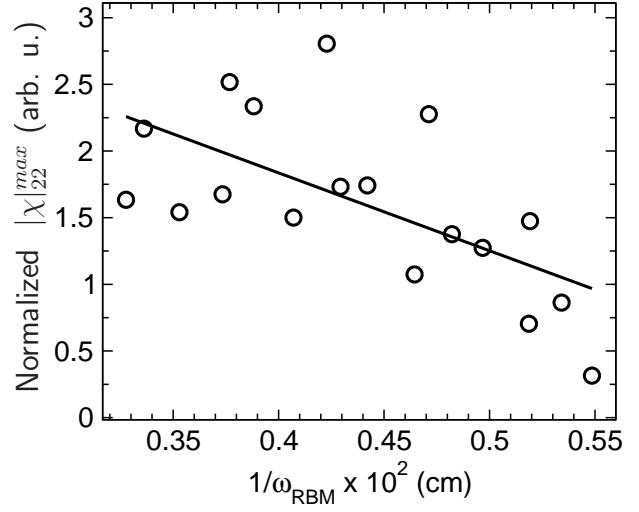
Figure 4.8: Broadening parameter γ as a function of $1/\omega_{\text{RBM}}$, thus d , for semiconducting nanotubes excited into E_{22}^S and metallic tubes excited into E_{11}^S . γ is obtained from fitting 2.5 to RBM intensity profiles. Dashed lines are linear fits.

same RBM frequency (diameter), of course. Similar to semiconducting nanotubes metallic tubes have larger $|\chi_R^{\text{max}}|$ for tubes in the branches which are bent downwards (Fig. 4.3). In fact, we did not observe the upper branches at all. Doorn *et al.* [85] presented results on the upper branches of metallic nanotubes. They used tubes produced by the so-called supergrowth method [86] which are presumed to have very little tube-tube interactions [63]. Therefore they attribute the observation of the upper branches to the absence of tube-tube interactions. However, we do not assume to have tube-tube interactions in our samples, since we used tubes separated in solution.

In Fig. 4.3, the Raman susceptibility $|\chi_{11}^{\text{max}}|$ of metallic nanotubes appear to be weaker than the susceptibilities of semiconducting nanotubes excited into the second optical transition E_{22}^S . Similar to the intensity difference between the E_{11}^S and E_{22}^S transitions of semiconducting nanotubes, the origin of this difference is mainly due to differences in the broadening parameter γ of the underlying electronic transition rather than due to changes in the transition matrix elements (\mathcal{M}_R). In Fig 4.8 we show the broadening γ as a function of nanotube diameter³ for the E_{22}^S transition of semiconducting nanotubes (stars) and the E_{11}^M transition of metallic nanotubes (circles). In average the broadening parameter of metallic nanotubes is ≈ 1.5 times larger than that of semiconducting nanotubes excited via E_{22}^S . This change in γ leads to a decrease of $|\chi_R^{\text{max}}|$ by a factor of approximately two, which is the average difference between $|\chi_{22}^{\text{max}}|$ of semiconducting tubes $\nu = -1$ and $|\chi_R^{\text{max}}|_{11}$ of metallic nanotubes. In conclusion, there is no significant difference between the Raman matrix elements \mathcal{M}_R of metallic nanotubes, referring to the lower branches, and semiconducting nanotubes.

³($1/\omega_{\text{RBM}}$ is proportional to the diameter)

Figure 4.9: Diameter dependence of $|\chi_R^{max}|$ for semiconducting tubes excited into E_{22}^S ($|\chi_{22}^{max}|$). In order to compare our results to predictions on the Raman matrix elements \mathcal{M}_R $|\chi_{22}^{max}|$ has been corrected to the influence of the diameter dependence of γ (see Fig. 4.8 and ω_{RBM} , see text). The solid line is a linear fit to the data, thus represents the diameter dependence of the Raman matrix element \mathcal{M}_R .



4.1.5 Diameter Dependence of $|\chi_R^{max}|$

Next to the difference between metallic and semiconducting nanotubes figure 4.8 shows that there is a significant diameter dependence of the broadening parameter γ which is especially pronounced for metallic nanotubes. As mentioned above, γ is related to the carrier lifetime which was calculated in Ref. [87] for a large number of (n_1, n_2) . Considering solely the electron-phonon coupling of the particular nanotube they get a diameter dependence of γ similar to our results. However, for large diameter tubes there is an increasing deviation between our results [$\gamma(d = 1.5 \text{ nm}) = 60 \text{ meV}$] and results published in Ref. [87] [$\gamma(d = 1.5 \text{ nm}) = 30 \text{ meV}$]. The reason for this deviation could be the fact, that in real nanotubes, thus our experiments, the transitions are additionally broadened due to sample inhomogeneities.

In case of metallic nanotubes the deviations between our results and results published in Ref. [87] are even more apparent. Similar to experimental results by Doorn *et al.* [85], we observe much larger values of the broadening parameter γ . This deviation indicates the presence of decay channels, which were not considered in Ref. [87], e.g. the influence of the Kohn anomaly on the electron-phonon coupling in metallic nanotubes [25].

Regarding the Raman susceptibility we must consider the values to be affected by the dependence of the broadening parameter γ as a function of the tube diameter d . Furthermore we are interested how the Raman matrix element \mathcal{M}_R varies with d . Therefore we plot the $|\chi_R^{max}|$ where we eliminated effects due to the diameter dependence of γ . In order to compare our results to \mathcal{M}_R we furthermore have to correct $|\chi_R^{max}|$ to ω_{RBM} and the excitation energy $\hbar\omega_i$, see Eq. 2.4.

In the diameter range of the observed nanotubes this causes $|\chi_R^{max}|$ to appear 20% stronger for the largest diameter tubes compared to the smallest tubes. In Fig. 4.9 we show $|\chi_R^{max}|$ normalized to influences by γ and the phonon energy. Therefore, the solid

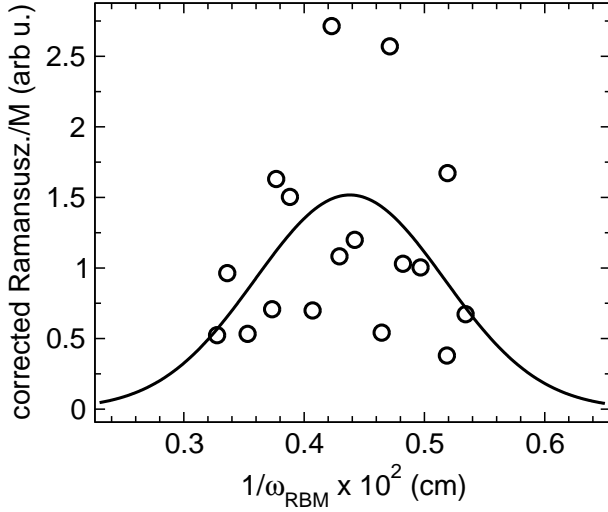


Figure 4.10: Raman susceptibility $|\chi_R^{max}|$ of semiconducting nanotubes excited into E_{22}^S normalized in order to represent the (n_1, n_2) abundance superimposed by the dependence of $|\chi_R^{max}|$ on the chiral angle θ (see text). The solid line shows the diameter distribution in the sample, assuming a Gaussian diameter distribution. The curve has a mean diameter of 1.0 nm and a full width at half maximum of 0.5 nm.

line gives the average dependence of the matrix element on the nanotube diameter. As mentioned above, the data in Fig. 4.9 are affected by the diameter distribution of the nanotubes. Assuming the diameter distribution to be symmetric, we expect effects of the distribution to cancel out.

Fig. 4.9 shows that the matrix elements decrease with increasing diameter. The same radial displacement results in a larger change of the carbon-carbon bonds in smaller tubes. A stronger change of the bonds corresponds to a larger electron-phonon coupling \mathcal{M}_{e-ph} . Therefore our result is in agreement with theory.

4.2 (n_1, n_2) abundances

In the previous section we assumed a uniform diameter distribution and attributed all differences in the Raman intensities to (n_1, n_2) specific variations of the scattering efficiency. Of course our sample does not contain all imaginable (n_1, n_2) . First we need to consider a diameter distribution, primarily determined in the growth process by the size of the catalyst particles [88].

In Fig. 4.10 we show $|\chi_R^{max}|$ of the semiconducting nanotubes excited into E_{22}^S as a function of nanotube diameter. In the presented data we eliminated diameter dependent variations of $|\chi_R^{max}|$ caused by γ and the phonon energy (see Sect. 4.1.5). Furthermore we normalized the data to the diameter dependence discussed in Sect. 4.1.5. Therefore we assume the intensities given in Fig. 4.10 to represent the diameter distribution and (n_1, n_2) abundances, respectively, superimposed by the dependence of \mathcal{M}_R on the chiral angle, discussed in Sect. 4.1.3.

To estimate the diameter distribution we fit the data by a Gaussian distribution and obtain a mean diameter of 1.0 nm and a full width at half maximum of 0.5 nm.

In addition to the diameter distribution we might assume that our sample has variations in the abundances of the different (n_1, n_2) tubes. To observe possible variations one can compare the experimentally obtained Raman intensities to theoretical predictions. The (n_1, n_2) abundance will then be given by the deviations between experiment and theory. Therefore a theory is needed which fully describes the scattering efficiency for each (n_1, n_2) . A comprehensive calculation of $|\chi_R^{max}|$, which includes electron-phonon, electron-hole, electron-electron, and exciton-exciton interactions has not yet been reported. Even if a potentially perfect theoretical description is achieved, one would not know if remaining deviations actually describe abundances or if there are further effects which are not included in the theory. A possible solution to this dilemma might be the additional study of the intensities observed in photoluminescence excitation experiments on the same sample [89].

4.3 Summary

In this chapter we presented the dependence of the Raman susceptibility $|\chi_R^{max}|$ of the radial breathing mode in carbon nanotubes on the optical transition (E_{11}^S and E_{22}^S), the nanotube family ν , the chiral angle θ , the metallicity (semiconducting or metallic) and the nanotube diameter d .

We found that $|\chi_R^{max}|$ in semiconducting nanotubes is much larger when the particular tube is excited into the first electronic transitions E_{11}^S compared to an excitation into E_{22}^S . Based on the lineshape of the resonance profiles we showed that this is mainly due to the much smaller broadening γ of E_{11}^S compared to E_{22}^S .

As well the dependence of $|\chi_R^{max}|$ on the family ν and the chiral angle θ we could associated to the position of the optical transition in the k -space with respect to the K point of the graphene Brillouin zone. Our results suggest that the electron-phonon coupling of the RBM is close to zero when the electronic transition of the particular nanotube is close to the K - K direction. This is the case for nanotubes with a chiral angle $\theta \approx 20^\circ$ and either $\nu = -1$ or $\nu = +1$ depending whether exciting into E_{11}^S or E_{22}^S , respectively.

Similar to the overall deviation of $|\chi_R^{max}|$ between E_{11}^S and E_{22}^S we found larger $|\chi_R^{max}|$ for semiconducting nanotubes compared to metallic nanotubes. Again we associated this to differences in the broadening parameter γ of the electronic transitions E_{ii} with larger γ in metallic nanotubes. Additionally we found γ to have a different diameter dependence in metallic and semiconducting tubes. The larger γ and the larger diameter dependence of γ in metallic nanotubes suggest an additional relaxation process in metallic nanotubes compared to semiconducting nanotubes.

Furthermore we found a diameter dependence of $|\chi_R^{max}|$ which is an agreement with the idea that the larger a nanotube gets the more the wall of the tube approaches a flat sheet of graphene which has no radial breathing mode. Therefore $|\chi_R^{max}|$ decreases gradually with increasing diameter.

In the last section of this chapter we discussed a possible study of (n_1, n_2) abundances in a nanotube sample based on the RBM intensities. Concerning the diameter distribution we found a mean diameter of 1.0 nm and a full width at half maximum of 0.5 nm in case of our particular HiPCO sample.

Chapter 5

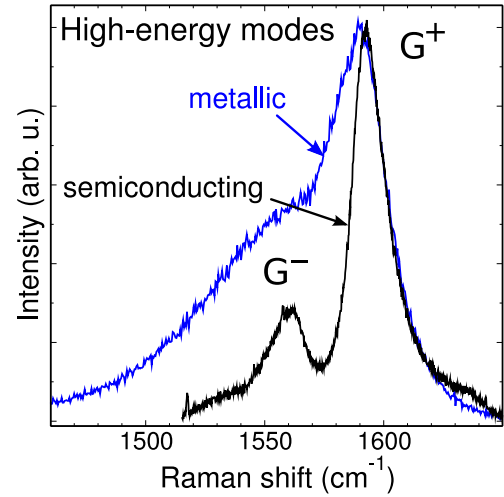
The high-energy modes

In the previous chapter (Chap. 4) we discussed the determination of the different (n_1, n_2) nanotubes in a sample on the basis of the radial breathing mode. In some growth, separation and selective functionalization methods, on the other hand, focus is solely put on the question whether a sample has more or less metallic or semiconducting nanotubes compared to another sample [6–8, 90]. The success of such a method can be monitored by studying the high-energy modes (HEM) rather than doing a full (n_1, n_2) analysis from the RBM [5, 20, 64].

Between 1540 and 1600 cm^{-1} , the Raman spectrum of a typical carbon nanotube sample – containing a large variety of chiral indices – shows two characteristic HEM features which are commonly referred to as G^- (lower frequency) and G^+ (higher frequency). Compared to the RBM, the high-energy modes are less diameter dependent and the resonance windows are up to an order of magnitude wider. Therefore, the HEM is often formed by overlapping signal of many different tubes. While both features appear as reasonably sharp peaks when mainly semiconducting nanotubes are resonantly excited (full width at half

maximum: FWHM $\sim 10 \text{ cm}^{-1}$), the G^- peak is broadened and downshifted when mainly metallic nanotubes are in resonance. [91] In the following we use the terms “metallic” G^- and “semiconducting” G^- , when referring to a broad and a narrow G^- peak, respectively.

In case of semiconducting nanotubes, G^+ and G^- are attributed to the LO and TO phonon, respectively, where LO refers to the axial (longitudinal optical) and TO to the circumferential (transverse optical) displacement of the atoms. [24, 92] For metallic nan-



otubes, the assignment of the G^- and G^+ Raman peaks to the TO and LO phonons is still under debate with contradicting conclusions appearing in the literature. [23–25, 29, 92–95]

Two different models have been developed for the description of the peculiar lineshape of the high-energy Raman modes (G^- and G^+) in metallic carbon nanotubes. The first model [23] proposed phonon-plasmon interactions as the origin of the metallic lineshape. According to this model, the linewidth increases with the thickness of the nanotube bundle. The G^- and G^+ features were assigned in Ref. [23] to the TO and LO phonon, respectively, as in semiconducting tubes. More recent models attribute the broadening of the “metallic” G^- to strong coupling between the LO phonon and electronic excitations. [24, 25, 93] This coupling causes a dramatic softening of the LO frequency and a broadening of the Raman line. As a result, the frequency of the LO phonon drops below the frequency of the TO phonon in metallic nanotubes. [24, 25, 93] This theory explains the “metallic” G^- and, in particular, the large Raman linewidth as an intrinsic property of a single metallic tube and is consistent with recent experiments on free-standing metallic nanotubes and on graphene. [94, 96] In this model – due to the strong electron-phonon coupling – the LO frequency is below the TO frequency, and consequently the G^- peak is assigned to the LO phonon. In some Raman measurements on what were presumed to be single metallic nanotubes, the G^+ peak has been reported at 1590 cm^{-1} . [26–28] Consequently this peak would have to be assigned to the TO phonon in metallic tubes. However, the TO phonon in metallic tubes is expected to have a similar frequency to that of the TO mode in semiconducting tubes, which is below 1590 cm^{-1} [24, 93]. The question therefore arises how to assign the G^+ peak at 1590 cm^{-1} .

In Section 5.1 we present results from resonant Raman experiments of the high-energy mode in isolated nanotubes separated in solution. By comparison of the Raman intensities of the different features of the HEM to the intensities of the RBM we assign the HEM-features to particular nanotubes or groups of tubes. Subsequent comparison to theoretical data allows us to assign most of the peaks to the particular phonons involved in the Raman process [95]. In this way we show that the characteristic broadened and downshifted G^- peak, which appears when metallic nanotubes are in resonance, is an intrinsic feature of metallic nanotubes, although it is weaker than in bundled tubes. Based on comparison to theoretical predictions we assign the broad and downshifted G^- peak to the LO-phonon in metallic nanotubes.

In addition to the major features, mentioned above, we observe a series of small peaks on the low and on the high-energy side of the HEM. Considering the RBM intensities we can assign the minor peaks on the low-energy side to the TO-phonons of particular semiconducting nanotubes or groups of tubes. Therefore we present the first experimental data of TO-phonon frequencies below 1.3 nm . For the peaks of the high-energy side of

the HEM we give a tentative assignment. We propose a second-order scattering process involving the infrared-active phonon as the origin of these peaks.

In the second section of this chapter (Sect. 5.2), we study a tiny bundle of one metallic and one semiconducting nanotube with Rayleigh scattering and resonant Raman scattering experiments. We show that the presence of a G^+ peak at $\sim 1590 \text{ cm}^{-1}$ in a typical “metallic” Raman spectrum, with a broad G^- and a narrow G^+ , often indicates the presence of an additional semiconducting nanotube. By varying the excitation energy we observed a changing lineshape for the high-energy G^+ and G^- Raman modes. We see a broad “metallic” G^- peak at 1540 cm^{-1} and a narrow G^+ peak at 1590 cm^{-1} with maximum Raman intensities at different excitation energies. Considering results from Rayleigh scattering experiments and radial breathing mode Raman spectra, we can relate the peak at 1540 cm^{-1} to the longitudinal mode of the metallic tube which is broadened due to the strong electron-phonon coupling, while the peak at 1590 cm^{-1} originates from the semiconducting tube [97].

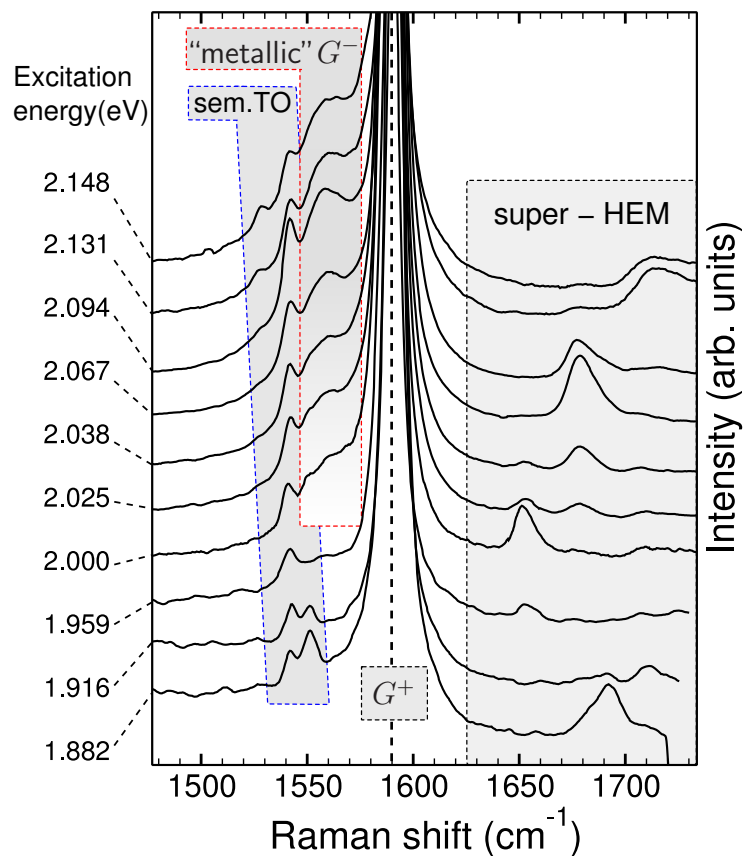
5.1 Nanotubes in solution

Parts of this sections were published in Ref. [95]

Data presented in this section are obtained from single-walled carbon nanotubes produced by the HiPCO method [98]. Therefore the observed nanotubes have diameters between ≈ 0.5 and ≈ 1.5 nm and include all chiral indices (n_1, n_2) contained in this diameter range (Sect. 4.2). The tubes were ultrasonically dispersed in D_2O and stabilized in surfactant micelles using sodium dodecyl sulfate (SDS) and sodium dodecylbenzene sulfonate (SDBS). [73, 99] Raman measurements were performed in backscattering geometry at room temperature on a macro-Raman setup as described in Sect. 2.2. We varied the excitation energy between 1.88 and 2.15 eV using a tunable dye laser. Spectra were normalized to laser power and integration time and were corrected for the system response (see Sect. 2.1.2).

Figure 5.1 shows the high-energy Raman spectra excited with different laser lines. The spectra show the characteristic features of the high-energy mode (HEM), a relatively sharp peak at 1590 cm^{-1} (G^+) and a broader peak at $\approx 1560\text{ cm}^{-1}$ (“metallic” G^-) with a full width at half maximum of 9 cm^{-1} and 30 cm^{-1} , respectively. The main peak (G^+) is

Figure 5.1: Raman spectra of the high-energy modes from a carbon nanotube ensemble excited at different laser energies. The spectra are vertically offset for clarity. Spectra are truncated in order to enhance variation of the less intense peaks. The characteristic features, a sharp peak at 1590 cm^{-1} (G^+) and the broad “metallic” G^- peak at $\approx 1560\text{ cm}^{-1}$ are seen (Sect. 5.1.1). Additionally we observe a series of small peaks on the low and high-energy side of the HEM (sem. TO) and a group of peaks on the high-energy side (super-HEM) which will be discussed in Sect. 5.1.2 and Sect. 5.1.3, respectively.



observed at all excitation energies (E_{laser}), while the smaller, broad peak (“metallic” G^-) is not visible at lower E_{laser} . It becomes apparent only for excitation energies above 2 eV. In addition, several peaks are seen below the “metallic” G^- and above the G^+ peak, with strongly varying resonance conditions.

In the following we will correlate the different features of the HEM to the transition energies E_{ii} of the different (n_1, n_2) nanotubes. As the transition energies are obtained from resonance profiles of the RBM our approach is solely based on experimental data, thus independent of theoretical prediction. Based on an experimental Kataura plot, the observed RBM frequencies can be uniquely identified with a particular chiral index (n_1, n_2) , as described in Sect. 3.5 [5]. Given this assignment, we analyze the HEM features on the basis of their strength in the Raman spectrum. This procedure is justified as long as the electron-phonon coupling matrix elements are similar for the RBM and the HEM. Indeed, the diameter and family dependence of RBM and HEM are similar, as was shown in recent *ab-initio* calculations [50, 100].

Note, that the terms G^- and G^+ evolved on the basis of a rather simple picture of the high-energy modes, in which all nanotubes contribute to both features. In this chapter we will show that the HEM is a multi-peak feature in the Raman spectrum from a nanotube ensemble, and that different nanotubes contribute to the different peaks. Therefore the terms G^- and G^+ can be rather confusing. As this problem occurs most particularly in case of G^- , we will always distinguish between “metallic” and “semiconducting” G^- .

5.1.1 The LO phonon modes

In Fig. 5.2(a) and Fig. 5.2(b) we show on the left contour plots of the RBM intensity as a function of excitation energy and the inverse RBM frequency, thus the nanotube diameter (see Sect. 3.3.1). The contour plots show the resonances of numerous RBMs which we assigned to the particular (n_1, n_2) (see Sect. 3.5). In the contour plot of Fig. 5.2(a) we labeled some of the assigned peaks by their chiral indices (n_1, n_2) . Apparently semiconducting tubes are well separated from metallic nanotubes. Therefore we plot a line, which separates the second optical transition E_{22}^S of semiconducting nanotubes from the first transition E_{11}^M of metallic tubes.

On the right of Fig. 5.2(a) and (b) we plot the intensities of the G^+ and the “metallic” G^- peak as a function of excitation energy. In order to correlate the HEM intensities to the RBM intensities we used the same energy scaling for both the contour plot on the left and the intensity plot on the right. The intensity of “metallic” G^- peak in Fig. 5.2(b) clearly goes through a maximum at 2.05 eV. This energy matches the transition energies of a number of RBMs highlighted by an ellipse in the contour plot. All RBMs inside the ellipse originate from metallic nanotubes from the (13,1) branch. Therefore, we

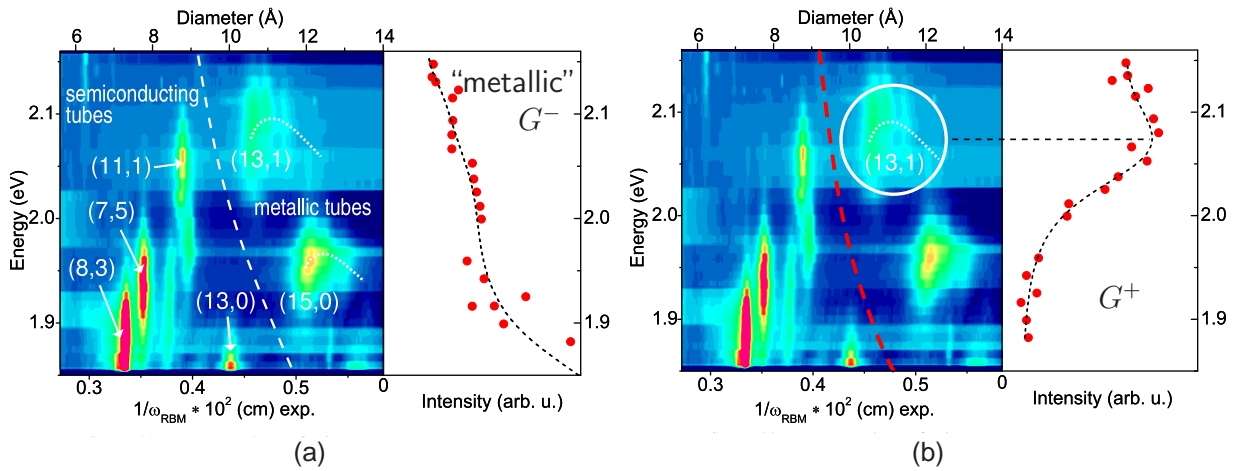


Figure 5.2: [(a) and (b) left] Colored contour plot of the Raman cross section of the RBM as a function of excitation energy and reciprocal RBM frequency (taken from Ref. [20]). The top axes gives the tube diameter according to $\omega_{\text{RBM}} = c_1/d + c_2$ (Sect. 3.3.1). Dashed lines separates the E_{11}^{M} optical transitions of metallic from the E_{22}^{S} transitions of semiconducting tubes. Dotted lines connect tubes of the same branch. [(a) and (b) right] Raman cross section of the G^+ peak (a) and G^- peak (b) vs. excitation energy (with the same scaling as the energy axes in the contour plot). Dashed line on the G^+ intensities is a guide to the eye (spline). G^- intensities are fit by a resonance profile. (b) The ellipse emphasizes the (13,1) branch assigned to G^- . The apparent weak intensity of the (13,1) branch compared to that of the (15,0) branch is an artifact due to different samples, which changed at ≈ 2 eV [5].

assign the “metallic” G^- peak to the (13,1) branch of metallic tubes [(13,1), (12,3), (11,5), (10,7) and (9,9)].

In contrast, the intensity of the G^+ peak in Fig. 5.2 (a) decreases with increasing excitation energy [right of Fig. 5.2 (a)]. The contour plot shows that the number and intensity of RBMs from semiconducting tubes decreases with increasing laser energy. The resonance maximum of G^+ is apparently below 1.85 eV. Therefore, we assign G^+ to semiconducting nanotubes.

In Fig. 5.3 we show HEM spectra with (red line) and without (black line) metallic tubes in resonance. Nanotubes produced by the HiPCO method do not contain metallic tubes with optical transition energies below 1.8 eV. [20] Therefore we used an excitation energy of 1.69 eV to obtain Raman spectra exclusively from semiconducting nanotubes (black line). In order to also match transition energies of metallic tubes we used a laser energy of 2.12 eV (red line). As mentioned in the introduction to this chapter the broad and downshifted “metallic” G^- peak is enhanced in bundled nanotubes, as can be seen in Fig. 5.3 (b). However, figure 5.3 (a) shows that also in case of separated tubes spectra with and without metallic nanotubes in resonance can well be distinguished by the intensity of the broad and downshifted G^- . Therefore we show that also for isolated nanotubes the

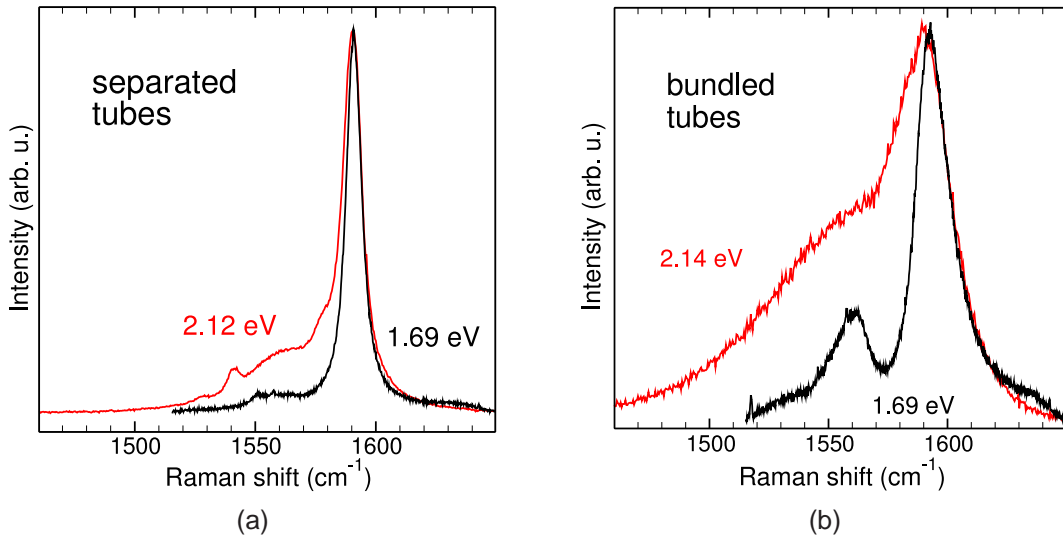


Figure 5.3: HEM with (red) and without (black) metallic tubes in resonance. (a) Separated HiPCO tubes in solution. (b) bundled HiPCO tubes.

lineshape of the HEM is suitable to detect metallic nanotubes and that the broadened and downshifted G^- is an intrinsic feature of metallic nanotubes.

The observation of the downshifted and broadened G^- peak in separated metallic nanotubes excludes the phonon-plasmon coupling as the origin of the “metallic” lineshape, since this theory is based on the formation of plasmon bands in bundled nanotubes [23]. However, the enhanced peak intensity of the G^- peak due to bundling is apparent in Fig. 5.3. Although the phonon-plasmon coupling is not the origin of the shift and broadening of the “metallic” G^- peak, it still might cause the intensity increase in bundled nanotube, see discussion below.

In the following we want to compare our results to theories which give a strong electron-phonon coupling (Kohn anomaly) as the reason for the “metallic” lineshape [24,93]. Therefore we plot in Fig. 5.4 the predicted Γ point phonon frequencies of the LO and TO phonons of metallic and semiconducting nanotubes as a function of tube diameter. Figure 5.4 (a) shows the Γ point LO phonon frequencies of semiconducting tubes obtained from theory (black solid line and black circle) and experiment (black stars) [24, 93, 101]. The red solid line and open circles are theoretical predictions for the LO phonon frequencies of metallic nanotubes. Positions from our measurements for the G^+ and “metallic” G^- peaks are given by dashed lines. The position of G^+ is in good agreement with the nearly diameter independent frequencies of the LO phonon in semiconducting nanotubes. The position of the “metallic” G^- peak matches the softened LO phonon frequencies of large diameter metallic tubes. However, the predicted frequencies of the tubes we assigned the “metallic” G^- to – the tubes from the (13,1) branch, which have diameters between the

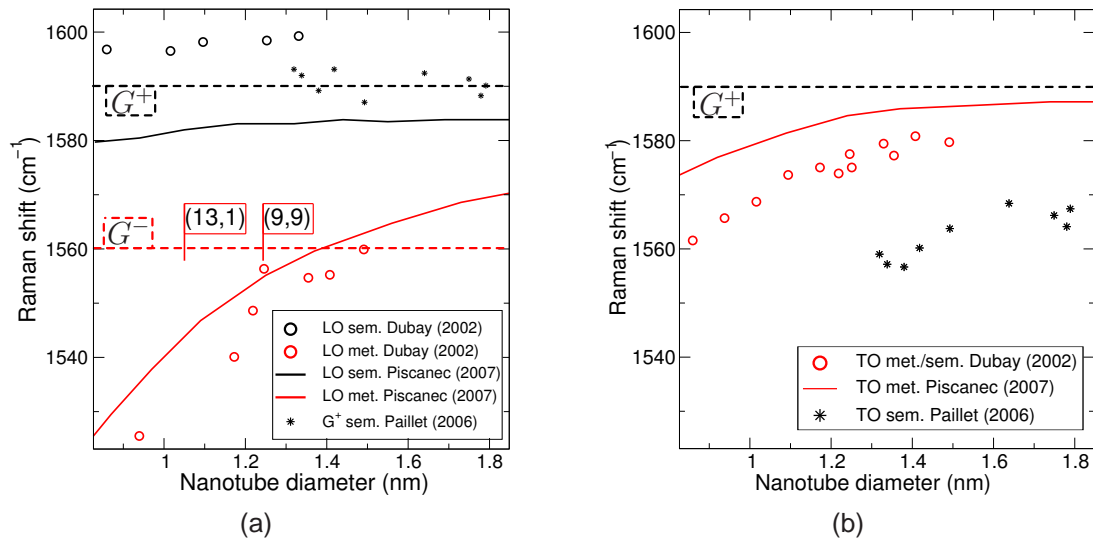


Figure 5.4: Frequencies of (a) the LO phonons in metallic and semiconducting nanotubes and (b) the TO phonons in metallic nanotubes as a function of tube diameter. Horizontal dashed lines give the observed positions of G^+ and “metallic” G^- . The diameter range of the tubes assigned to the “metallic” G^- peak is marked by the largest [(13,1)] and smallest [(9,9)] tube of the (13,1) branch.

(13,1) ($d = 1.06$ nm) and (9,9) ($d = 1.22$ nm) tubes – are slightly lower than our results. The reason for this might be doping of the tubes by the surfactant. Doping weakens the electron-phonon coupling, caused by the Kohn anomaly. Therefore the LO phonon in metallic nanotubes is less softened in the surfactant-wrapped tubes compared to the pristine tubes assumed in the theory.

In summary, our results support the theory of a Kohn anomaly at the Γ point in the phonon dispersion of the LO phonon, which causes a strong electron-phonon coupling of phonons to electrons close to the Fermi level [24, 25].

Having assigned “metallic” G^- to the LO phonon in metallic nanotubes the question arises, whether the metallic tubes also contribute to G^+ or whether this peak originates exclusively from semiconducting nanotubes. In the first case, the TO phonon of metallic nanotubes would have to be at the same position as the LO phonon of semiconducting nanotubes, namely at 1590 cm^{-1} . Figure 5.4(b) shows that predictions of the TO frequencies in metallic nanotubes deviate between data from Dubay *et al.* [24] and Piscanec *et al.* [93]. Dubay *et al.* predict the TO frequencies to be distinctly below 1590 cm^{-1} , i.e. the G^+ peak would be related to the LO phonon in semiconducting tubes. In contrast Piscanec *et al.* predict a TO frequency in metallic tubes similar to the frequency of the LO phonon in semiconducting tubes. We can therefore not tell from the experiments presented in this section whether in addition to the semiconducting tubes metallic nanotubes contribute to the G^+ peak. This point will be discussed in more detail in Sect. 5.2 on the

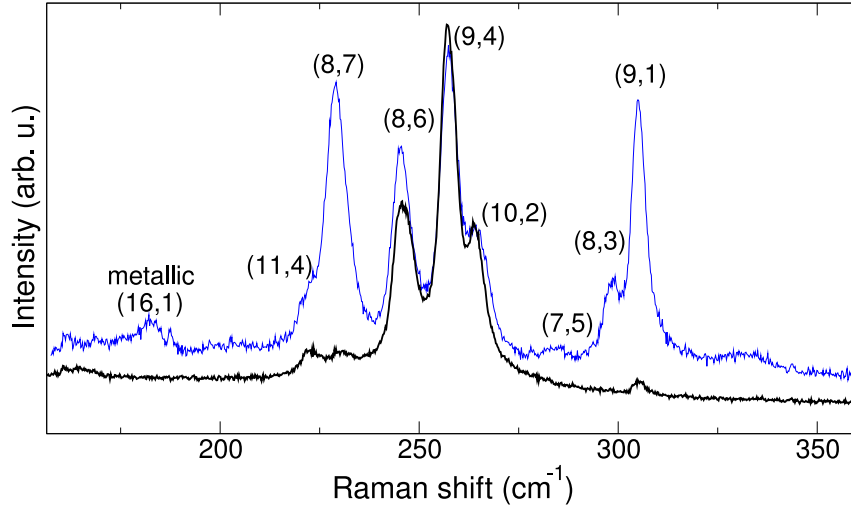


Figure 5.5: RBM spectra from bundled (blue) and separated (black) nanotubes taken at ≈ 1.7 eV. Due to wider resonance windows more tubes are in resonance and more RBMs appear at a given excitation energy in bundled tubes compared to separated tubes.

basis of the HEM from a single metallic nanotube.

Despite the fact that our results support the theory of a Kohn anomaly as the origin of the broadened and downshifted G^- in metallic nanotubes, the lineshape of the HEM is effected additionally by bundling, see Fig. 5.3. Figure 5.3 shows spectra with (red) and without (black) metallic tubes in resonance. Compared to the spectra of separated tubes in (a), the spectra of bundled tubes in (b) show much broader peaks and an increase of the G^- intensity relative to the G^+ intensity.

Before we start interpreting this finding we want to point out that the two samples – bundled and separated tubes – can be compared only to a limited extend. Although both samples are identical in terms of the growth process, the separated tubes were substantially treated in order to separate the tubes and to stabilize them in solution. We can expect that dirt, like amorphous carbon, is removed during these treatments. Since most carbon related materials give Raman signal at energies similar to that of the HEM in nanotubes, the broadening of the HEM peaks in the bundled sample might solely be related to impurities in the sample. In the following discussion we assume all observations to be based solely on the bundling of the tubes, while there is no effect induced by impurities.

Assuming that the broadening of the peaks in the HEM spectrum of bundled tubes in comparison to the separated tubes (Fig. 5.3) is related to plasmon-phonon interactions, as proposed by Kempa *et al.* [23], it is very surprising to see a broadening of the peaks in bundled tubes when only semiconducting tubes are in resonance. Semiconducting tubes have by definition no electrons close to the Fermi level and therefore can not generate plasmons.

Another interpretation which could explain also a broadening of the semiconducting HEM features is the diameter dependence of the frequencies of the HEM phonons. It is known that the resonance window of bundled nanotubes is by up to 50 meV larger than

in separated tubes [72]. Therefore in bundled tubes more nanotubes are in resonance at a particular excitation energy. This is nicely seen in the low energy part of the nanotube Raman spectrum. Figure 5.5 shows the RBM spectra of separated nanotubes in solution (black) and of bundled nanotubes (blue), both excited at 1.69 eV. The larger number of RBMs from the bundled nanotubes is solely the result of larger resonance windows in nanotube bundles. Therefore also the HEM is the superposition of a larger number of nanotubes (n_1, n_2) when nanotubes are bundled compared to separated nanotube in solution. Figure 5.4(a) shows that the frequencies of all HEM phonons depend on the nanotube diameter. As there are more nanotubes in resonance in case of the bundled tubes the diameter dependence might lead to a broadening of the peaks. However, by simply superpositioning all HEM spectra taken at the different excitation energies, and therefore covering the whole diameter range in our sample, we do not see a broadening which is comparable to that seen in bundled tubes. To solve this issue, further experimental studies are needed in which separated tubes are rebundled. Unlike in our sample the separated tubes should not be stabilized by the use of solvents, since the solvent remains around the tube and prevents the tubes from rebundling.

5.1.2 The TO phonon modes

In the previous section we assigned the major features of the observed HEM, G^+ and “metallic” G^- , to LO phonons in semiconducting and metallic nanotubes. For semiconducting nanotubes we expect to see the modes of the TO phonons on the low energy side of the LO phonon mode [24, 92]. In fact, we observe three small peaks at 1526 cm^{-1} , 1541 cm^{-1} , and 1551 cm^{-1} (Fig. 5.1). Since each of these peaks is in resonance at different resonance condition, we can perform an (n_1, n_2) assignment in the same way as we did for the major peaks in the last section.

In figure 5.6 we compare the excitation energy dependence of the peak intensities of the three small peaks to the intensities of RBMs. Obviously the resonances of the peaks match the resonance of a large variety of RBMs. However, due to the diameter dependence of the TO, see below, and the different diameters of metallic and semiconducting nanotubes in our excitation regime, we will show now that these peaks originate from semiconducting nanotubes.

The intensity profile of the peak at 1541 cm^{-1} [Fig. 5.6(b)] covers almost the whole resonance profile including incoming and outgoing resonance. Fitting equation 2.5 – the equation for a resonance profile – to the intensity profile yields the transition energy E_{ii} (dashed, black line) of the corresponding nanotube (n_1, n_2) . The comparison to the RBMs on the left of Fig. 5.6 shows that this energy matches nicely the transition energy of the (7,5) nanotube. However, there are nanotubes with similar resonance energies as the

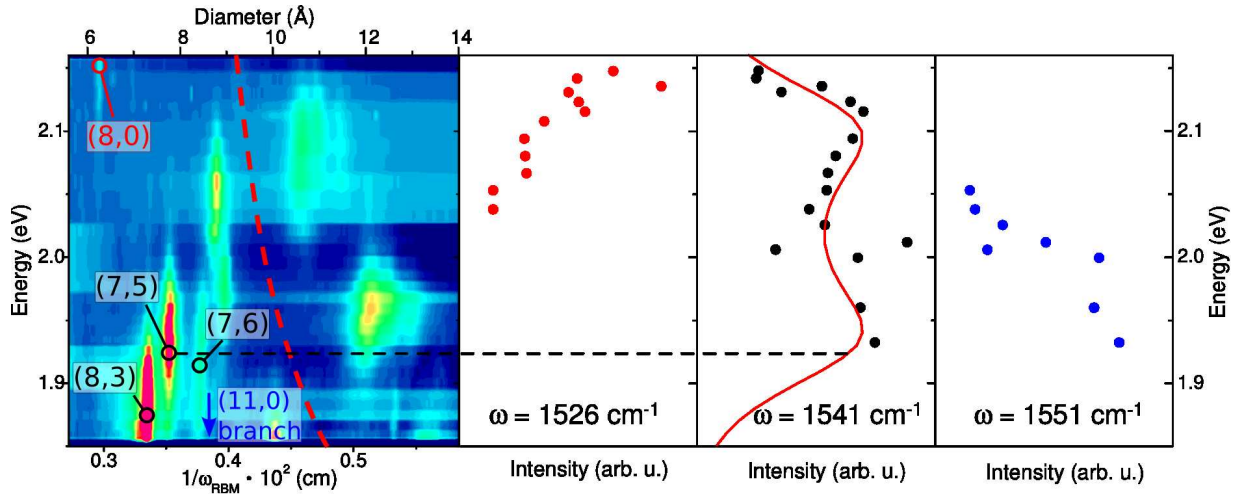


Figure 5.6: (left) Contour plot of the RBM intensities as a function of excitation energy and tube diameter. (right) intensities of the three observed modes which we assigned to TO phonons in semiconducting nanotubes. To the intensities of the peak at 1541 cm^{-1} we fit a resonance profile which yields the transition energy given by the dashed, black line.

(7,5) tube, mainly the (7,6) with a slightly larger diameter and the (8,3) with a slightly smaller diameter. As discussed above we can assume that the HEMs show similar intensity behavior as the RBMs regarding the dependence on the nanotube family $\nu = \pm 1$ [50,100]. Therefore we expect the TO phonon mode of the (7,6) tube ($\nu = +1$) to be weaker than the TO mode from the (7,5) nanotube ($\nu = -1$). The (8,3) nanotube also belongs to the $\nu = -1$ family and shows an RBM with a similar intensity as the (7,5), therefore the (8,3) should as well give rise to a TO mode. In fact, the observed peak position shifts with the excitation energy. Therefore the peak at 1541 cm^{-1} is most probably a superposition of the TO phonon modes of the (8,3) and the (7,5) nanotube.

In case of the peaks at 1551 and 1526 cm^{-1} , the observed excitation energy range does not cover the whole resonances of the peaks. Therefore we can not determine the exact transition energies of the corresponding nanotubes. However, the peak at 1526 cm^{-1} comes into resonance when the RBM of the (8,0) tube comes into resonance. The TO phonon in zig-zag tubes, thus the (8,0) tube, is forbidden by symmetry [48]. Therefore we do not assign the peak at 1526 cm^{-1} to the (8,0) nanotube but to the nanotubes of the same branch, (7,2) and (6,4), which have slightly larger diameters. Because they also have larger transition energies than the (8,0) their RBM signal becomes strong outside the observed energy range and we do not see them in the contour plot of Fig. 5.6. From the peak at 1551 cm^{-1} we only observe the high-energy tail of the outgoing resonance, which makes it even harder to assign it to a particular tube. Tentatively we assign this peak to the tubes from the next $\nu = -1$ branch below the (9,1) branch, which is the (11,0) branch including the (10,2), (9,4), and (8,6) tubes. We exclude the (11,0) tube of this branch as a possible candidate, because it is a zig-zag tube again.

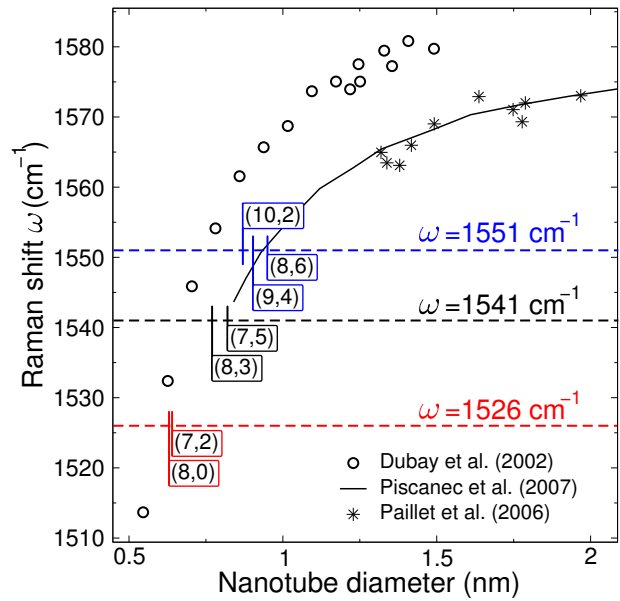


Figure 5.7: Frequencies of the TO phonons in semiconducting nanotubes. Horizontal dashed lines give the position of the observed peaks. Diameters of the tubes which we assigned to the particular peaks are marked. Our results are in excellent agreement with the predictions from Ref. [93].

In Fig. 5.7 we compare our results of the assigned TO phonon modes to theoretical predictions by Dubay *et al.* [24] (circles) and Piscanec *et al.* [93] (black solid line) and to previous results from individual semiconducting nanotubes by Paillet *et al.* [102] (stars). The plot shows the TO phonon frequencies as a function of tube diameter. The positions of the peaks from our measurements are given by the horizontal dashed lines. In addition we give the diameters of the nanotubes which we assigned to the particular peaks. Our results nicely match the predictions by Piscanec *et al.* [93] and extend the range of experimentally assigned TO phonon modes to much smaller tube diameters. This result on the one hand supports our assignment of the peaks at 1551, 1541, and 1526 cm^{-1} to the TO phonons in semiconducting nanotubes. On the other hand it suggests that regarding the TO phonons of semiconducting tubes the predictions from Ref. [93] are in better agreement with experimental results from HiPCO tubes in solution than the predictions from Ref. [24].

Having assigned the three small peaks to the TO phonons of semiconducting nanotubes the questions arises, at which frequencies are the TO phonons of the metallic nanotubes. Assuming that the position of the TOs in metallic nanotubes are at the same frequencies as in semiconducting nanotubes of same diameters, as predicted by Dubay *et al.* [24], we would expect the TOs of the metallic nanotubes to be between ≈ 1560 and $\approx 1565 \text{ cm}^{-1}$. One reason for the absence of the metallic TOs might be, that the intensity is too weak compared to the strong LO of metallic tubes in the same frequency range. This is conceivable, assuming the relative intensities of the TO phonon modes to be similar to that of the RBMs, which are weak for metallic nanotubes. On the other hand, Piscanec *et al.* [93] predicts the frequency of the TOs in metallic nanotubes to be very different to those of semiconducting nanotubes [93]. They predict a frequency which is rather comparable to that of the LO phonons in semiconducting nanotubes. In fact, till now no systematic experimental work has been published regarding the diameter dependence of the TO phonon modes in metallic nanotubes. Further discussions about the TO phonons in individual metallic nanotubes can be found in section 5.2.

5.1.3 Infrared active phonon

In this section we want to discuss the origin of the remaining peaks in Fig. 5.1 which are located between ≈ 1650 and ≈ 1720 cm^{-1} . Because these peaks have larger wavenumbers than the main features of the high-energy modes we will refer to them as super-HEM (sHEM). The fact that these peaks are rather asymmetric and that their resonances profiles are unusually narrow supports the assumption that these peaks are not the origin of a simple first order Raman process. A combination mode of the HEM and the RBM can be excluded, since this would lead to frequencies about 100 cm^{-1} higher than the frequencies observed. A feasible process would be the second-order overtone of the infrared-active mode with a expected frequency of ≈ 850 cm^{-1} .

In figure 5.8 (a) we plot the intensity of four super-HEMs versus the RBM intensities as described in the previous sections. The following assignment of the peaks is based on results from a tiny bundle of one metallic and one semiconducting nanotube, presented in the next section (Sect.5.2). There we show that a peak at 1677 cm^{-1} originates from the metallic (12,3) tube [(13,1) branch]. Therefore we also assign the peak at 1677 cm^{-1} which we observed in the measurements presented here to the (12,3) or at least to one of the nanotubes in the (13,1) branch. Assuming the origin of the super-HEMs to be the second-order overtone of the infrared-active mode, we would expect the frequency to

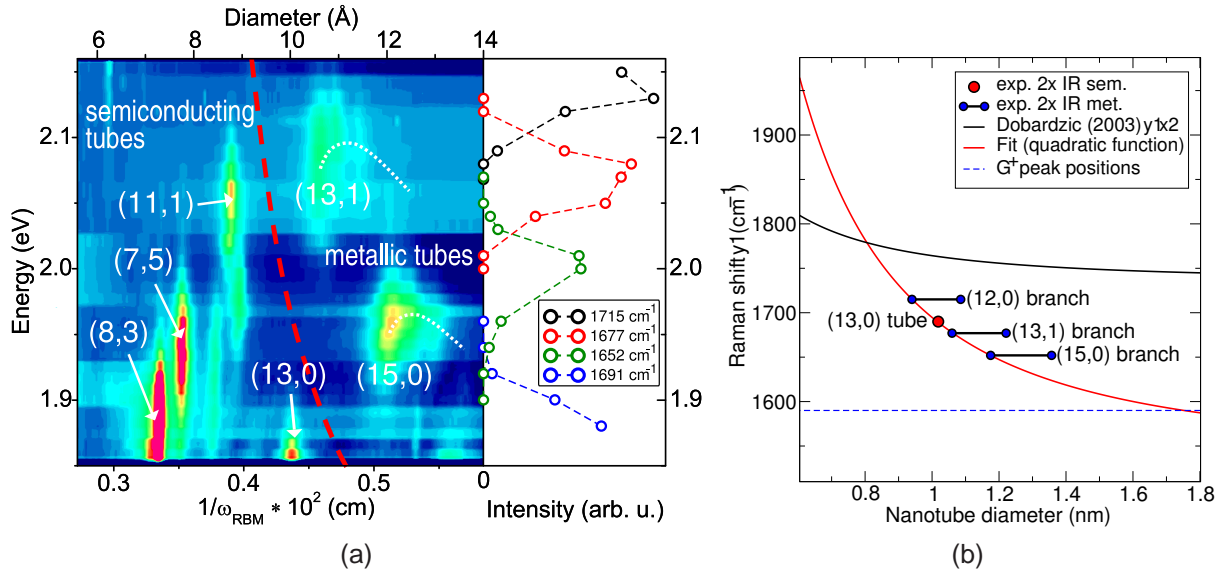


Figure 5.8: (a) (left) Contour plot of the RBM intensities as a function of excitation energy and tube diameter. (right) intensity of the observed super-HEMs as a function of excitation energy. (b) Raman shift of the sHEMs as a function of the diameter of the assigned tube(s). When we assigned the peak to more than one tube, a diameter range is given. The red line is Eqn. 5.1 fit to our results. The black line is two times the predicted frequency of the IR-mode as a function of diameter [56].

increase for larger diameter tubes [56]. We therefore have to look for smaller diameter tubes to assign the 1651 cm^{-1} peak to. The tubes with resonances matching the best are tubes from the (15,0) branch. Based on likewise considerations we assign the peaks at 1715 and 1690 cm^{-1} to tubes of the (12,0) branch and the (13,1) tube, respectively. Although we assigned in some cases the whole branch to one peak, it is probable that the particular peak originates from the small-chiral angle tubes within this branch, because the IR-mode in armchair tubes is forbidden by symmetry [56].

Figure 5.8 (b) shows the peak positions as a function of the diameter of the assigned nanotubes. In addition we plot two times the frequency of the IR-active phonon frequency (black line) predicted by Dobardžić *et al.* in Ref. [56]. Apparently, there is a strong deviation between the predicted data and our results. However, our data can nicely be fit by

$$\omega_{sHEM} = \frac{c_1}{d^2} + c_2 \quad , \quad (5.1)$$

the relation proposed in Ref. [56]. The additional third order term given in Ref. [56] is negligible in the diameter regime of interest here. Assuming the diameter dependence of the peak position given by the red line in Fig. 5.8 (b) to be correct, we have an easy explanation why we do not observe peaks from all the other tubes in resonance. Due to the small diameter their IR-mode is at much larger frequencies and therefore outside of the observed spectral range.

Our assignment of the sHEM peaks to the second order IR-phonon could further be supported if we found a mode with a similar diameter dependence as the super-HEM but

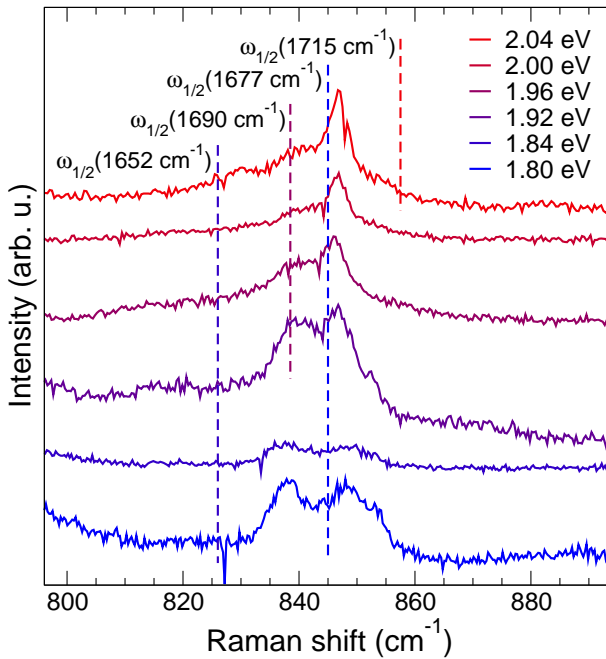


Figure 5.9: Nanotube Raman spectra as a function of excitation energy. In contrast to all other spectra presented in this chapter, these spectra were obtained from bundled nanotubes (HiPCO bucky paper) instead of isolated tubes in solution. The displayed spectral range covers the part of the spectrum where the IR-mode is expected. Dashed lines mark half the frequency of the super-HEMs of Fig. 5.1. The color of the lines give the estimated transition energy of the nanotube related to the particular sHEM. The scaling of the color of the dashed lines is the same as the color of the spectra.

with half the frequency. Of course, the first order IR-mode is not Raman active, however, it might be observed if there are enough defects present in the sample. Figure 5.9 shows the region of the Raman spectrum which covers $\omega_{1/2}$ of the sHEMs.¹ In Fig. 5.9 we marked the expected positions of the first order Raman modes $\omega_{1/2}$ by dashed lines. The color of the particular line marks the guessed resonance energy, assuming E_{ii} to be downshifted by ≈ 100 meV. Although, no unambiguous assignment is possible, the observed peaks seem to have a similar diameter dependence.

Further studies are necessary to clarify the origin of the super-HEMs. Therefore we will perform measurements including larger Raman shifts in order to study the sHEMs of smaller diameter tubes. On the same sample we will study the region of the Raman spectrum covering $\omega_{1/2}$ and determine the tube diameter dependence of the observed modes.

¹The spectra were taken from another kind of sample which also contained HiPCO nanotubes but in the form of bucky paper. Therefore we have to take tube-tube interactions into account. On the one hand this is a lowering of the transition energies E_{ii} in the tubes [73]. On the other hand the frequency of the IR-mode might be effected.

5.2 Isolated nanotubes

Parts of this sections were published in Ref. [97] and [103].

One of the biggest questions which was left open in the previous Section is, do the metallic nanotubes contribute to the G^+ peak of the high-energy modes. This question could not be answered since for nanotube ensembles there are energies where only semiconducting nanotubes are in resonance, but no energy where solely metallic nanotubes are in resonance. Therefore there is no way to obtain from such sample a HEM spectrum which shows signal exclusively from metallic tubes. To know the exact lineshape of a metallic nanotube is of interest for measurements on individual nanotubes. Knowing the expected lineshape would help to distinguish individual nanotubes from small bundles. To address this question we performed measurements on a tiny bundle of one metallic and one semiconducting nanotube, as shown in Fig. 5.10. With this kind of measurements we can furthermore confirm and strengthen the conclusion from the previous section regarding the LO phonon in metallic nanotubes as the origin of the downshifted and broadened G^- peak.

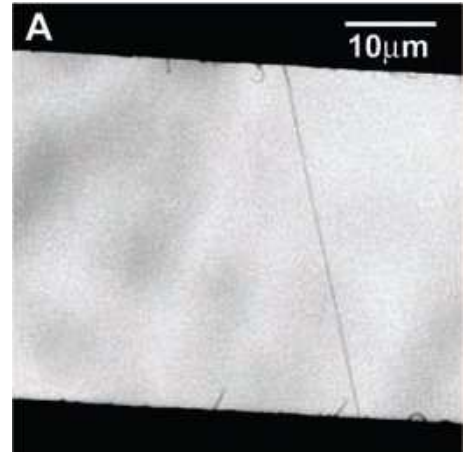


Figure 5.10: Single nanotube or small bundle across trench; similar to the sample used in this work. Taken from Ref. [104].

Rayleigh and resonant Raman scattering experiments were performed on a pair of one metallic and one semiconducting nanotube a side-product of single-nanotube growth. The nanotubes were grown in a CVD process using CoMo-doped mesoporous silica catalyst particles. To minimize possible interactions with the environment [30] tubes were grown across a $100\text{ }\mu\text{m}$ wide slit with the growth direction defined by the gas flow in the furnace [105]. A further advantage of freely suspended tubes, compared to tubes on substrate, is that there is no background signal generated from the substrate.

5.2.1 Rayleigh experiments

Rayleigh experiments presented in this section were performed by Yang Wu at the Columbia University New York.

Rayleigh scattering, elastic scattering of light, is as well as Raman scattering enhanced when the scattered light matches an optical transition in the sample. Therefore when the sample is irradiated by with-light each optical transition in the sample results in a peak in the spectrum of scattered light. Rayleigh scattering experiments are very useful for samples which are much smaller than the focus of the incoming light. On this kind of samples absorption spectroscopy would be impossible.

Rayleigh scattering measurements were performed using a white-light source and detected in a dark field geometry as described in Ref [104]. The detection range was between 1.24 and 2.76 eV. The tubes were located by scanning the white light focus along the slit until a bright scattering spot was seen, indicating the presence of freely suspended tubes.

In Fig. 5.11 we plot the Rayleigh spectrum of our nanotube sample. The spectrum shows three peaks at 1.937, 2.055 and 2.206 eV indicating either a bundle of three tubes, a bundle of two tubes from which one tube contributes with two transitions or one tube with three transitions. Considering a tube diameter between 1 nm and 2.5 nm, there is no single nanotube with three transitions predicted in the detection range of our system. Therefore our sample must consists of a small bundle of two or more nanotubes. Assuming two nanotubes in the sample there is a good chance of having one metallic nanotube since metallic nanotubes show pairs of closed by transitions. We will show below by resonant Raman experiments that it is indeed a pair of nanotubes, one semiconducting and one metallic.

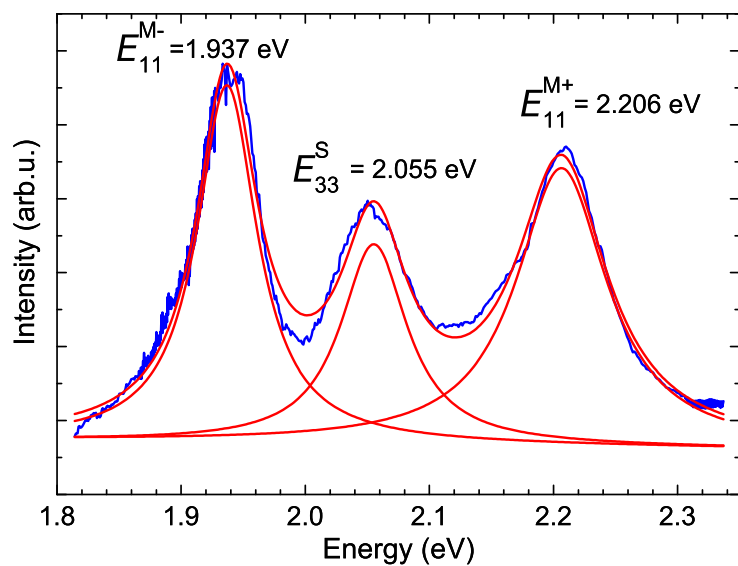


Figure 5.11: Rayleigh scattering spectrum of a pair of nanotubes. Peaks at 1.937 and 2.206 eV are assigned to the lower E_{11}^{M-} and upper E_{11}^{M+} transition of the first optical transition in the metallic (12,3) tube. The peak at 2.055 eV originates from the third optical transition E_{33}^S in a semiconducting tube.

5.2.2 Raman experiments

Raman measurements were performed on a micro-Raman setup as described in Sect. 2.2 in backscattering geometry at room temperature. The Raman excitation energy was varied between 1.87 and 2.15 eV using a tunable dye laser. To prevent laser induced heating, we limited the laser power to $\approx 200 \mu W$. [106,107]. Similar to the Rayleigh experiments we located the tubes by scanning the laser focus along the slit until a bright spot indicated the presence of a nanotube. All spectra were normalized to laser power and integration time. In order to correct the Raman intensities for the system response, we normalized each spectrum to the intensity of the Raman signal of CaF_2 (Sect. 2.1.2).

Figure 5.12 (a) shows the HEM Raman spectra for all excitation energies. The spectra show two peaks, a broad peak (metallic G^-) at 1540 cm^{-1} (FWHM= 48.5 cm^{-1}) and a

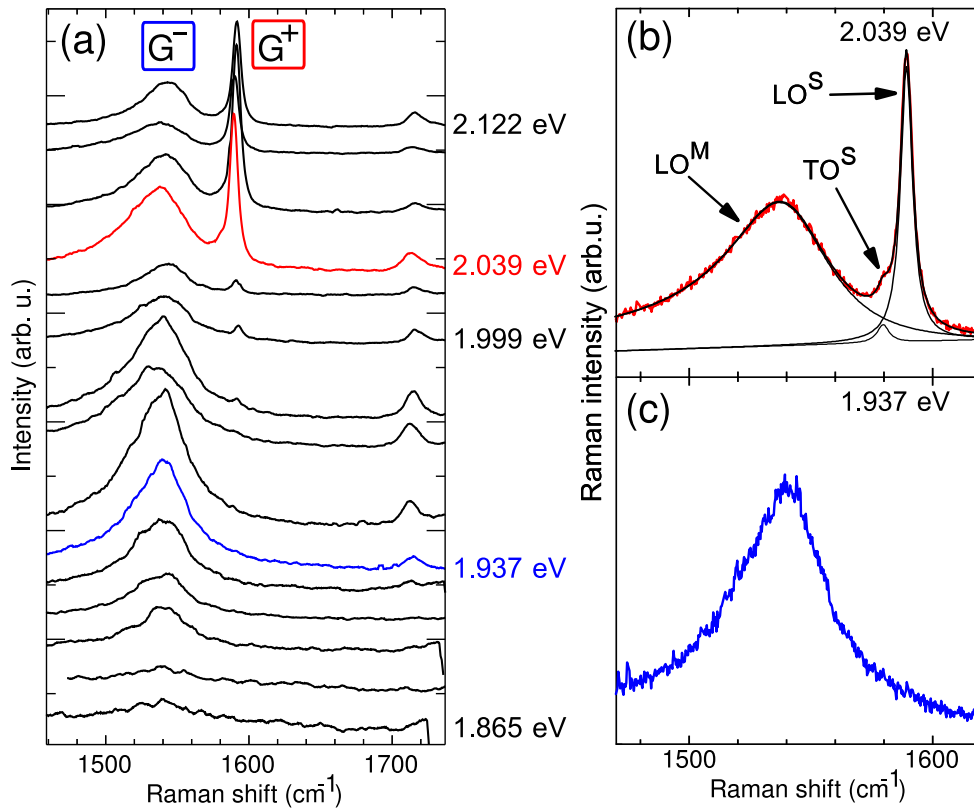


Figure 5.12: (a) High-energy mode Raman spectra for excitation energies in the range of the Rayleigh-scattering maxima of Fig. 5.11 (1.87 to 2.12 eV). G^- and G^+ show different resonance conditions. We observe an additional peak at 1677 cm^{-1} with the same resonance condition as G^- . (b) Spectrum obtained at 2.04 eV excitation energy; such a spectrum would typically be called a “metallic” Raman spectrum. Peaks are labeled by the associated phonons, LO or TO, where the superscript S indicates the semiconducting and M the metallic nanotube. (c) At an excitation energy of 1.94 eV the G^- but no G^+ peak is observed.

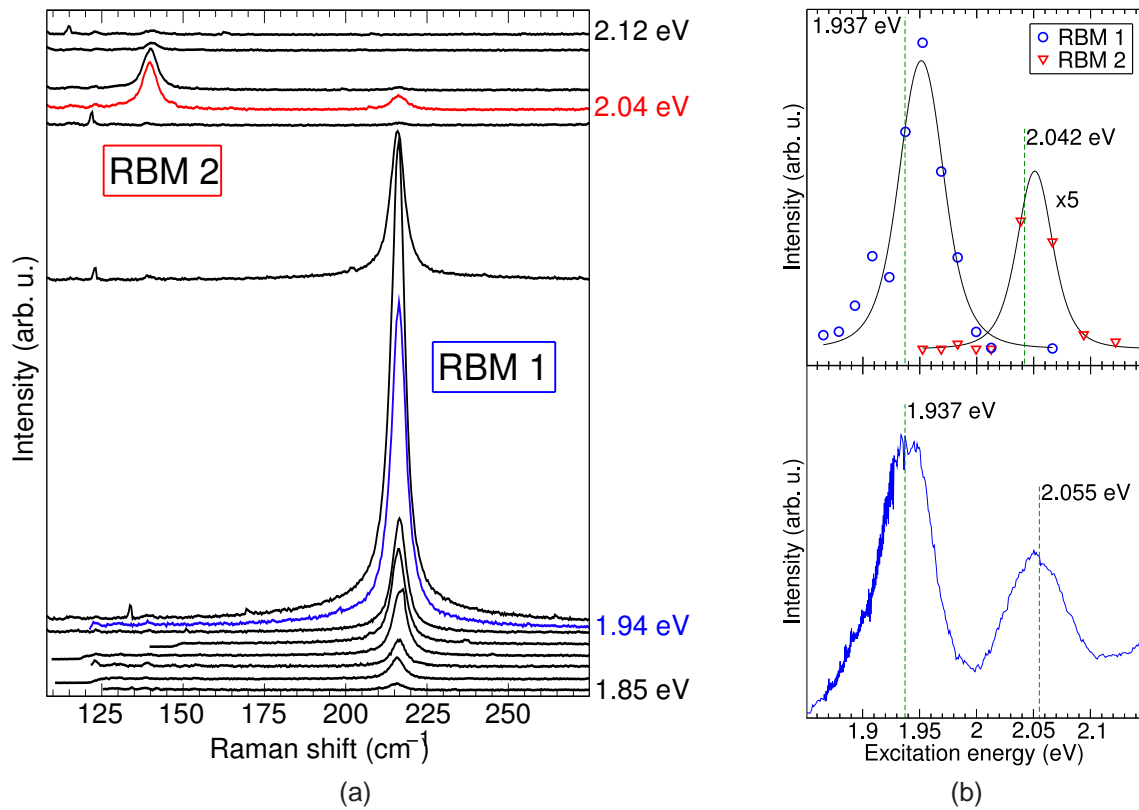


Figure 5.13: (a) RBM spectra excited at varying excitation energies. Two RBMs are observed corresponding to two nanotubes in the sample. RBM₁ (RBM₂) shows similar resonance conditions as the G^- (G^+) peak. (b) (top) Raman intensities of the radial breathing modes RBM₁ (circles) and RBM₂ (triangles) as a function of excitation energy. Fitting a Raman resonance profile (Eq. 2.5) to the data yields the transition energies marked by vertical dashed lines. The transition energies are slightly on the low-energy side of the profiles due to incoming and outgoing resonance, see Sect. 2.1.3. (bottom) Rayleigh spectrum of the sample. Transition energies obtained from Raman are in excellent agreement with the peak positions in the Rayleigh spectrum.

narrow peak (G^+) at 1590 cm^{-1} (FWHM = 5.6 cm^{-1}). In addition, a small shoulder at 1580 cm^{-1} and an asymmetric peak at 1677 cm^{-1} is seen. In the Raman spectrum excited at 2.039 eV [Fig. 5.12 (b)] both G^- and G^+ are present. Due to the metallic G^- peak this spectrum would typically be assigned to a metallic nanotube. [26, 28, 91, 101] While the broad peak (G^-) has its maximum intensity at 1.94 eV excitation energy, the narrow peak (G^+) appears only at excitation energies above this energy. This implies that the G^- and G^+ peaks originate from different nanotubes with different resonance energies, confirming the conclusion from the Rayleigh experiment that we have at least two tubes. In the following we show that the spectrum in Fig. 5.12 (b) can easily be explained if only the broad peak (G^-) is related to a metallic tube, whereas G^+ originates from a semiconducting tube.

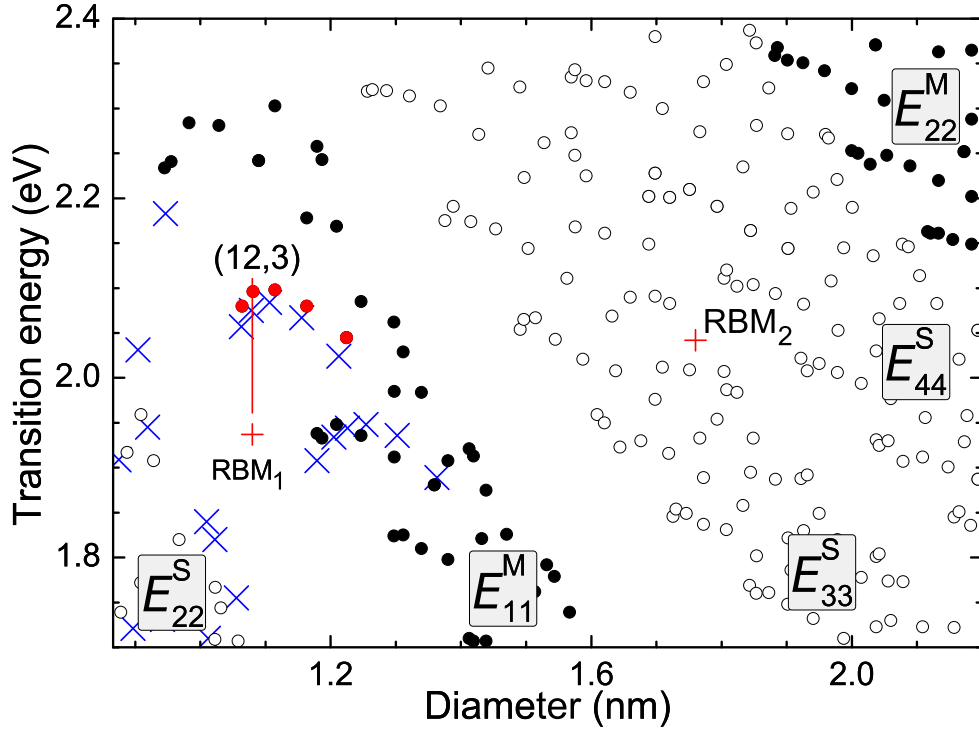


Figure 5.14: Kataura plot containing theoretical data by Popov *et al.* [21] (open and closed circles) and experimental data (x-symbols) from Ref. [20]. Theoretical data are upshifted by ≈ 300 meV according to Ref [21]. Results from this work, RBM₁ and RBM₂, are given by crosses. Considering screening effects RBM₁ is assigned to the metallic (12,3) tube. RBM₂ cannot be assigned to a particular nanotube but certainly originates from a semiconducting tube excited resonantly into the third E_{33}^S or forth E_{44}^S optical transition.

In addition to the HEM spectra, we collected Raman spectra of the radial breathing mode at the same excitation energies, shown in Fig. 5.13 (a). We observed two RBM peaks at 217 cm^{-1} (RBM₁) and 140 cm^{-1} (RBM₂), corresponding to the two nanotubes. Both RBM features go through resonance, with RBM₁ (RBM₂) having its maximum intensity at excitation energy similar to that of the G^- (G^+) mode. From the correlation of resonance energies we conclude that the G^- feature originates from the same tube as RBM₁ and G^+ from the same as RBM₂. In the top plot of Fig. 5.13 (b) we plot the intensities of both RBM peaks as a function of excitation energy. Fitting a Raman resonance profile (Eq. 2.5) to the data yields transition energies E_{ii} of 1.937 eV for RBM₁ and 2.04 eV for RBM₂. In Fig. 5.13 (b) we show how the resonance energies from the RBM intensity profiles (top) nicely match the peak positions in the Rayleigh spectrum (bottom). Note that the transition energies (dashed green line) in the Raman intensity profiles are slightly on the low-energy side of the profiles due to incoming and outgoing resonance, see Sect. 2.1.3.

In order to assign the RBMs, and thus the high-energy G^- and G^+ peaks, to particu-

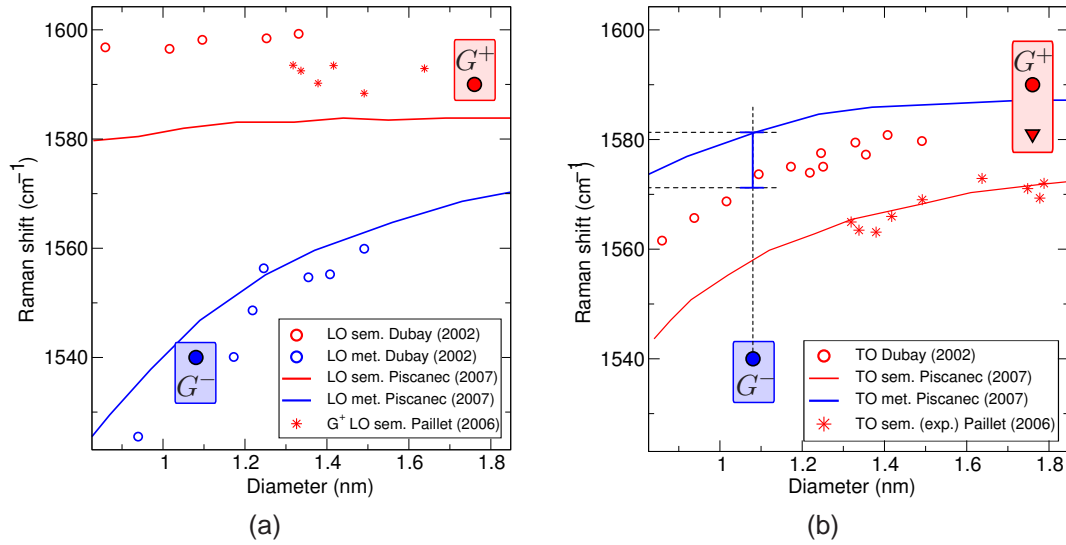


Figure 5.15: Phonon frequencies as a function of nanotube diameter. Our results for the G^+ peak (semiconducting tube) and the G^- peak (metallic tube) are given by the red and blue filled circles. (a) Further data are exclusively LO phonons in semiconducting (red) and metallic (blue) tubes, given in Ref. [24, 93, 102]. (b) As (a) for TO phonons. We also give the result for the shoulder on the low-energy side of G^+ (triangle). TO frequencies from Dubay *et al.* are the same for semiconducting and metallic tubes. (a) and (b) Note that Ref. [24] and [93] are theory work while Ref. [102] presents results from experiment.

lar chiral indices (n_1, n_2) , we identify the RBM frequency and its corresponding Raman resonance energy in an experimental or theoretical/empirical Kataura plot. [4, 5, 20, 108] The Kataura plot in Fig. 5.14 shows theoretical data based on a non-orthogonal tight binding model from Ref. [21] and experimental values (\times -symbols) from Ref. [20]. Our results for RBM₁ and RBM₂ are marked by crosses in Fig. 5.14. The transition energies of nanotubes depend on the nanotube environment, whereas the RBM frequencies hardly change [5, 64, 72]. Assuming negligible deviation of the RBM frequency and a red-shift (159 meV) of the transition energies in our sample compared to the data in Fig. 5.14, we assign RBM₁ to the metallic (12,3) tube. Although we cannot assign the second nanotube to a specific (n_1, n_2) chirality, its RBM frequency and resonance energy clearly show that it is semiconducting (see Fig. 5.14).

As a consequence of the (n_1, n_2) assignment, we can relate the high-energy modes G^- and G^+ to a metallic and a semiconducting tubes, respectively, independent of assumptions concerning the lineshape of G^- and G^+ . This result supports previous experimental results and theoretical predictions about a strongly broadened and downshifted LO phonon in metallic nanotubes due to a Kohn anomaly [24, 29, 93, 94]. As shown in Figure 5.16 5.16 we can also confirm the observation of an asymmetric lineshape of the G^- of isolated metallic nanotubes [94].

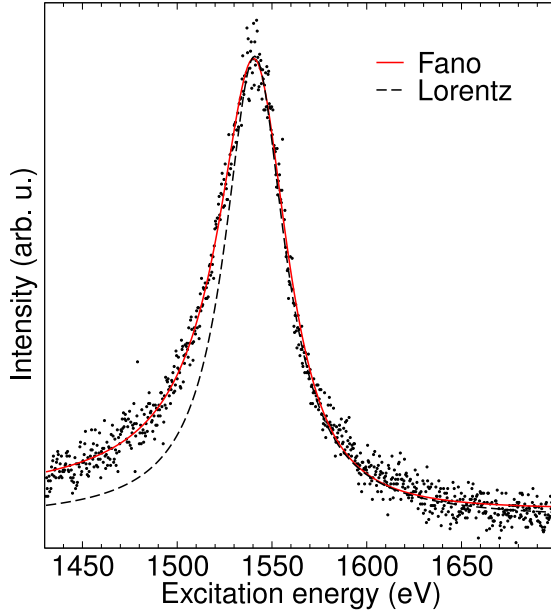


Figure 5.16: G^- peak of the metallic nanotube excited at 1.937 eV. To clarify the asymmetric lineshape we plot a Lorentzian (dashed black line) and a Fano (red line) lineshape on top of the data.

Concerning the G^+ peak at 1590 cm^{-1} (G^+) we can exclude that this peak originates from the TO phonon of the same metallic tube as the G^- mode because of the different resonance conditions for the G^- and G^+ features. Furthermore the frequency of the G^+ peak is higher than expected for the TO phonon in a metallic nanotube with a diameter as the one we observed. Next to our results figure 5.15 (b) shows TO-phonon frequencies as a function of nanotube diameter. While predictions from Ref. [93] show a large difference of the TO frequencies between metallic and semiconducting nanotubes, there is no difference predicted in Ref. [24]. In addition we plot experimental results of the TO-frequencies in *semiconducting* nanotubes from Ref. [102]. Regarding to the theoretical predictions we would expect the TO of the metallic nanotube to be between ≈ 1570 and $\approx 1580\text{ cm}^{-1}$ (blue bare in Fig. 5.15 (b)). Assuming the same frequencies of TOs in metallic and semiconducting nanotubes the frequency would be even lower at $\approx 1560\text{ cm}^{-1}$. Only for nanotubes with large diameters ($d > 5\text{ nm}$) does the TO frequency approach 1590 cm^{-1} .

Therefore, a lineshape like that of Fig. 5.12 (b) with both a broad and downshifted metallic G^- and an additional G^+ peak located at 1590 cm^{-1} can best be explained by the presence of at least one metallic and one semiconducting tube. Even if only the metallic lineshape as shown in Fig. 5.12 (c) is observed and the experiment is limited to a small number of excitation wavelengths, we cannot exclude the possibility that the sample contains an additional semiconducting nanotube that does not benefit from resonant enhancement. It seems that often a "metallic" spectrum like that in Fig. 5.12 (b) arises from a small bundle instead of a single metallic nanotube. [26, 28, 29, 101] In larger diameter metallic tubes, the G^- is less downshifted, and the spectrum will be more similar to that

of semiconducting tubes. [24, 93]

After assigning the observed high-energy modes to LO vibrations, the question arises whether we can observe the TO phonons as well. In fact, the G^+ peak (LO of the semiconducting tube) shows a small shoulder [see Fig. 5.12 (b)], which we fit to a weak peak lying 9 cm^{-1} below the principal G^+ feature. For a semiconducting nanotube with a diameter of 1.8 nm , as in our experimental sample, theory and experiment predict the TO phonon frequency $10\text{ to }20\text{ cm}^{-1}$ below the LO frequency (see Fig. 5.15 (b)) [24, 93, 102]. Therefore we assign the shoulder of the G^+ peak to the TO phonon in the semiconducting nanotube. When only the metallic nanotube is in resonance [Fig. 5.12 (c)] we cannot resolve a TO peak next to the G^- peak. The reason for the absence or very weak intensity of the TO peak might be that the (12,3) tube is close to a zig-zag tube for which the TO phonon is Raman forbidden by symmetry. [48]

The high-energy mode spectra in Fig. 5.12 shows an additional feature at 1677 cm^{-1} which was also observed in nanotube ensembles and which we refer to as the super-HEM (Sect. 5.1.3). As this peak has the same resonance condition as the G^- peak, we can assign it to the metallic (12,3) nanotube. An assignment of the different super-HEMs (sHEM) observed on a nanotube ensemble in Sect. 5.1.3 is rather difficult due to the large number of tubes in resonance. But with the exact (n_1, n_2) assignment of one sHEMs in this section we are able to assign also sHEMs observed in Sect. 5.1.3. Based on these assignments we proposed these tubes to be the second-order overtone of the IR-active mode. Furthermore we found a diameter dependence of the sHEM which might explain, why we do not observe a sHEM from the semiconducting nanotube in Fig. 5.12. Fig. 5.17 shows the diameter dependence of the sHEM (black line) found in Sect. 5.1.3. Although the error of the graph is very large, we expect the sHEM of the semiconducting tube to be at a similar frequency as the LO phonon mode (G^+). Therefore the sHEM might be outshined by the strong signal of the G^+ peak.

Finally we want to make a remark on the defect induced Raman mode (D-mode) which has not been investigated systematically in this work. We recorded the D-mode spectrum at an excitation energy of 1.999 eV where both nanotubes are observed [Fig. 5.12 (a)]. This spectrum showed no signal of the D-mode, which agrees with our general experience on separated nanotubes in solution.

5.3 Summary

The presence of metallic nanotubes in a sample is usually probed by Raman experiments on nanotube bundles. It was assumed that the broadening and downshift of the G^- peak – the so called metallic lineshape – is correlated to the bundling and that this peak is

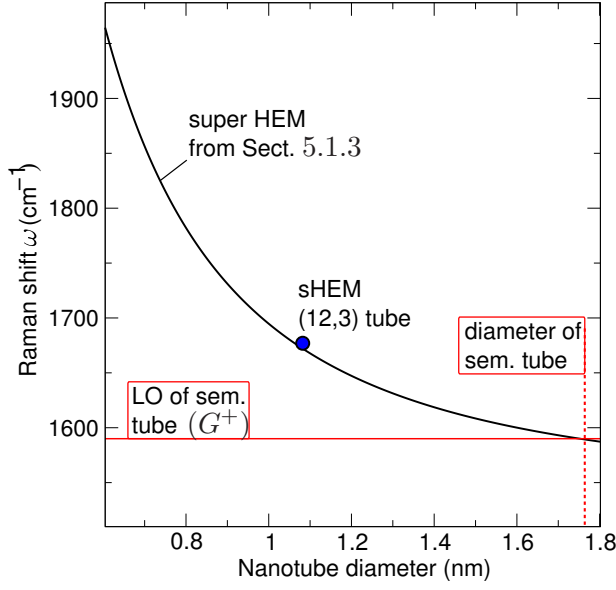


Figure 5.17: Frequency of the super-HEM as a function of tube diameter found in Sect. 5.1.3. With increasing diameter the frequency of the sHEM approaches the position of the LO phonon mode of semiconducting nanotubes. The sHEM signal of semiconducting tube is probably at the same position as the G^+ peak.

therefore not observed in nanotubes separated in solution. We show that the metallic lineshape of the HEM is observed also in nanotube ensembles separated in solution, although, the intensity of the metallic G^- is weaker in separated tubes compared to bundles. By correlating the resonance profiles of the HEM and the RBM, we could assign the broad and downshifted G^- to metallic nanotubes. From Raman and Rayleigh experiments on a small bundle of one semiconducting and one metallic nanotube we can furthermore conclude that the appearance of a G^+ peak at 1590 cm^{-1} in addition to the broad and downshifted metallic peak indicates the presence of a semiconducting nanotube next to the metallic tube. This implies that also the G^+ peak in the Raman experiments on nanotube ensembles originates exclusively from semiconducting tubes.

By comparison of our data to theoretical predictions with respect to the diameter dependence of the peak positions we assign the broad downshifted metallic peak (G^-) as well as the sharp semiconducting peak (G^+) to LO phonons. In metallic tubes the frequency of the LO phonon is downshifted due to a strong electron-phonon coupling to electrons close to the Fermi level (Kohn anomaly).

On the low energy side of the HEM for nanotube ensembles in solution we observe a series of small peaks with different resonance conditions. Based on a similar comparison as used in case of G^- and G^+ we can assign these small peaks to the TO phonons of small diameter semiconducting nanotubes.

Furthermore we can assign peaks which are observed on the high-energy side of the HEM to particular (n_1, n_2) or groups of tubes. Tentatively we assign these peaks to the second-order Raman process of the infrared-active phonons.

Chapter 6

Conclusions

In this work we present Raman scattering experiments on ensembles of nanotubes in solution and individual suspended nanotubes.

In the first part of this work (Chap. 4) we study the maximum Raman intensities for a large number of (n_1, n_2) including semiconducting and metallic nanotubes. We show that the strong differences between the RBM Raman intensities of the first and second optical transition of semiconducting nanotubes can be related to a larger broadening parameter of the second transition compared to the first transition. This is in accordance with a shorter live times of carriers excited into the second optical transition compared to carriers in the first transition. Also intensity differences between metallic and semiconducting nanotubes can be related to a stronger broadening of metallic transitions rather than differences in the electron-phonon coupling.

On the other hand intensity variations as a function of nanotube family, chiral angle and diameter are related to variations in the Raman matrix elements, primarily the electron-phonon coupling. The dependence of the RBM intensity on the family and the chiral angle can be correlated to the position of the electronic transition with respect to the K point.¹ We find a small maximum of the electron-phonon coupling for tubes with the transition close to K - Γ symmetry line and a large maximum for tubes with the transition close to the K - M direction. Close to K - K line we find a minimum, where the electron-phonon coupling is close to zero. Due to the trigonal warping of the graphene bandstructure the minimum electron-phonon coupling is obtained for nanotubes with a chiral angle of $\approx 20^\circ$ and with a family index of either $\nu = +1$ or $\nu = -1$ depending on the electronic transition. Surprisingly, the Raman intensities of nanotubes with transitions exactly on the K - M symmetry line are extremely weak. In order to clarify whether this is due

¹Therefore the line of allowed states which is involved in the particular transition has to be plotted on top of the graphene bandstructure in according to the zonefolding approximation.

to the broadening of the optical transition or a weak electron-phonon coupling further experiments are necessary.

The dependence of the RBM Raman intensity on the nanotube diameter is related to three effects. First, with increasing diameter the broadening of the electronic transitions decreases which causes the intensity to rise. Second, with increasing diameter the RBM frequency decreases, which reduces the distance between incoming and outgoing resonance. This again causes the intensity to rise with diameter. The observed overall decrease of the intensities with diameter can therefore only be explained by a decrease of the electron phonon coupling.

In the second part of this work (Chap. 5) we study the lineshape of the high-energy mode. From experiments on a tiny bundle of one metallic and one semiconducting nanotube we conclude that the broad and downshifted G^- peak is related to the LO phonon in metallic nanotubes. We show that the observation of a sharp peak at 1590 cm^{-1} indicates the presence of an additional semiconducting nanotube. The peak at 1590 cm^{-1} in semiconducting nanotubes is again related to the LO phonon. The energy of the LO phonon in metallic nanotubes is broadened and downshifted in comparison to the LO in semiconducting nanotubes due to the effect of a Kohn anomaly. The fact that we see the downshifted and broadened G^- peak of metallic nanotubes in the tiny bundle as well as in the nanotube separated in solution clarifies that this peak is an intrinsic feature of metallic carbon nanotubes.

On nanotube ensembles dispersed in solution we observe several features in addition to the major G^- and G^+ features. We can assign a series of peaks on the low energy side of the HEM to particular (n_1, n_2) or groups of nanotubes. This leads to a diameter dependence of this feature. By comparison to theoretical prediction we assign this peak to the TO phonon in semiconducting nanotubes. In order to strengthen this assignment the measurements should be extended to higher and lower excitation energies.

Furthermore we find peaks on the high energy side of the HEM which we tentatively assign to the second-order Raman modes of the infrared-active phonon. To clarify this assignment a detailed study of this feature and the intermediate frequency modes is necessary. The frequency of the first-order phonon falls into this region and might be visible due to imperfections in the nanotubes.

Bibliography

- [1] S. Iijima, “Helical microtubules of graphitic carbon”, *Nature* **354**, 56 (1991).
- [2] B. Yakobson and R. Smalley, “Fullerene nanotubes: C-1000000 and beyond”, *American Scientist* **85**(4), 324–337 (1997).
- [3] S. Reich, C. Thomsen, and J. Maultzsch, *Carbon Nanotubes: Basic Concepts and Physical Properties* (Wiley-VCH, Berlin, 2004).
- [4] J. Maultzsch and C. Thomsen, “Characterization of carbon nanotubes by optical spectroscopy”, in *AMN: Advanced Micro and Nanosystems*, edited by C. Hierold (Wiley-VCH, Weinheim, 2008), vol. 8.
- [5] J. Maultzsch, H. Telg, S. Reich, and C. Thomsen, “Radial breathing mode of single-walled carbon nanotubes: Optical transition energies and chiral-index assignment”, *Phys. Rev. B* **72**, 205 438 (2005).
- [6] R. Krupke, F. Hennrich, H. v. Löhneysen, and M. M. Kappes, “Separation of metallic from semiconducting single-walled carbon nanotubes”, *Science* **301**, 344 (2003).
- [7] M. S. Strano, C. A. Dyke, M. L. Usrey, P. W. Barone, M. J. Allen, *et al.*, “Electronic structure control of single-walled carbon nanotube functionalization”, *Science* **301**, 1519 (2003).
- [8] M. Zheng, A. Jagota, M. S. Strano, A. P. Santos, P. Barone, *et al.*, “Structure-based carbon nanotube sorting by sequence-dependent dna assembly”, *Science* **302**, 1545 (2003).
- [9] P. Collins, K. Bradley, M. Ishigami, and A. Zettl, “Extreme oxygen sensitivity of electronic properties of carbon nanotubes”, *Science* **287**(5459), 1801–1804 (2000).
- [10] P. T. Araujo and A. Jorio, “The role of environmental effects on the optical transition energies and radial breathing mode frequency of single wall carbon nanotubes”, *phys. stat. sol. (b)* **245**(10, Sp. Iss. SI), 2201–2204 (2008).

- [11] V. C. Moore, M. S. Strano, E. H. Haroz, R. H. Hauge, and R. E. Smalley, “Individually suspended single-walled carbon nanotubes in various surfactants”, *Nano Lett.* **3**, 1379 (2003).
- [12] Y. Miyauchi, R. Saito, K. Sato, Y. Ohno, S. Iwasaki, *et al.*, “Dependence of exciton transition energy of single-walled carbon nanotubes on surrounding dielectric materials”, *Chem. Phys. Lett.* **442**(4-6), 394–399 (2007).
- [13] E. Malić, *Many-particle theory of optical properties in low-dimensional nanostructures*, Ph.D. thesis, Technische Universität Berlin, Hardenbergstrasse 36, 10623 Berlin (2008).
- [14] X. Tu, S. Manohar, A. Jagota, and M. Zheng, “DNA sequence motifs for structure-specific recognition and separation of carbon nanotubes”, *Nature* **460**(7252), 250–253 (2009).
- [15] N. Stiirzl, F. Hennrich, S. Lebedkin, and M. M. Kappes, “Near Monochiral Single-Walled Carbon Nanotube Dispersions in Organic Solvents”, *J. Phys. Chem. C* **113**(33), 14 628–14 632 (2009).
- [16] A. Jorio, A. P. Santos, H. B. Ribeiro, C. Fantini, M. Souza, *et al.*, “Quantifying carbon-nanotube species with resonance raman scattering”, *Phys. Rev. B* **72**, 075 207 (2005).
- [17] H. Telg, J. Maultzsch, S. Reich, and C. Thomsen, “Resonant-raman intensities and transition energies of the $e_{[11]}$ transition in carbon nanotubes”, *Phys. Rev. B* **74**(11), 115415 (pages 5) (2006).
- [18] J. M. S. R. H. Telg and C. Thomsen, “First and second optical transitions in single-walled carbon nanotubes: a resonant raman study”, *phys. stat. sol. (b)* **244**(11), 4006 (2007).
- [19] S. K. Doorn, D. A. Heller, P. W. Barone, M. L. Usrey, and M. S. Strano, “Resonant raman excitation profiles of individually dispersed single walled carbon nanotubes in solution”, *Appl. Phys. A* **78**, 1147 (2004).
- [20] H. Telg, J. Maultzsch, S. Reich, F. Hennrich, and C. Thomsen, “Chirality distribution and transition energies of carbon nanotubes”, *Phys. Rev. Lett.* **93**, 177 401 (2004).

- [21] V. N. Popov, L. Henrard, and P. Lambin, “Electron-phonon and electron-photon interactions and resonant raman scattering from the radial-breathing mode of single-walled carbon nanotubes”, *Phys. Rev. B* **72**(3), 035 436 (2005).
- [22] J. Jiang, R. Saito, K. Sato, J. S. Park, G. G. Samsonidze, *et al.*, “Exciton-photon, exciton-phonon matrix elements, and resonant raman intensity of single-wall carbon nanotubes”, *Phys. Rev. B* **75**(3), 035405 (pages 10) (2007).
- [23] K. Kempa, “Gapless plasmons in carbon nanotubes and their interactions with phonons”, *Phys. Rev. B* **66**, 195 406 (2002).
- [24] O. Dubay, G. Kresse, and H. Kuzmany, “Phonon Softening in Metallic Nanotubes by a Peierls-like Mechanism”, *Phys. Rev. Lett.* **88**, 235 506 (2002).
- [25] M. Lazzeri, S. Piscanec, F. Mauri, A. Ferrari, and J. Robertson, “Phonon linewidths and electron-phonon coupling in graphite and nanotubes”, *Phys. Rev. B* **73**, 155 426 (2006).
- [26] J. Maultzsch, S. Reich, U. Schlecht, and C. Thomsen, “High-energy phonon branches of an individual metallic carbon nanotube”, *Phys. Rev. Lett.* **91**, 087 402 (2003).
- [27] C. Jiang, K. Kempa, J. Zhao, U. Schlecht, U. Kolb, *et al.*, “Strong enhancement of the Breit-Wigner-Fano Raman line in carbon nanotube bundles caused by plasmon band formation”, *Phys. Rev. B* **66**, 161 404(R) (2002).
- [28] A. Jorio, A. G. Souza Filho, G. Dresselhaus, M. S. Dresselhaus, A. K. Swan, *et al.*, “*G*-band resonant Raman study of 62 isolated single-wall carbon nanotubes”, *Phys. Rev. B* **65**, 155 412 (2002).
- [29] M. Oron-Carl, F. Hennrich, M. Kappes, H. Löhneysen, and R. Krupke, “On the electron-phonon coupling of individual single-walled carbon nanotubes”, *Nano Lett.* **5**(9), 1761–1767 (2005).
- [30] A. Gaur and M. Shim, “Substrate-enhanced σ^2 adsorption and complexity in the raman g-band spectra of individual metallic carbon nanotubes”, *Phys. Rev. B* **78**(12), 125422 (2008).
- [31] M. Cardona, “First-order raman scattering in crystals”, in *Light Scattering in Solids II*, edited by M. Cardona and G. Güntherodt (Springer, Berlin, 1982), vol. 50 of *Topics in Applied Physics*, p. 38.

- [32] M. Cardona, “Absolute raman scattering cross sections for molecules”, in *Light Scattering in Solids II*, edited by M. Cardona and G. Güntherodt (Springer, Berlin, 1982), vol. 50 of *Topics in Applied Physics*, p. 38.
- [33] R. Zeyher, H. Bilz, and M. Cardona, “Omega-4 Law in Microscopic Theories of Inelastic Light-Scattering”, *Solid State Communications* **19**(1), 57–60 (1976).
- [34] R. M. Martin and L. M. Falicov, “Resonant raman scattering”, in *Light Scattering in Solids I*, edited by M. Cardona (Springer, Berlin, 1983), vol. 50 of *Topics in Applied Physics*, p. 79.
- [35] M. Cardona, “Resonance phenomena”, in *Light Scattering in Solids II*, edited by M. Cardona and G. Güntherodt (Springer, Berlin, 1982), vol. 50 of *Topics in Applied Physics*, p. 19.
- [36] C. Thomsen and S. Reich, “Raman scattering in carbon nanotubes”, in *Light Scattering in Solids IX* (Springer, Berlin, 2007), vol. 108 of *Topics in Applied Physics*, pp. 115–235.
- [37] C. Trallero-Giner, A. Cantarero, M. Cardona, and M. Mora, “Impurity-induced resonant Raman scattering”, **45**, 6601 (1992).
- [38] G. Gao, T. Cagin, and W. Goddard, “Energetics, structure, mechanical and vibrational properties of single-walled carbon nanotubes”, *Nanotechnology* **9**(3), 184–191 (1998), 5th Foresight Conference on Molecular Nanotechnology, PALO ALTO, CALIFORNIA, NOV 05-08, 1997.
- [39] D. Walters, L. Ericson, M. Casavant, J. Liu, D. Colbert, K. Smith, and R. Smalley, “Elastic strain of freely suspended single-wall carbon nanotube ropes”, *Appl. Phys. Lett.* **74**(25), 3803–3805 (1999).
- [40] H. Dai, J. Hafner, A. Rinzler, D. Colbert, and R. Smalley, “Nanotubes as nanoprobe in scanning probe microscopy”, *Nature* **384**(6605), 147–150 (1996).
- [41] T. Rueckes, K. Kim, E. Joselevich, G. Tseng, C. Cheung, and C. Lieber, “Carbon nanotube-based nonvolatile random access memory for molecular computing”, *Science* **289**(5476), 94–97 (2000).
- [42] M. J. O’Connell, *Carbon Nanotube - Properties and Applications 2006* (Taylor & Francis, Boca Raton, 2006).
- [43] S. Tans, A. Verschueren, and C. Dekker, “Room-temperature transistor based on a single carbon nanotube”, *Nature* **393**(6680), 49–52 (1998).

- [44] S. Berber, Y.-K. Kwon, and D. Tománek, “Unusually high thermal conductivity of carbon nanotubes”, *Phys. Rev. Lett.* **84**(20), 4613–4616 (2000).
- [45] H. Kataura, Y. Kumazawa, Y. Maniwa, I. Umezū, S. Suzuki, Y. Ohtsuka, and Y. Achiba, “Optical properties of single-wall carbon nanotubes”, *Synth. Met.* **103**, 2555 (1999).
- [46] S. Reich, J. Maultzsch, C. Thomsen, and P. Ordejón, “Tight-binding description of graphene”, *Phys. Rev. B* **66**, 035 412 (2002).
- [47] H. Ajiki and T. Ando, “Carbon nanotubes: Optical absorption in Aharonov-Bohm flux”, *Jpn. J. Appl. Phys. Suppl.* **34-1**, 107 (1994).
- [48] M. Damnjanović, I. Milošević, T. Vuković, and R. Sredanović, “Full symmetry, optical activity, and potentials of single-wall and multiwall nanotubes”, *Phys. Rev. B* **60**(4), 2728–2739 (1999).
- [49] V. Popov, “Curvature effects on the structural, electronic and optical properties of isolated single-walled carbon nanotubes within a symmetry-adapted non-orthogonal tight-binding model”, *New Journal of Physics* **6** (2004).
- [50] M. Machón, S. Reich, H. Telg, J. Maultzsch, P. Ordejón, and C. Thomsen, “Strength of radial breathing mode in single-walled carbon nanotubes”, *Phys. Rev. B* **71**, 035 416 (2005).
- [51] E. Chang, G. Bussi, A. Ruini, and E. Molinari, “Excitons in carbon nanotubes: an *ab-initio* symmetry-based approach”, **92**, 196 401 (2004).
- [52] V. Perebeinos, J. Tersoff, and P. Avouris, “Scaling of excitons in carbon nanotubes”, **92**, 257 402 (2004).
- [53] C. D. Spataru, S. Ismail-Beigi, L. X. Benedict, and S. G. Louie, “Excitonic effects and optical spectra of single-walled carbon nanotubes”, **92**, 077 402 (2004).
- [54] F. Wang, G. Dukovic, L. E. Brus, and T. Heinz, “The optical resonances in carbon nanotubes arise from excitons”, *Science* **308**, 838 (2005).
- [55] J. Maultzsch, R. Pomraenke, S. Reich, E. Chang, D. Prezzi, *et al.*, “Exciton binding energies in carbon nanotubes from two-photon photoluminescence”, *Phys. Rev. B* **72**, 241 402 (R) (2005).

- [56] E. Dobardžić, I. Milošević, B. Nikolić, T. Vuković, and M. Damnjanović, “Single-wall carbon nanotubes phonon spectra: Symmetry-based calculations”, *Phys. Rev. B* **68**, 045 408 (2003).
- [57] C. Thomsen and S. Reich, “Double-resonant Raman scattering in graphite”, **85**, 5214 (2000).
- [58] J. Maultzsch, S. Reich, and C. Thomsen, “Double-resonant Raman scattering in single-wall carbon nanotubes”, in *Proc. 26th ICPS*, edited by A. R. Long and J. H. Davies (Institute of Physics Publishing, Bristol (UK), 2002), p. D209.
- [59] V. Skakalova, J. Maultzsch, Z. Osvath, L. P. Biro, and S. Roth, “Intermediate frequency modes in Raman spectra of Ar+-irradiated single-wall carbon nanotubes”, *phys. stat. sol. lett.* **1**(4), 138–140 (2007).
- [60] C. Fantini, A. Jorio, M. Souza, R. Saito, G. Samsonidze, M. Dresselhaus, and M. Pimenta, “Steplike dispersion of the intermediate-frequency Raman modes in semiconducting and metallic carbon nanotubes”, *Phys. Rev. B* **72**(8) (2005).
- [61] R. A. Jishi, L. Venkataraman, M. S. Dresselhaus, and G. Dresselhaus, “Phonon modes in carbon nanotubules”, *Chem. Phys. Lett.* **209**, 77–82 (1993).
- [62] M. Longhurst and N. Quirke, “The environmental effect on the radial breathing mode of carbon nanotubes in water”, *J. Chem. Phys.* **124**(23) (2006).
- [63] P. T. Araujo, I. O. Maciel, P. B. C. Pesce, M. A. Pimenta, S. K. Doorn, *et al.*, “Nature of the constant factor in the relation between radial breathing mode frequency and tube diameter for single-wall carbon nanotubes”, *Phys. Rev. B* **77**(24), 241403 (pages 4) (2008).
- [64] C. Fantini, A. Jorio, M. Souza, M. S. Strano, M. S. Dresselhaus, and M. A. Pimenta, “Optical transition energies for carbon nanotubes from resonant raman spectroscopy: Environment and temperature effects”, *Phys. Rev. Lett.* **93**, 147 406 (2004).
- [65] G. Zhang and B. Li, “Thermal conductivity of nanotubes revisited: Effects of chirality, isotope impurity, tube length, and temperature”, *J. Chem. Phys.* **123**(11) (2005).
- [66] V. Perebeinos, J. Tersoff, and P. Avouris, “Electron-phonon interaction and transport in semiconducting carbon nanotubes”, *Phys. Rev. Lett.* **94**(8) (2005).
- [67] L. Chico, M. P. López-Sancho, and M. C. Muñoz, “Spin splitting induced by spin-orbit interaction in chiral nanotubes”, *Phys. Rev. Lett.* **93**(17), 176 402 (2004).

-
- [68] F. Hennrich, S. Lebedkin, and M. M. Kappes, “Improving separation techniques for single-walled carbon nanotubes: Towards monodisperse samples”, *phys. stat. sol. (b)* **245**(10, Sp. Iss. SI), 1951–1953 (2008).
- [69] S. M. Bachilo, M. S. Strano, C. Kittrell, R. H. Hauge, R. E. Smalley, and R. B. Weisman, “Structure-assigned optical spectra of single-walled carbon nanotubes”, *Science* **298**, 2361 (2002).
- [70] M. Gao, J. M. Zuo, R. D. Twisten, I. Petrov, L. A. Nagahara, and R. Zhang, “Structure determination of individual single-wall carbon nanotubes by nanoarea electron diffraction”, **82**, 2703 (2003).
- [71] M. J. O’Connell, S. M. Bachilo, C. B. Huffman, V. C. Moore, M. S. Strano, *et al.*, “Band gap fluorescence from individual single-walled carbon nanotubes”, *Science* **297**, 593 (2002).
- [72] M. O’Connell, S. Sivaram, and S. Doorn, “Near-infrared resonance raman excitation profile studies of single-walled carbon nanotube intertube interactions: A direct comparison of bundled and individually dispersed hipco nanotubes”, *Phys. Rev. B* **69**, 235 415 (2004).
- [73] S. Lebedkin, F. Hennrich, T. Skipa, and M. M. Kappes, “Near-infrared photoluminescence of single-walled carbon nanotubes prepared by the laser vaporization method”, *J. Phys. Chem. B* **107**, 1949 (2003).
- [74] N. Izard, D. Riehl, and E. Anglaret, “Exfoliation of single-wall carbon nanotubes in aqueous surfactant suspensions: A Raman study”, *Phys. Rev. B* **71**, 195 417 (2005).
- [75] B. Kitiyanan, W. E. Alvarez, J. H. Harwell, and D. E. Resasco, “Controlled production of single-wall carbon nanotubes by catalytic decomposition of co on bimetallic co-mo catalysts”, **317**, 497 (2000).
- [76] S. Reich, L. Li, and J. Robertson, *Chem. Phys. Lett.* **421**, 469 (2006).
- [77] J. Robertson, G. Zhong, H. Telg, C. Thomsen, J. H. Warner, *et al.*, “Growth and characterization of high-density mats of single-walled carbon nanotubes for interconnects”, *Appl. Phys. Lett.* **93**(16), 163111 (pages 3) (2008).
- [78] M. S. Arnold, S. I. Stupp, and M. C. Hersam, “Enrichment of single-walled carbon nanotubes by diameter in density gradients”, *Nano Lett.* **5**(4), 713–718 (2005).

- [79] S. Lebedkin, F. Hennrich, O. Kiowski, and M. M. Kappes, “Photophysics of carbon nanotubes in organic polymer-toluene dispersions: Emission and excitation satellites and relaxation pathways”, *Phys. Rev. B* **77**(16), 165429 (pages 8) (2008).
- [80] H. Telg, J. Maultzsch, S. Reich, F. Hennrich, and C. Thomsen, “Raman intensities of the first optical transitions in carbon nanotubes”, *phys. stat. sol. (b)* **243**(13), 3181 (2006).
- [81] J.-S. Lauret, C. Voisin, G. Cassabois, C. Delalande, P. Roussignol, O. Jost, and L. Capes, “Ultrafast carrier dynamics in single-wall carbon nanotubes”, *Phys. Rev. Lett.* **90**, 057 404 (2003).
- [82] B. C. Satishkumar, S. V. Goupalov, E. H. Haroz, and S. K. Doorn, “Transition level dependence of raman intensities in carbon nanotubes: Role of exciton decay”, *Phys. Rev. B* **74**, 155 409 (2006).
- [83] M. Machón, *Electron-phonon coupling, vibrational, and optical properties of carbon nanotubes and picotubes*, Ph.D. thesis, Technische Universität Berlin, Hardenbergstrasse 36, 10623 Berlin (2006).
- [84] S. Reich, C. Thomsen, and J. Robertson, “Exciton resonances quench the photoluminescence of zigzag carbon nanotubes”, *Phys. Rev. Lett.* **95**, 077 402 (2005).
- [85] S. K. Doorn, P. T. Araujo, K. Hata, and A. Jorio, “Excitons and exciton-phonon coupling in metallic single-walled carbon nanotubes: Resonance raman spectroscopy”, *Phys. Rev. B* **78**(16), 165408 (pages 9) (2008).
- [86] K. Hata, D. N. Futaba, K. Mizuno, T. Namai, M. Yumura, and S. Iijima, “Water-Assisted Highly Efficient Synthesis of Impurity-Free Single-Walled Carbon Nanotubes”, *Science* **306**(5700), 1362–1364 (2004).
- [87] J. S. Park, Y. Oyama, R. Saito, W. Izumida, J. Jiang, *et al.*, “Raman resonance window of single-wall carbon nanotubes”, *Phys. Rev. B* **74**(16), 165414 (pages 6) (2006).
- [88] P. Nikolaev, M. Bronikowski, R. Bradley, F. Rohmund, D. Colbert, K. Smith, and R. Smalley, “Gas-phase catalytic growth of single-walled carbon nanotubes from carbon monoxide”, *Chem. Phys. Lett.* **313**(1-2), 91–97 (1999).
- [89] S. Heeg, C. Casiraghi, and S. Reich, “Quantitative composition of swcnt-sample: Raman scattering vs. photoluminescence”, (2009).

- [90] M. S. Strano, M. Zheng, A. Jagota, G. B. Onoa, D. A. Heller, P. W. Barone, and M. L. Usrey, “Understanding the nature of the dna-assisted separation of single-walled carbon nanotubes using fluorescence and raman spectroscopy”, *Nano Lett.* **4**, 543 (2004).
- [91] M. A. Pimenta, A. Marucci, S. A. Empedocles, M. G. Bawendi, E. B. Hanlon, *et al.*, “Raman modes of metallic carbon nanotubes”, *Phys. Rev. B* **58**, R16 016 (1998).
- [92] A. Jorio, C. Fantini, M. S. S. Dantas, M. A. Pimenta, A. G. Souza Filho, *et al.*, “Linewidth of the raman features of individual single-wall carbon nanotubes”, *Phys. Rev. B* **66**(11), 115 411 (2002).
- [93] S. Piscanec, M. Lazzeri, J. Robertson, A. C. Ferrari, and F. Mauri, “Optical phonons in carbon nanotubes: Kohn anomalies, peierls distortions, and dynamic effects”, *Phys. Rev. B* **75**, 035 427 (2007).
- [94] Y. Wu, J. Maultzsch, E. Knoesel, B. Chandra, M. Huang, *et al.*, “Variable electron-phonon coupling in isolated metallic carbon nanotubes observed by raman scattering”, *Phys. Rev. Lett.* **99**, 027 402 (2007).
- [95] H. Telg, J. Maultzsch, S. Reich, and C. Thomsen, “Chirality dependence of the high-energy raman modes in carbon nanotubes”, in *Electronic Properties of Novel Nanostructures*, edited by H. Kuzmany, J. Fink, M. Mehring, and S. Roth, AIP 786 (2005), p. 162.
- [96] J. Yan, Y. Zhang, P. Kim, and A. Pinczuk, “Electric field effect tuning of electron-phonon coupling in graphene”, *Phys. Rev. Lett.* **98**(16), 166802 (2007).
- [97] M. Fouquet, H. Telg, J. Maultzsch, Y. Wu, B. Chandra, *et al.*, “Longitudinal optical phonons in metallic and semiconducting carbon nanotubes”, *Phys. Rev. Lett.* **102**(7), 075501 (pages 4) (2009).
- [98] M. J. Bronikowski, P. A. Willis, D. T. Colbert, K. A. Smith, and R. E. Smalley, “Gas-phase production of carbon single-walled nanotubes from carbon monoxide via the HiPco process: A parametric study”, *J. Vac. Sci. Technol. A* **19**, 1800–1805 (2001).
- [99] M. J. O’Connell, S. M. Bachilo, C. B. Huffman, V. C. Moore, M. S. Strano, *et al.*, “Band-gap fluorescence from individual single-walled carbon nanotubes”, *Science* **297**, 593 (2002).

BIBLIOGRAPHY

- [100] M. Machón, S. Reich, and C. Thomsen, “Strong electron-phonon coupling of the high-energy modes of carbon nanotubes”, *Phys. Rev. B* **74**(20), 205423 (pages 4) (2006).
- [101] M. Paillet, P. Poncharal, A. Zahab, and J.-L. Sauvajol, “Vanishing of the breittwigner-fano component in individual single-wall carbon nanotubes”, *Phys. Rev. Lett.* **94**, 237 401 (2005).
- [102] M. Paillet, T. Michel, J. C. Meyer, V. N. Popov, L. Henrard, S. Roth, and J.-L. Sauvajol, “Raman active phonons of identified semiconducting single-walled carbon nanotubes”, **96**, 257 401 (2006).
- [103] H. Telg, M. Fouquet, J. Maultzsch, Y. Wu, B. Chandra, *et al.*, “G(-) and G(+) in the Raman spectrum of isolated nanotube: a study on resonance conditions and lineshape”, *phys. stat. sol. (b)* **245**(10, Sp. Iss. SI), 2189–2192 (2008).
- [104] M. Y. Sfeir, F. Wang, L. Huang, C. Chuang, J. Hone, *et al.*, “Probing electronic transitions in individual carbon nanotubes by rayleigh scattering”, **306**, 1540 (2004).
- [105] L. Huang, X. Cui, B. White, and S. P. O’Brien, “Long and oriented single-walled carbon nanotubes grown by ethanol chemical vapor deposition”, *J. Phys. Chem. B* **108**, 16 451 (2004).
- [106] K. Matsuda, Y. Kanemitsu, K. Irie, T. Saiki, T. Someya, Y. Miyauchi, and S. Maruyama, “Photoluminescence intermittency in an individual single-walled carbon nanotube at room temperature”, *Appl. Phys. Lett.* **86**(12), 123116 (2005).
- [107] F. Simon, R. Pfeiffer, and H. Kuzmany, “Temperature dependence of the optical excitation lifetime and band gap in chirality assigned semiconducting single-wall carbon nanotubes”, *Phys. Rev. B* **74**(12), 121411 (2006).
- [108] R. Pfeiffer, F. Simon, H. Kuzmany, and V. N. Popov, “Fine structure of the radial breathing mode of double-wall carbon nanotubes”, *Phys. Rev. B* **72**(16), 161404 (pages 4) (2005).

Acknowledgements

This work would not have been possible without the contribution of many people. I want to thank all those who supported me, in particular

Prof. Christian Thomsen for providing me the opportunity to perform exciting scientific work in the familiar working environment of his group. Thank you for the academic supervision and the persistent motivation.

Prof. Janina Maultzsch for supervising me, beyond my Diploma thesis. Many thanks for always finding time to answer my questions, to read my manuscripts or to have a chat (cookies included).

Prof. John Robertson for the fruitful scientific collaboration and for reviewing this work.

Prof. Sabine Klapp for being the chairwoman of my defense.

Frank Hennrich for providing the nanotube suspensions.

Prof. Tony Heinz for supporting the work on individual nanotubes. Many thanks also to his group and the group of Prof. James Hone, who prepared the samples and performed the Rayleigh experiments.

Marianne Heinold for support and handling of the bureaucracy. I deeply regret the loss of a good colleague and nice person.

Harald Scheel for his overall server and lab support.

Mandy Neumann, Bernd Schöler, Michael Mayer und Heiner Perls for handling of the bureaucracy, for technical support and for taking care of the instruments.

Christian Kristukat for writing the great data processing tool *peak-o-mat* and for awaking my interest in programming.

the whole AG Thomsen for the great atmosphere.